Time-Resolved Vibrational Spectroscopy in the Impulsive Limit

Lisa Dhar, John A. Rogers, and Keith A. Nelson*

Department of Chemistry, Massachusetts Institute of Technology, Cambridge, Massachusetts 02139

Received June 24, 1993 (Revised Manuscript Received November 16, 1993)

Contents

I. Introduction

The development of femtosecond lasers brought entirely new possibilities into the practive of time-resolved vibrational spectroscopy (TRVS). For the first time, it became possible to conduct observations on time scales that are not only shorter than vibrational lifetimes or dephasing times, but shorter than individual vibrational oscillation periods. It therefore became possible, in principle, to monitor materials and molecules at various stages of vibrational distortion, recording "stop-action" spectroscopic observations corresponding to well-defined nonequilibrium molecular or condensed-phase geometries. In principle, stretched or bent molecules, distorted crystal lattices, and other specific out-of-equilibrium structures could be characterized directly. Molecular structures corresponding to unstable intermediates between reactant and product, crystal structures assumed during transitions between different phases, and other nonequilibrium species of interest in connection with rearrangements of matter could be observed.

In practice the realization of these possibilities requires not only adequate time resolution for probing vibrations but also excitation mechanisms suitable for initiating the vibrational oscillations in a phase-coherent (i.e. synchronized) manner. Fortunately, such mechanisms exist and in fact come into play ubiquitously and unavoidably whenever ultrashort pulses interact with most forms of matter. Thus time-resolved observations of coherent vibrational motion in ground and excited electronic states of solid, liquid, and gas phases have now been recorded. These have provided new insights into chemical and structural rearrangements in all phases of matter and into the dynamical behavior of crystal lattices, liquids, isolated molecules, and biological systems.

In this review we discuss the main mechanisms through which phase-coherent vibrational motional is initiated and monitored in the "impulsive" limit, that is, the limit in which the pulse duration is less than a single vibrational oscillation period. Qualitative physical pictures of the different mechanisms are presented first. The excitation and probing processes are then treated theoretically from both classical and quantum mechanical points of view, with some emphasis on the physical appeal as well as the limitations of the classical treatment.

Following elucidation of the excitation and probing processes, a series of examples is given to illustrate the

0009-2665/94/0794-0157$14.00/0

Lisa Dhar was born in Evanston, IL, on September 23, 1968. She received the B.S. degree in chemistry from the University of Chicago in 1989. At MIT, her research has focused on the dynamics of low-frequency phonons in ferroelectric crystals and acoustic modes in ferroelectric thin-film systems. She has also worked on femtosecond reaction dynamics in condensed-phase systems. She is the recepient of the Department of Defense Graduate Fellowship and the AT&T Bell Laboratories Graduate Research Program for Women Award.

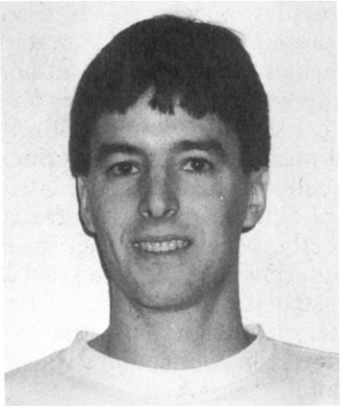

John A. Rogers was born in Rolla, MO, on August 22, 1967. He received a B.S. degree in physics and a B.A. degree in chemistry from the University of Texas at Austin in 1989. Since arriving at MIT in the fall of 1989, his research has centered on the development of an optical technique for real-time evaluation of mechanical and thermal properties of thin films. This research led to master of science degrees in chemistry and physics in 1992. Although his research remains focused on thin-films dynamics, his interests include the development and use of experimental techniques which allow for excitation and time-resolved observation of microscopic motions involved in phase transitions and chemical reactions. He is the recepient of a National Science Foundation Graduate Fellowship.

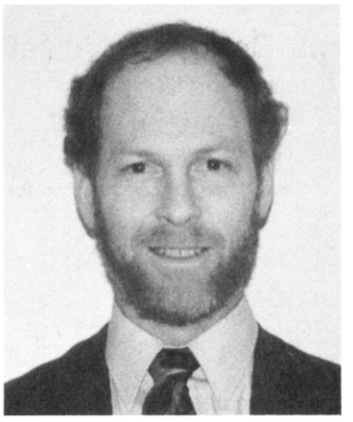

Keith A. Nelson was born in New York, NY, on December 8, 1953. He received the B.S. degree in chemistry and Ph.D. in physical chemistry in 1976 and 1981 from Stanford University. He then did postdoctoral work at UCLA. He has been on the faculty of the MIT Department of Chemistry since 1982. His main interests are in time-resolved spectrocopy of structural and chemical rearrangements in condensed materials. Professor Nelson has received a Presidential Young Investigator Award, Alfred P. Sloan Fellowship, Coblentz Prize, and Japan Society for Promotion of Science Fellowship. He is a Fellow of the Americal Physical Society.

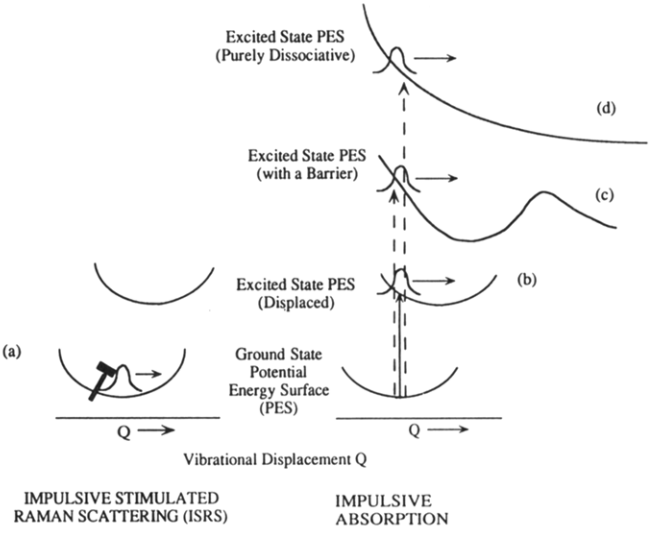

Figure 1. Mechanisms for impulsive initiation of coherent vibrational motion, represented in the figure by coherent wavepacket propagation. Impulsive stimulated scattering initiates coherent vibrations in the ground electronic state. Impulsive absorption initiates coherent vibrational motion in the electronic excited state. Note that if the excited state is unstable, phase-coherent motion is still initiated. In this case synchronized dissociation or other rearrangements can occur. This is the basis for "femtochemistry".

progress made to date in impulsive time-resolved vibrational spectroscopy and to indicate some of the prospects. Regarding the latter, increased capabilities for control over, as well as observation of, coherent vibrational motion are emphasized. These capabilities hold promise for improved control over chemical and structural rearrangements involving the vibrational motions being manipulated.

II. Qualitative Physical Picture

A. Impulsive Excitation Mechanisms

There are two excitation mechanisms most commonly exploited for impulsive vibrational excitation, impulsive stimulated Raman scattering (ISRS) which can occur with nonresonant or resonant excitation wavelengths and impulsive absorption which can occur on resonance. Figure 1a illustrates impulsive stimulated Raman scattering[1-6] when the excitation wavelength is far from any electronic absorption resonance. In this case, the ultrashort excitation pulse exerts a sudden ("impulse") driving force to initiate coherent vibrational motion in the ground electronic state of the molecule. The magnitude of the force, and the resulting coherent vibrational amplitude, are linearly proportional to the excitation light intensity and to the light-scattering differential polarizability for the mode being driven. This mode could be an acoustic vibration of a liquid or solid, an optic phonon in a crystal lattice, a molecular

vibration, or any other mode which is active in light scattering. The only requirements for ISRS excitation are that the pulse duration be short compared to the vibrational oscillation period and that the mode be Raman-active.

Ordinarily, stimulated Raman or Brillouin scattering involve two discrete frequencies, ω_1 and ω_2, tuned such that their difference matches a light-scattering-active vibrational mode.[7] In classical–mechanical terms, the (square of the) superposed electric fields exert an oscillatory driving force on the vibrational mode at the difference frequency. The mode undergoes forced oscillations which may continue after the pulses are gone. In impulsive stimulated scattering, the excitation pulse is only present for a fraction of the vibrational oscillation period and so an oscillatory force at the vibrational frequency cannot be exerted. Instead an impulse force on the vibrational mode is delivered, initiating coherent oscillations which continue after the pulse is gone. Stimulated scattering in the impulsive case occurs not through mixing between two discrete frequencies but through mixing among the continuous distribution of Fourier components within the spectral bandwidth of the ultrashort pulse. Since the pulse duration is less than the vibrational period, the spectral bandwidth of the pulse necessarily exceeds the vibrational frequency so that many frequency components are available to play the roles of ω_1 and ω_2. Note that in stimulated scattering with discrete frequency components (assuming $\omega_1 > \omega_2$), light is (Stokes-) shifted in frequency from ω_1 to ω_2 and the difference in energy is provided as vibrational energy in the medium. In ISRS, light is shifted from the blue toward the red side of the spectrum of the pulse to provide the coherent vibrational energy.

If the excitation wavelength is near an electronic absorption resonance, absorption may occur and coherent vibrational motion may be initiated in the excited electronic state[4,8,9] in addition to the ground electronic state as shown by Figure 1, parts b–d. Figure 1b shows the case of a stable excited-state potential energy surface (PES). In classical terms, absorption of the excitation pulse creates an electronic excited state whose geometry is initially that of the electronic ground state. The electronic excited-state equilibrium geometry is generally shifted from that of the ground state, so motion toward and oscillation about the new local equilibrium position begins. The requirements for coherent vibrational motion to occur are that the pulse duration be short compared to the excited-state vibrational period and that the mode have some degree of vibronic coupling to the electronic excitation as reflected in the shifted potential energy surface. In Figure 1c a reactive excited-state PES with a barrier is considered. In this case, after excitation to the excited state, (parts of) the wavepacket can either remain within the bound part of the potential surface and undergo coherent oscillations or cross the barrier and propagate along the surface toward the reaction product. The final possibility of a purely repulsive excited-state energy surface, commonly encountered in photodissociation reactions, is illustrated in Figure 1d. Here the phase-coherent motion of the wavepacket down the repulsive surface can be monitored to extract the reaction dynamics.

From a quantum–mechanical point of view, the excitation pulse in ISS creates a coherent superposition of vibrational states in the ground electronic level while the absorbed excited pulse creates a superposition of vibrational states in the excited electronic level. In more general terms, there is really no distinction between the two excitation mechanisms. The excitation pulse in general creates a coherent superposition of vibrational *and electronic* levels. It is only after electronic dephasing occurs, at which point which the material is in the ground or excited electronic eigenstate rather than a coherent superposition of the two, that the two processes are clearly distinguishable. A rigorous treatment must consider coherent wavepacket propagation along both potential energy surfaces, with coherent coupling of the electronic levels included explicitly. However, we will speak of two distinct excitation mechanisms throughout much of this review because in practice most experiments have been conducted on samples in which electronic dephasing was very rapid (most condensed phases) or in which no signatures of electronic phase coherence were observed in the probing process.

Since coherent vibrational motion is initiated by both resonant and nonresonant excitation wavelengths, it is a nearly unavoidable consequence whenever a sufficiently short light pulse passes through most types of matter.

B. Probing Processes

Coherent vibrational motion influences both the real and imaginary parts of the refractive index, so there are many optical observables through which such motion can be monitored. In practice, vibrational oscillations in ground electronic states have been probed mainly through their effects on the real part of the refractive index and coherent motion in electronic excited states has been monitored mostly through its effects on the imaginary part. Here we outline the methods that have been used to prove both components.

1. Probing the Real Part of the Refractive Index

a. Transient Grating Excitation and Probing. In many nonresonant ISS experiments, two time-coincident excitation pulses have been used to produce a spatially periodic "grating" excitation pattern, and in this case coherent scattering ("diffraction") of a probe pulse is detected.[1,2] This time-delayed four-wave mixing or "transient grating" excitation and detection geometry, illustrated in Figure 2a, often is used because the coherently scattered signal can be detected against a dark background. The geometry also offers experimental control over the vibrational wavevector $\mathbf{q}$ which is given by the difference between the excitation pulse wavevectors $\mathbf{k}_1$ and $\mathbf{k}_2$, i.e. $\mathbf{q} \approx \pm(\mathbf{k}_1 - \mathbf{k}_2)$. For dispersive vibrational excitations such as acoustic phonons or polar optic phonon–polariton modes, the vibrational frequency ω depends on the wavevector orientation and magnitude.[2,10] In the transient grating experimental setup, higher-frequency components in each incident excitation pulse undergo stimulated scattering into lower-frequency components in each opposite outgoing pulse, creating vibrational excitations of the difference wavevectors and the natural vibrational frequency $\omega(\mathbf{q})$.

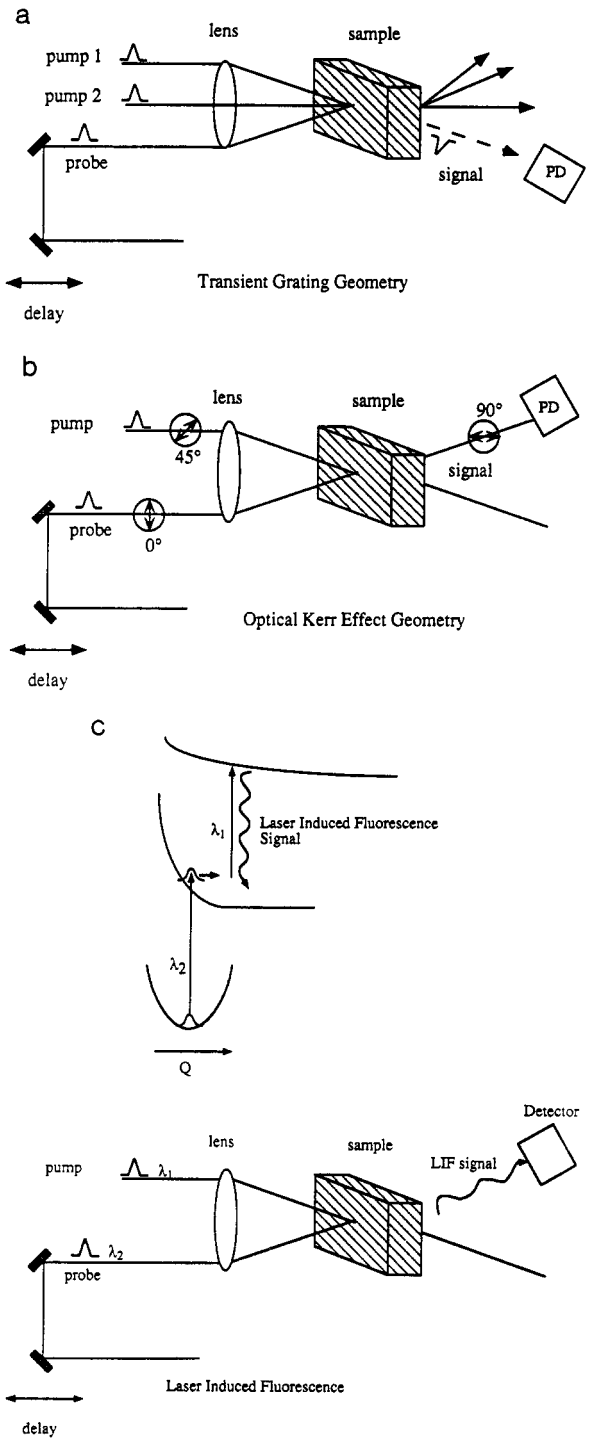

Figure 2. Part a shows time-delayed four-wave mixing or "transient grating" experimental geometry. The two excitation pulses form a spatially-varying (grating) pattern which defines the scattering wavevector **q**. The time-delayed probe pulse is coherently scattered ("diffracted") to provide the signal. Part b shows the pump–probe experimental geometry, with several types of measurement indicated. Part c shows the laser-induced fluorescence or ionization geometry. Fluorescence or ionization induced by the probe pulse is measured, providing a method for determining the weak time-dependent absorpiton strength.

The four-wave mixing experimental setup offers extensive control over which material excitations are excited and probed through variation of the light polarizations. This is true for coherent scattering experiments with long pulses or cw light as well as with ultrashort pulses and has been reviewed extensively from the point of view of coherent light scattering (in which case the emphasis is on Raman-scattering differential polarizabilities[11] which are tensor quantities) and nonlinear optics[7] (in terms of nonlinear optical polarizabilities and their tensor components). The main results are intuitive. For example, with all polarizations parallel to each other and perpendicular to the scattering plane (i.e. polarizations all vertical "V"), vibrational modes which give rise to polarization-preserved ("polarized") light scattering are excited and monitored. With perpendicular (VH) excitation pulses and perpendicular (e.g. V and H) probe and signal pulses, vibrational modes active in depolarized light scattering are observed. The results of nonorthogonal polarization combinations are often not so obvious,[12,13] and in some cases selected contributions to signal can be emphasized or canceled. Some examples of these possibilities will be illustrated below.

b. Probing Following a Single Excitation Pulse. When a single excitation pulse is used, the excitation profile is spatially uniform rather than spatially periodic as in crossed-pulse excitation. Impulsive stimulated scattering occurs in the forward direction through mixing among frequency *and wavevector* components of the incident pulse. In this case, the vibrational wavevector **q** is parallel to the excitation pulse propagation wavevector inside the sample **k**, i.e. $\mathbf{q} = \mathbf{k}(\omega/\omega_L)$ where ω and ω_L are the vibrational and (central) optical frequencies, respectively. The vibrational wavevector magnitude reflects the fact, through stimulated scattering, frequency components of the excitation pulse emerge from the sample with slightly lower (Stokes-shifted) frequencies and with correspondingly lower wavevectors. A simple real-space picture is also appealing. The excitation pulse reaches the front of the sample first, initiating coherent vibrational motion there, and later reaches the middle and the back of the sample where the phase of coherent vibrational motion is linearly retarded. The distance d that the excitation pulse travels inside the sample during a single oscillation period gives the vibrational period in space (the vibration wavelength) and therefore the wavevector magnitude q, i.e. $d = 2\pi/q$. Of course these same effects occur in transient grating excitation as well, and so the phonon wavevectors have a small forward component in addition to the transverse component $\pm q$. The forward component is negligible except at extremely small scattering angles. Single-pulse excitation can be thought of as the zero-degree limit of transient grating excitation, at which the transverse wavevector component vanishes completely to leave only the small forward wavevector component.

A variety of detection methods have been used following excitation with a single pulse rather than a pair of pulses. Coherent scattering of a probe pulse which is collinear with the excitation pulse can still occur, but the scattered signal is collinear with the unscattered probe light. Although separation of the signal based on propagation direction is not possible, separation can be based on polarization, frequency shift, or other changes.

i. Polarization Discrimination: Optical Kerr Effect. The most common form of detection involves polarization discrimination as shown in Figure 2b. The optical Kerr effect utilizes an excitation pulse linearly

polarized at an angle we will call 45° and a nearly collinear probe pulse polarized at 0°, while the transmitted probe light is passed through a crossed polarizer to detect signal polarized at 90°. This could be thought of as the zero-angle limit of a transient grating experiment with V and H polarized excitation pulses, which when collinear yield the 45°-polarized excitation light. As in the V–H transient grating experiment, the coherently scattered probe light polarization is rotated 90° relative to the incident probe light. In some cases the final polarizer is set at not quite 90° to permit some unscattered probe light to be transmitted and to act as an optical heterodyne component which can facilitate signal detection.

ii. Frequency Discrimination. Since the coherently scattered probe light is frequency shifted, it can be spectrally analyzed to permit monitoring of vibrational motion as illustrated in Figure 2c. However the frequency shift is generally within the spectral bandwidth of the incident probe pulse, so the shifted and unshifted components of the emerging probe pulse overlap spectrally and interfere with each other. The resulting spectrum of the transmitted light depends on the temporal delay between the excitation and probe pulses. To understand the results, it is useful to consider that the probe pulse, just like the excitation pulse, exerts an impulsive driving force on a vibrational mode of the sample. However, unlike the excitation pulse, the probe pulse encounters the sample already undergoing coherent vibrational oscillations. The force exerted by the probe pulse may be in phase with the coherent vibrations, in which case the vibrational motion is amplified, or the force may be out of phase in which case it opposes the motion already under way and the vibrational motion is reduced in coherent amplitude. In the former case, the probe pulse imparts energy to the vibrational mode and emerges from the sample red-shifted. In the latter case, the probe pulse takes energy away from the vibrational mode and emerges blue-shifted. The spectral profile of the probe pulse "wags" back and forth as a function of the probe pulse delay, alternating at the vibrational frequency between blue- and red-shifting.[2,14]

The frequency shifting of the probe pulse can also be considered from a purely nonlinear optics point of view as the consequence of the time-dependent oscillations in the refractive index of the sample. Time-dependent changes in the refractive index of a sample, whether caused by coherent vibrations or other events, cause frequency shifting ("chirping") of light within the sample. For example, this is the basis for white-light continuum generation by femtosecond pulses due to intensity-induced changes in refractive index.[15]

iii. Other Measurements of Refractive Index Changes. Several alternative methods for detecting changes in the real part of the refractive index have been demonstrated. One is to measure the time required for the probe pulse to pass through the sample.[16] Coherent vibrational oscillations in the sample cause time-dependent changes in the refractive index which can be detected by inserting the sample into one arm of an interferometer. The optical path length of that arm undergoes time-dependent oscillations and decay. Another method is based on the fact that the single excitation pulse is most intense at its center, ideally with a Gaussian spatial profile. Coherent vibrational displacements and the associated refractive index changes are largest at the center, giving rise to a lensing effect which is similar to the "thermal" lensing resulting from heating and thermal expansion induced by a single absorbed pulse.[17] In this case the extent of lensing depends on the oscillatory vibrational displacements. As in thermal lensing experiments, vibrational oscillations and decay can be monitored through measurement of time-dependent probe transmission through a pinhole or of the deflection angle of a probe beam which is not collinear.

2. Probing the Imaginary Part of the Refractive Index

a. Transient Grating Excitation and Probing. This method has been used in a few cases to detect coherent vibrational motion through changes in the imaginary as well as real part of the refractive index. The experimental arrangement is the same as that described earlier, with the difference that the probe wavelength is resonant with an electronic transition. In this case amplitude as well as phase grating effects contribute to diffraction. The excitation pulses are generally resonant as well, and the coherent vibrations monitored are those initiated through absorption into an electronic excited state.

b. Transient Absorption and Reflection. By far the most common method for observation of excited-state vibrational motion in condensed phases has been measurement of time-resolved absorption or reflection. In terms of Figure 1, parts b and c, the excited-state wavepacket will show differing amounts of absorption or stimulated emission depending on its instantaneous position. Measurements can be made by frequency-tuning a femtosecond probe pulse and recording the total amount of light transmitted through a sample, or by using a broadband ("white-light") continuum pulse[18–23] and spectrally analyzing the transmitted light after the sample. These cases have sometimes been referred to a "pre-dispersed" or "post-dispersed", respectively, and detailed treatments have been given concerning the information content of the results. These will be summarized below.

It is important to recognize that spectroscopic observation of coherently vibrating species which pass through well-defined nonequilibrium geometries is not identical to observation of species somehow "frozen" into the same nonequilibrium geometries. This is true regardless of any issues concerning wavepacket width, i.e. concerning the distribution of geometries sampled. Even for the same distribution of geometries, the result of an absorption (or other) spectral measurement of the coherently moving wavepacket is not the same as the result of a similar measurement on a statically distorted species. This is because of the frequency shifting of the probe pulse which was described earlier and which occurs for a resonant pulse as well as a nonresonant pulse. In fact for a resonant probe pulse the effect will often be stronger. This can be viewed as resonance enhancement of coherent Raman scattering of the pulse or as resonance enhancement of the time-dependent refractive index changes of the sample. The frequency shifts, which in the nonresonant case have very small effects on the total transmitted light intensity, have important effects on the transmitted

intensity near resonance since the probe pulse spectrum may be shifted either toward or away from the absorption maximum. This limits the precision with which time-dependent changes in the absorption spectrum can be determined and can be viewed as a consequence of the uncertainty principle.[14]

c. Transient Fluorescence. Although it has rarely been demonstrated, detection of coherent excited-state vibrational motion is possible through measurement of time-resolved fluorescence.[24] This offers some simplification over transient absorption or stimulated emission measurement since then only the electronic excited state and the ground state (and no higher-lying electronic states) are involved. In practice it is more difficult to make fluorescence measurements with sufficient time resolution.

d. Laser-Induced Fluorescence and Ionization. In the gas phase, direct determination of transient absorption is difficult and measurements of laser-induced fluorescence or ionization are far more common and convenient.[25] The experimental arrangement, shown in Figure 2d, is similar to that of a transient absorption measurement except that what is actually measured is not the absorption of the probe pulse but the amount of fluorescence or ionization induced by it. From this the absorption and the wavepacket dynamics can be deduced.

III. Theoretical Treatment of the Excitation Process

We treat nonresonant and resonant impulsive excitation classically and then quantum mechanically. The emphasis here is on vibrational phase coherence, but electronic phase coherence effects are also discussed in a later section. The treatment is presented in some detail, to clearly define the nature of the coherent state created through impulsive excitation. However, the subsequent section on experimental examples can be read easily without reference to this section. Readers not specifically interested in the theoretical description may wish to skip this section.

A. Nonresonant Excitation

We begin with an intuitive description of nonresonant excitation in quantum and classical pictures. We treat the simplest case to allow for a straightforward comparison of the two pictures. Through this comparison, we show that classical intuition can be used successfully to interpret the results of off-resonant ISS experiments. We first specify a Hamiltonian which makes use of the Placzek approximation. Using this Hamiltonian we solve the quantum mechanical equations nonperturbatively and show that the quantum and classical pictures yield identical results for the energy, momentum, and displacement when expectation values in the quantum case are considered. Because the classical and the nonperturbative quantum descriptions break down as resonance is approached, we also present a density matrix quantum mechanical treatment that deals with the excitation perturbatively. While less intuitive for the nonresonant case, this treatment is more general in that it can easily be extended to the case of resonant excitation.

1. The Exact Treatment

a. The Hamiltonian. Expansion of the Hamiltonian of the material in terms of powers of the applied electric field gives[1]

$$H = H_0 + H_1 + H_2 + \ldots \quad (1)$$

H_0 is the Hamiltonian of the isolated system, while H_1 gives rise to light absorption. H_2 describes light scattering processes, and the higher order terms describe nonlinear interactions of various sorts. Since we wish to describe light scattering only, and since we assume that the laser wavelength is far from any electronic resonance, we neglect $H_{i>2}$ and H_1. In addition, we consider only motions of nuclei that can be described in terms of normal modes. This allows for a simplified Hamiltonian and at the same time describes a wide range of phenomena such as phonons, intramolecular vibrations, and surface waves (ripplons) for example.

In this approximation, and in the limit of negligible damping, H_0 is given by

$$H_0 = \frac{1}{2}\sum_{q\alpha} P^{\alpha}(-q)\, P^{\alpha}(q) + \omega^{\alpha}(q)\, \omega^{\alpha}(q)\, Q^{\alpha}(-q)\, Q^{\alpha}(q) \quad (2)$$

Here, Q and P are the normal mode displacement and the conjugate momentum, q labels the wavevector and α labels the material mode.

H_2 is given by

$$H_2 = -\sum_{ij}\sum_{\mathbf{q}} \delta\alpha_{ij}(\mathbf{q},t)\, F_{ij}(-\mathbf{q},t) \quad (3)$$

$\delta\alpha_{ij}$ is the change in the polarizability and for first-order light scattering-active modes within the Placzek approximation[26,27] can be written as,

$$\delta\alpha_{ij}(\mathbf{q},t) = \sum_{\alpha\zeta} \frac{\partial\alpha_{ij}}{\partial Q^{\alpha}_{\zeta}} Q^{\alpha}_{\zeta}(\mathbf{q},t) \quad (4)$$

Finally, the effective force is given by

$$F_{ij}(\mathbf{q},t) = \frac{1}{8\pi} E_i(\mathbf{q},t)\, E_j(-\mathbf{q},t) \quad (5)$$

For notational convenience, we drop polarization indices, neglect the tensorial nature of the dielectric operator, and consider the evolution of a single mode. A detailed tensor, multimode treatment has been presented.[1,2] With these simplifications, we have

$$H = \frac{1}{2}(P^2 + \omega^2 Q^2) - \frac{\partial\alpha}{\partial Q} Q F(t) \quad (6)$$

This sort of effective Hamiltonian has been used extensively in the past.[27-32] With it, properties of electronic excited states are hidden in the differential polarizability, and exact solutions in the quantum case are realizable. In this way perturbative schemes are circumvented, and the treatment holds for arbitrary laser intensities.[30]

Finally, in what follows, the influence of the material on the electric field is neglected and we treat the electric field (and thus the term $F(t)$) classically in both the quantum (semiclassical) and the classical treatments.

b. The Classical Mechanical Description. The most straightforward procedure is to solve the classical equations of motion with the Hamiltonian (eq 6). This solution has been presented in detail.[1,2] In this section we solve the equations in such a way as to highlight

similarities between the classical and quantum cases. We use the Poisson bracket formalism and consider motion of a variable $a_c(t)$ somewhat artificially defined by

$$a_c(t) \equiv \left(\frac{\omega}{2\hbar}\right)^{1/2} Q + i\frac{P}{(2\hbar\omega)^{1/2}} \tag{7}$$

The evolution of this variable is determined by the Poisson bracket formulation of classical mechanics,

$$\frac{da_c(t)}{dt} = -\{H,a_c\} + \frac{\partial a_c}{\partial t} = -\left(\frac{\partial H}{\partial Q}\frac{\partial a_c}{\partial P} - \frac{\partial H}{\partial P}\frac{\partial a_c}{\partial Q}\right) \tag{8}$$

or

$$\frac{da_c(t)}{dt} = -i\omega a_c(t) + \frac{i}{(2\hbar\omega)^{1/2}}\frac{\partial \alpha}{\partial Q}F(t) \tag{9}$$

Solving this yields the evolution of $a_c(t)$,

$$a_c(t) = e^{-i\omega(t-t')}\left(a_c(t') + e^{i\omega t'}\frac{i}{(2\hbar\omega)^{1/2}}\frac{\partial \alpha}{\partial Q}\int_{t'}^{t} F(\tau)e^{i\omega\tau}\,d\tau\right) \tag{10}$$

$$= e^{-i\omega(t-t')}\,(a_c(t') + e^{-i\omega t'}\lambda) \tag{11}$$

where for ease of notation we have defined the new variable λ. From $a_c(t)$, we can easily determine the evolution of $Q(t)$, $P(t)$, and the energy density, $E(t)$, associated with the normal mode. That is

$$Q(t) = (2\hbar/\omega)^{1/2} Re(a_c(t)) \tag{12}$$

$$P(t) = (2\hbar\omega)^{1/2} Im(a_c(t)) \tag{13}$$

$$E(t) = \hbar\omega|a_c(t)|^2 \tag{14}$$

For the case that $a_c(t') = 0$ (i.e. the zero initial temperature condition), the above expressions reduce to

$$Q(t) = \left(\frac{2\hbar}{\omega}\right)^{1/2} Re(\lambda e^{-i\omega t}) = \left(\frac{2\hbar}{\omega}\right)^{1/2} |\lambda|\sin(\omega t - \varphi) \tag{15}$$

$$P(t) = (2\hbar\omega)^{1/2} Im(\lambda e^{-i\omega t}) = (2\hbar\omega)^{1/2}|\lambda|\cos(\omega t - \varphi) \tag{16}$$

$$E(t) = \hbar\omega|\lambda|^2 \tag{17}$$

with $\cos(\varphi) = Re(i\lambda)/|\lambda|$. The phase factor vanishes in the limit of $F(t) \propto \delta(t - t')$, i.e. when the excitation pulse duration is much shorter than the vibration period. We note that damping can be introduced in a phenomenological way through a modification of eq 8. In the limit of small damping rates γ (i.e. $\gamma \ll \omega$) it is easy to show that the above expressions remain valid provided that,

$$\lambda \equiv \frac{\partial \alpha}{\partial Q}\frac{i}{(2\hbar\omega)^{1/2}}\int_{t'}^{t} F(\tau)\, e^{i\omega\tau}\,d\tau \rightarrow \frac{\partial \alpha}{\partial Q}\frac{i}{(2\hbar\omega)^{1/2}}\int_{t'}^{t} F(\tau)\, e^{-\gamma(t-\tau)}e^{i\omega\tau}\,d\tau \tag{18}$$

(Note that in these expressions the factors of $\hbar$ all exactly cancel.) This classical description has been used to analyze nonresonant ISS experiments in the past and agreement with data in all cases is excellent. The relation between ISS data described in this manner and frequency-domain light scattering spectroscopy has also been described in detail.[1,2]

c. The Nonperturbative Quantum Mechanical Description. We now present a quantum mechanical solution for the system subject to the Hamiltonian given in eq 6. Although the undamped driven quantum oscillator problem was solved as early as 1948[33] and has since been solved in different ways in many different contents,[34-39] we summarize a solution which enables facile extraction of important results in a framework that allows for comparison to the classical picture presented in the previous section. We also present an extension to the weakly damped oscillator and show it to be exactly analogous to the classical case.

Defining the Heisenberg lowering and raising operators in the usual way

$$a = \left(\frac{\omega}{2\hbar}\right)^{1/2} Q + i\frac{P}{(2\hbar\omega)^{1/2}} \tag{19}$$

$$a^\dagger = \left(\frac{\omega}{2\hbar}\right)^{1/2} Q - i\frac{P}{(2\hbar\omega)^{1/2}} \tag{20}$$

we can write the Hamiltonian in eq 6 as

$$H(t) = \hbar\omega(a^\dagger(t)\,a(t) + {}^1/_2) - \frac{\partial \alpha}{\partial Q}F(t)\left(\frac{\hbar}{2\omega}\right)^{1/2}(a(t) + a^\dagger(t)) \tag{21}$$

where we have made use of the commutator properties of Q and P, and have evolved the equation with the time evolution operator U_t.

The important quantity will be the transition amplitude between an initial state labeled by z' and occupied at time t', and state z at time t. The equation of motion which determines this quantity is

$$i\hbar\frac{\partial}{\partial t}\langle z,t|z',t'\rangle = \langle z,t|H(t)|z',t'\rangle \tag{22}$$

To solve this, we use the Heisenberg equation of motion to determine $a(t)$ in terms of $a(t')$. That is, using

$$\frac{da(t)}{dt} = \frac{1}{i\hbar}[a(t),H(t)] \tag{23}$$

we find, using the commutator properties of $a(t)$ and $a^\dagger(t)$

$$\frac{da(t)}{dt} = -i\omega a(t) + \frac{i}{(2\hbar\omega)^{1/2}}\frac{\partial \alpha}{\partial Q}F(t) \tag{24}$$

which is, of course, identical to the equation of motion for the classical variable $a_c(t)$. Solving for $a(t)$ yields

$$a(t) = e^{-i\omega(t-t')}\left(a(t') + \frac{ie^{-i\omega t'}}{(2\hbar\omega)^{1/2}}\int_{t'}^{t} F(\tau)e^{i\omega\tau}\,d\tau\right) \tag{25}$$

This equation provides the temporal evaluation of the Heisenberg operators $P(t)$ and $Q(t)$, and in conjunction with eq 23 can be used to determine transition amplitudes. Assuming that the oscillator is in the $n = 0$ number eigenstate at time $t = t'$, then the probability that the oscillator is found in number state n at time t is given by

$$P_n = |\langle n,t|0,t'\rangle|^2 = \frac{(|\lambda|^2)^n}{n!}e^{-|\lambda|^2} \quad (26)$$

It cannot be over-emphasized that although eq 26 gives a probability for finding the system in the nth eigenstate at time t, the system is not prepared in a number eigenstate. As a result, this probability does not measure the chance that an oscillator reaches the nth eigenstate as a result of being acted on by the driving force. Instead, it represents the probability that *upon measurement of the oscillator energy*, a value corresponding to n quanta is observed. The system is prepared in a coherent superposition of number eigenstates, and it remains in this coherent superposition if it is left to evolve freely (i.e. no energy measurement or other perturbation is applied). This point is crucial, and its importance is made clearer subsequently.

With the zero temperature approximation, it is possible to show that a coherent state is prepared independent of the form of $F(t)$. The label of this coherent state is time dependent and is given by $\lambda(t)$. Knowing this, expressions related to position, momentum, and energy expectation values can be written down. Since coherent states are minimum uncertainty states, we only present results for the second moment (rms fluctuation) of the energy:

$$\langle Q(t)\rangle = \left(\frac{2\hbar}{\omega}\right)^{1/2} Re(\lambda e^{-i\omega t}) = \left(\frac{2\hbar}{\omega}\right)^{1/2} |\gamma|\sin(\omega t - \varphi) \quad (27)$$

$$\langle P(t)\rangle = (2\hbar\omega)^{1/2}\, Im(i\lambda e^{-i\omega t}) = (2\hbar\omega)^{1/2}\, |\lambda| \cos(\omega t - \varphi) \quad (28)$$

$$\langle E\rangle = \hbar\omega(\langle n\rangle + {}^1/_2) = \hbar\omega(|\lambda|^2 + {}^1/_2) \quad (29)$$

$$\langle \Delta E\rangle = \hbar\omega|\lambda| \quad (30)$$

where $\cos(\varphi) = Re(i\lambda)/|\lambda|$. The brackets indicate expectation value of, and eq 30 gives the rms fluctuation of the energy. These expressions are valid in the zero initial temperature limit and in the absence of damping. Relaxing the zero initial temperature assumption introduces some modifications, but does not alter eqs 27 or 28 nor does it substantially change any qualitative conclusions.[30,35,37] In addition, expressions 26–30 are valid for the weakly damped oscillator provided that the replacement specified in eq 18 is made.[40]

With these results, the similarity of the classical and quantum mechanical pictures is easily evaluated. While it is clear that both the displacements and the conjugate momenta are identical (cf. eqs 15 and 16 and 27 and 28), the energy must be discussed more carefully. First, there is, of course, a ground-state zero-point energy in the quantum case that is not present in the classical case. However, we are concerned with the magnitude of the energy deposited by the driving force. In this case, only changes in energy are important, and the ground-state energy of the quantum system is not problematic. The second point is that unlike the displacement or the momentum, the energy in the quantum case is quantized, an effect which has no analog in the classical case. Nevertheless, for a coherent state which is an eigenstate of the lowering operator with continuous eigenvalues, but which is distinctly not an energy eigenstate, the expectation value of the energy given by eq 29 is a continuous variable. If we consider changes in the expectation value of the energy, the classical picture is valid in all limits as evidenced from the similar functional dependencies of the quantum mechanical and the classical expressions given in eqs 29 and 17. This interpretation is different from one offered earlier based on identical quantitative expressions.[30,41] While the quantum mechanical description of the coherent state provides complete information about the distribution of energy eigenvalues reached upon making an energy measurement, our results show that the expectation value of the energy increases linearly with the excitation intensity in any intensity regime. The comparison between classical and quantum mechanical treatments and their interpretations is discussed further below in connection with multiple-pulse ISRS excitation.

2. The Density Matrix Approach

Although nonresonant ISRS can be treated exactly within the Plackzek approximation, it is instructive to consider the alternative approach of a perturbative expansion of the system's time-dependent density matrix. While the previous exact treatment of section III.A.1 demonstrated the concurrence of the classical and the quantum mechanical pictures of nonresonant ISRS, the strength of a perturbative approach is that it leads to a physically appealing wavepacket picture. The formalism is utilized later to consider resonant excitation where an exact treatment is not possible.

In this section, we begin with the familiar perturbative expansion of the system's time-dependent density matrix in orders of the electric field of the excitation laser. Considering a single vibrational coordinate, we work within the electric dipole approximation to expand the density matrix to second order in the field, obtaining expressions for the ground-state vibrational coherences created through impulsive excitation. The expressions are then recast into a wavepacket picture following the formalism developed by Heller.[48,49] The section concludes by comparing the expectation values of the system's position and momentum operators calculated in the previous exact treatment to those calculated in the present perturbative treatment.

a. The Time-Dependent Density Matrix. Various authors have utilized the density matrix approach to describe time-resolved optical spectroscopies.[42–47] We follow the treatment of Fain and Lin[46] (equivalent in this respect to that of Yan and Mukamel[30,44]) as it leads to a straightforward comparison to the results of section III.A.1.

The Hamiltonian is expressed as

$$H = H_0 + H_{int} \quad (31)$$

where H_0 denotes the unperturbed Hamiltonian and H_{int} represents the interaction Hamiltonian

$$H_{int} = -\mu(q)\, E(t) \quad (32)$$

where $\mu(q)$ is the coordinate-dependent transition dipole moment operator and $E(t)$ is the electric field.

Ignoring any relaxation effects, the time evolution of the density matrix is dictated by the quantum-mechanical Liouville equation:

$$i\hbar\frac{\partial\rho}{\partial t} = [H,\rho] \quad (33)$$

By using the interaction representation, the time

evolution of the transformed density matrix $\tilde{\rho}(t)$ is expressed as

$$i\hbar\frac{\partial\tilde{\rho}}{\partial t} = [\tilde{V}(t),\tilde{\rho}] \tag{34}$$

where the density operator and the potential are expressed in the interaction ($\tilde{\rho}$) representation through the transformations

$$\tilde{\rho}(t) = U^{+}(t)\,\rho(t)\,U(t)$$

$$\tilde{V}(t) = U^{+}(t)\,V(t)\,U(t)$$

and $U(t)$ is the unitary transformation

$$U(t) = e^{-iH_0t/\hbar}$$

The integral solution of eq 34 is then

$$\Delta\tilde{\rho}(t) = \tilde{\rho}(t) - \tilde{\rho}(t_i) = \frac{1}{i\hbar}\int_{t_i}^{t}[\tilde{V}(t_1),\tilde{\rho}(t_1)]\,dt_1 \tag{35}$$

Perturbatively solving eq 35 in orders of the interactions potential, $\tilde{V}(t)$, yields

$$\Delta\tilde{\rho}^{(n+1)}(t) = \frac{1}{i\hbar}\int_{t_i}^{t}[\tilde{V}(t_1),\tilde{\rho}^{n}(t_1)]\,dt_1 \tag{36}$$

assuming that

$$\tilde{\rho}^{(0)}(t) = \tilde{\rho}^{(0)}(t_i) = \tilde{\rho}^{(0)}(-\infty) \tag{37}$$

As discussed previously, the impulsively initiated coherent vibrational motion is a result of vibrational coherences created within each electronic state. To obtain an expression for the vibrational coherences created, we must solve for ρ to second order. Equation 36 yields

$$\Delta\tilde{\rho}^{(2)}(t) = \left(\frac{1}{i\hbar}\right)^2\int_{-\infty}^{t}dt_1\int_{-\infty}^{t_1}dt_2\,[\tilde{V}(t_1),[\tilde{V}(t_2),\rho(-\infty)]] \tag{38}$$

To apply this result specifically to the case of impulsive excitation, the interaction energy is expressed as

$$V(t) = -\mu(Q)\,E(t) = \mu(Q)[E(\Omega)\,e^{-i\Omega t} + E(-\Omega)\,e^{i\Omega t}]f(t)$$
$$= [V(\Omega)\,e^{-i\Omega t} + V(-\Omega)\,e^{i\Omega t}]f(t) \tag{39}$$

where $f(t)$ describes the temporal profile of the ultrashort pulse.

Using the preceding framework, Fain and Lin[46] obtain the following expression for the vibrational coherence created in off-resonant ISRS:[43]

$$\Delta\rho_{0v;0v'} = \frac{i}{\hbar^2}\left\{\sum_{l\neq 0}\sum_{w}\left[\frac{\langle 0v|V(\Omega)|lw\rangle\langle lw|V(-\Omega)|0v'\rangle}{\omega_0-\omega_l-\Omega} + \frac{\langle 0v|V(-\Omega)|lw\rangle\langle lw|V(\Omega)|0v'\rangle}{\omega_0-\omega_l+\Omega}\right]\times(\rho_{0v';0v'}-\rho_{0v;0v})\int_{-\infty}^{\infty}f^2(t)\,dt\right\} \tag{40}$$

where 0 and l denote the ground and higher electronic states, v, v', and w represent vibrational states within the ground and higher electronic states, $\rho_{0v';0v'}$ and $\rho_{0v;0v}$ are elements of density matrix of the system before any interaction with light, and the system was assumed to initially be in the ground electronic state with its density matrix strictly diagonal. (Since we are concerned with the effect of ultrashort pulses and are ignoring any relaxation processes, the system dynamics after the pump pulses have passed are calculated by extending the limits of integration to $(-\infty,+\infty)$.)

The expression for $\rho^{(2)}(t)$ allows us to calculate the coherent displacement that is induced by ultrashort pulses. Before we explicitly determine the form of the displacement, we use eq 40 to present a wavepacket interpretation of nonresonant ISRS that is analogous to the interpretation developed for cw Raman processes.

b. A Wavepacket Interpretation of nonresonant ISRS. Fain and Lin's result is easily recast into a wavepacket framework. We find that as in cw off-resonant Raman scattering, off-resonant ISRS results from a distortion of the wavepacket describing the initial state of the system by the coordinate-dependent electronic transition dipole moment.

Following the work of Heller,[48,49] the Kramers–Heisenberg–Dirac summation over vibronic states that appears in the brackets of eq 40 can be manipulated to reexpress the coherence created through impulsive excitation, $\Delta\tilde{\rho}_{0v;0v'}$ as

$$\Delta\tilde{\rho}_{0v;0v'} =$$

$$\frac{i}{\hbar^2}\left\{\frac{i}{\hbar}\int_0^{\infty}dt\,\langle\phi_f|\phi_i(t)\rangle\,e^{i(\omega_0+\Omega)t} + \langle\phi_f|\phi_i(t)\rangle\,e^{i(\omega_0-\Omega)t}\right\}\times$$

$$E(\Omega)E(-\Omega)(\rho_{0v';0v'}-\rho_{0v;0v})\{\int_{-\infty}^{\infty}f^2(t)\,dt\} \tag{41}$$

where

$$|\phi_i\rangle = \mu_{10}(Q)|0v'\rangle$$

$$|\phi_i(t)\rangle = e^{-iH_1t/\hbar}|\phi_i\rangle \tag{42}$$

$$\langle\phi_f| = \langle 0v|\mu_{01}(Q)$$

The first term of the sum inside the brackets corresponds to the resonant term of the KHD expression while the second term corresponds to the antiresonant term. In eq 41, the magnitude of the coherence depends on the excitation intensity, $\int_{-\infty}^{\infty}f^2(t)\,dt$, and the overlap integral. As in off-resonance cw Raman processes, there is little contribution to the overlap integral from excited-state propagation as the propagation time for the wavepacket $\phi_i(t)$ on the excited-state surface is inversely related to the mismatch between the excitation energy $\hbar\Omega$ and the energy separation $\hbar(\omega_1-\omega_0)$ of the ground and excited surface.[48] Instead it is the distortion of the initial wavepacket by the coordinate-dependent electronic transition dipole moment (seen in $\mu_{10}(Q)|0v'\rangle$) that governs the magnitude of the coherence in off-resonant ISRS.

c. The Expectation Values of the Position and Momentum Operators. We return to eq 40 to calculate the expectation value of the displacement operator to emphasize the initiation of coherent vibrational motion through impulsive excitation. We then compare the calculated expectation values of the position and momentum operators within the perturbative treatment of off-resonant ISRS to those calculated in the exact treatment.

Equation 40 can be reexpressed in terms of the molecular polarizability $\alpha(\Omega)$.[50] $\alpha(\Omega)$ for a molecule

under the influence of a field oscillating at frequency Ω is

$$\alpha(\Omega) = \sum_{\ell}\left[\frac{\langle 0|\mu|\ell\rangle\langle\ell|\mu|0\rangle}{\hbar\omega_0 - \hbar\omega_\ell - \hbar\Omega} + \frac{\langle 0|\mu|\ell\rangle\langle\ell|\mu|0\rangle}{\hbar\omega_0 - \hbar\omega_\ell + \hbar\Omega}\right] \quad (43)$$

We can also expand the polarizability in normal coordinates, q_i:

$$\alpha = \alpha_0 + \sum_i\left(\frac{\partial\alpha}{\partial q_i}\right)_0 q_i + \frac{1}{2}\sum_{ij}\left(\frac{\partial^2\alpha}{\partial q_i\partial q_j}\right)_0 q_i q_j + \ldots \quad (44)$$

As in eq 4 of section III.A.1.a, we keep only the first derivative term and consider only one normal coordinate, and use eqs 43 and 44 to rewrite eq 40 as

$$\Delta\tilde{\rho}^{\mathrm{nr}}_{0v;0v'} = \frac{i}{\hbar}(\rho_{0v';0v'} - \rho_{0v;0v})\left(\frac{\partial\alpha}{\partial q}\right)q_{v;v'}T \quad (45)$$

where $T = \int_{-\infty}^{\infty} f^2(t)\,\mathrm{d}t$.

Assuming that only the ground vibrational state is populated initially (i.e. $\rho_{00;00} = 1$), the only nonzero elements of $\Delta\tilde{\rho}$ are

$$\Delta\tilde{\rho}_{01;00} = \frac{i}{\hbar}\left(\frac{\partial\alpha}{\partial q}\right)|E(\Omega)|^2\, q_{00;01}T$$

$$\Delta\tilde{\rho}_{00;01} = \frac{i}{\hbar}\left(\frac{\partial\alpha}{\partial q}\right)|E(\Omega)|^2\, q_{01;00}T \quad (46)$$

We can calculate the expectation value of an operator $O(t)$ from

$$\langle O(t)\rangle = \sum_{v,v'}\Delta\tilde{\rho}_{0v;0v'}(t)\; O_{0v';0v}(t)\; \mathrm{e}^{i\omega_{0v;0v'}t} \quad (47)$$

The expectation value of the position operator is then

$$\langle Q(t)\rangle = T\left(\frac{\partial\alpha}{\partial q}\right)|E(\Omega)|^2\,\frac{1}{\omega_{10}}\sin\omega_{10}t \quad (48)$$

As expected the average displacement oscillates with the frequency of the vibrational mode and with an amplitude proportional to the intensity of the excitation pulse.

In a similar fashion the expectation value of the momentum operator is determined to be

$$\langle P(t)\rangle = T\left(\frac{\partial\alpha}{\partial q}\right)|E(\Omega)|^2\,\frac{1}{\omega_{10}}\cos\omega_{10}t \quad (49)$$

For the sake of completeness we conclude this section by comparing results of the perturbative and exact treatments. Recall from the previous exact treatment that the expectation values for the position and momentum were found to be (eqs 27 and 28):

$$\langle Q(t)\rangle_{\mathrm{exact}} = \left(\frac{2\hbar}{\omega}\right)^{1/2}|\lambda|\sin(\omega t - \varphi) \quad (50)$$

$$\langle P(t)\rangle_{\mathrm{exact}} = (2\hbar\omega)^{1/2}|\lambda|\cos(\omega t - \varphi) \quad (51)$$

where

$$\lambda = \left(\frac{\partial\alpha}{\partial q}\right)\frac{1}{(2\hbar\omega)^{1/2}}\int_{t'}^{t}F(\tau)\,\mathrm{e}^{i\omega\tau}\,\mathrm{d}\tau \qquad F(\tau) \propto E_1(\tau)\,E_2(\tau)$$

$$\cos(\varphi) = Re(i\omega)/|\lambda| \qquad \omega = \omega_{10}$$

By ignoring high-frequency terms in $F(t)$ (i.e., those that oscillate at $2\Omega t$) and assuming that $\omega\tau \ll 1$ (i.e. impulsive excitation), λ becomes

$$\lambda = \left(\frac{\partial\alpha}{\partial q}\right)\frac{1}{(2\hbar\omega)^{1/2}}|E(\Omega)|^2 T \quad (52)$$

Assuming that λ is strictly real, we can rewrite $\langle Q(t)\rangle_{\mathrm{exact}}$ and $\langle P(t)\rangle_{\mathrm{exact}}$ as

$$\langle Q(t)\rangle_{\mathrm{exact}} = T\left(\frac{\partial\alpha}{\partial q}\right)|E(\Omega)|^2\,\frac{1}{\omega}\sin(\omega t) \quad (53)$$

$$\langle P(t)\rangle_{\mathrm{exact}} = T\left(\frac{\partial\alpha}{\partial q}\right)|E(\Omega)|^2\cos(\omega t) \quad (54)$$

We see that in the limit of impulsive excitation, the exact and perturbative treatments give the same values for the expectation values of the position and momentum. However, the agreement of eqs 50 and 51 and eqs 53 and 54 does not imply that only the $v = 0$ and $v = 1$ vibrational states are involved in the coherent state created by the pump pulse. This is made clear by calculating $\rho_{00;01}(t)$ using the exact coherent state derived in section III.A.1.c):

$$\rho(t) = |0,t';t\rangle\langle 0,t';t|$$

$$\begin{aligned}\rho_{00;01}(t) &= \langle 00|0,t';t\rangle\langle 0,t';t|01\rangle \\ &= i\mathrm{e}^{i\omega t}\left(\frac{\partial\alpha}{\partial Q}\right)\frac{1}{(2\hbar\omega)^{1/2}}\mathrm{e}^{-|\lambda|^2}\int_{t'}^{t}\mathrm{d}\tau\, F(\tau) \\ &= i\mathrm{e}^{i\omega t}\left(\frac{\partial\alpha}{\partial Q}\right)\frac{1}{(2\hbar\omega)^{1/2}}\mathrm{e}^{-|\lambda|^2}T|E(\Omega)|^2\end{aligned} \quad (55)$$

where $|0,t';t\rangle$ re presents the state at time t after originating in the $n = 0$ eigenstate at time t'. Comparing this result to the perturbative result

$$\rho_{00;01}(t) = i\mathrm{e}^{i\omega t}\left(\frac{\partial\alpha}{\partial Q}\right)\frac{1}{(2\hbar\omega)^{1/2}}T|E(\Omega)|^2 \quad (56)$$

we see that a second-order perturbative treatment (assuming a harmonic oscillator system) yields the correct values for the expectation values of position and momentum because it only considers the $v = 0$ and $v = 1$ states and thereby overemphasizes their contributions. It must be stressed that impulsive excitation creates a coherent state that involves all vibrational states. Although in the weak field limit of ISRS the contribution from states higher than $v = 1$ is vanishingly small, retaining the complete expression for the coherent state is essential for a complete understanding of the effects of multiple excitation pulses or even the effects of varying the intensity $|E(\Omega)|^2$. This point is stressed in the next section which calculates the evolution of the coherent state when multiple excitation pulses are used.

3. Multiple Pulse Excitation

Although the results of sections III.A.1.2 were derived considering only a single vibrational mode, in general all modes with energies contained within the bandwidth of the excitation pulses are coherently excited. It is often desirable to selectively excite and probe a single

mode. The technique of multiple-phase ISRS achieves this selectivity.[112,113] Multiple-pulse ISRS experiments utilize an appropriately timed sequence of excitation pulses to repetitively drive a selected vibrational mode. This excitation scheme allows for mode selectivity and energy amplification of the oscillators, treated collectively or individually. These features are most accurately described quantitatively using the exact quantum mechanical results given in section III.A. Using these expressions, we write the energy expectation value and the energy eigenvalue probability distribution as functions of time as the excitation pulse train passes through the sample. These results are valid for each individual material oscillator as well as for an ensemble of oscillators.

a. Mode Selectivity. To demonstrate mode selectivity, the effects of detuning on the energy and amplitude achieved in a multiple pulse experiment are examined. We consider a series of evenly spaced pulses of equal intensity and Gaussian temporal profile. This is described by the force $F(t)$

$$F(t) = C\left[\sum_n \exp\left(\frac{-(t-nT)^2}{t_p^2} - \frac{n^2}{N_p^2}\right)\right] \quad (57)$$

which was used in the previously reported[51] data analysis; t_p gives a measure of the pulse widths, N_p is related to the number of pulses in the train, T gives the temporal spacing of the pulses, and C gives the amplitude. By using this function and requiring that $t' \rightarrow -\infty$, the expression for λ which includes damping becomes

$$\lambda \equiv \frac{\partial\alpha}{\partial Q}\frac{i}{(2\hbar\omega)^{1/2}}\int_{t'}^{t} F(\tau)\, e^{-\gamma(t-\tau)}\, e^{i\omega\tau}\, d\tau \quad (58)$$

$$= C'\sum_n \exp\left\{-\frac{n^2}{N_p^2} + i\omega nT + \gamma nT\right\} \times \operatorname{erfc}\left\{\frac{(i\omega+\gamma)t_p}{2} - \frac{(t-nT)}{t_p}\right\} \quad (59)$$

with

$$C' = \frac{\partial\alpha}{\partial Q}\frac{iC}{(2\hbar\omega)^{1/2}}\pi^{1/2}\frac{t_p}{2}\exp\left\{\frac{(\omega+i\gamma)^2 t_p^2}{4} - \gamma t\right\} \quad (60)$$

and where erfc() is the complementary error function.

By using this equation with $\gamma = 0$, the energy was calculated and is plotted in Figure 3 as a function of time as the excitation pulse train passes through the system for resonant pulse separation. From this we see that the energy increases upon arrival of each pulse in the pulse train. By performing similar calculations for a variety of excitation pulse timings, we demonstrate that only oscillations with frequencies resonant with the pulse train are amplified. These results are given in Figure 4.

As another way to demonstrate mode selectivity, we calculate the energy per oscillator after the pulse train has passed through the system. Evaluating λ in the zero damping and long time limits yields

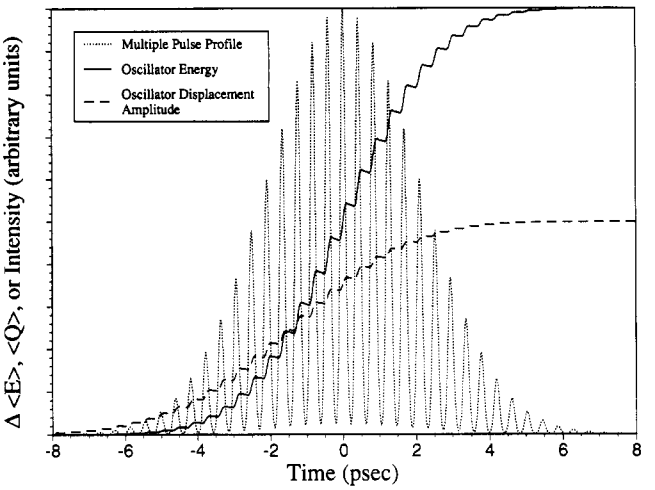

Figure 3. Simulation of $\Delta\langle E\rangle$ and $\langle Q\rangle$ as functions of time as a pulse train timed to match a vibrational resonance passes through the sample. The pulse separation is 419 fs and the frequency of the oscillator is 0.015 rad/fs. The profile of the pulse train is also shown.

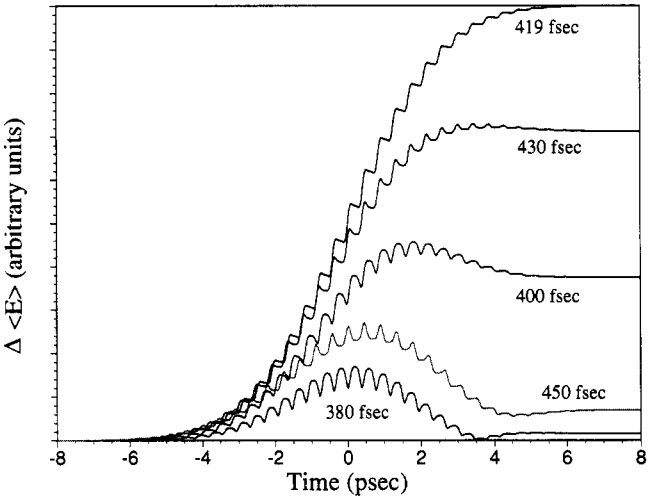

Figure 4. Simulation of $\Delta\langle E\rangle$ as a function of time as differently timed pulse trains pass through the sample. Enhancement of $\Delta\langle E\rangle_{final}$ for resonant pulse separation is clearly evident. This demonstrates the mode selectivity of multiple-pulse ISRS.

$$\lambda = 2C'\sum_n \exp\left\{-\frac{n^2}{N_p^2} + inT\omega\right\} = 4C'\sum_{n>0}\exp\left\{-\frac{n^2}{N_p^2}\right\}\cos(nT\omega) + 2C' \quad (61)$$

The final energy is

$$\langle E\rangle_{final} \propto |\lambda|^2 = \left[2\sum_{n>0}\exp\left\{-\frac{n^2}{N_p^2}\right\}\cos(nT\omega) + 1\right]^2 \quad (62)$$

When written in this manner, it is more easily seen that the final energy is maximized when ωT is equal to an even multiple π, (i.e. when the vibrational mode is driven in phase by the sequence of pulses) while the energy is minimized when ωT is equal to an odd multiple of π

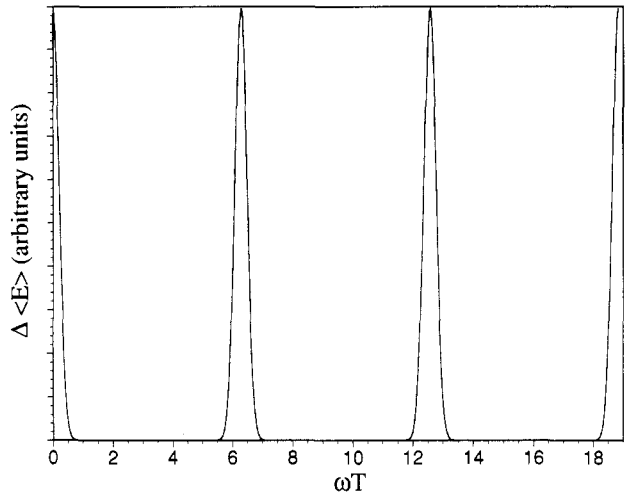

Figure 5. $\Delta\langle E\rangle_{\text{final}}$ as a function of ωT, the product of the oscillator frequency and the pulse separation. Amplification occurs only for resonant timings. This demonstrates the mode selectivity of multiple-pulse ISRS.

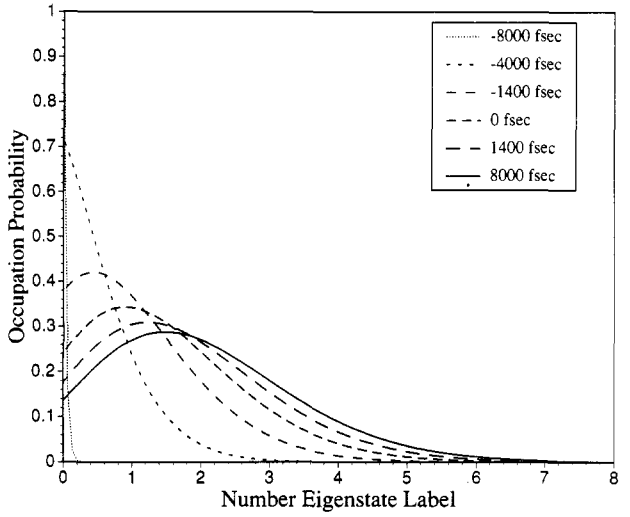

Figure 6. Number eigenstate probability distribution at various times as a reasonantly timed excitation pulse train passes through the sample. The distribution contains increasing amplitudes on higher eigenstates as the pulse train continues.

(i.e. when the mode is driven out of phase). For clarity the final energy was calculated using eq 62 and is plotted as a function of ωT in Figure 5.

Finally, although to this point we have presented results in terms of the energy expectation value which is a continuous variable, the fact that the energy is quantized must not be overlooked. For this reason, we present some of the information given in Figure 3 in terms of probabilities and number states in Figure 6. Note here that we have scaled the magnitude of the driving force to allow for a convenient illustration of the results.

b. Energy and Displacement Amplification. From the previous section, it is clear that the energy of each oscillator increases as the resonant pulse train excites the system. For appropriately timed multiple pulse sequences it is easy to show that the increase is directly proportional to the square of the impulse of the driving force. The impulse of a force is just the integral of the force over all times. For the forcing function given in eq 57, the impulse is given by

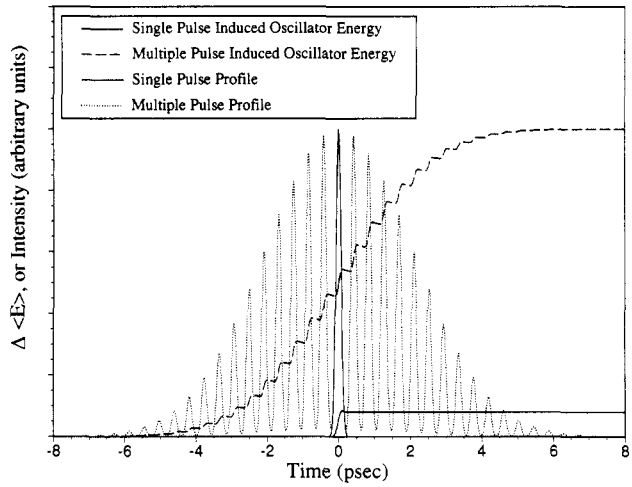

Figure 7. $\Delta\langle E\rangle$ as a function of time for a resonant pulse train and for a single pulse whose intensity maximum is equal to that of the pulse sequence. The most intense pulses in the pulse train (dotted curve) is identical to the single pulse (solid curve). The vibrational energy increases with each pulse of the pulse train. This figure demonstrates that the increase in final energy is due to an increase in the impulse of the force, or equivalently, in the excitation pulse-train area.

$$I \equiv \int_{-\infty}^{\infty} F(t)\,dt = \sum_n \exp\left\{-\frac{n^2}{N_p^2}\right\} \tag{63}$$

For resonant driving forces, the final energy (using eq 62 with ωT equal to an integer times 2π) becomes

$$\langle E\rangle_{\text{final}} \propto \left[2\sum_{n>0} \exp\left\{-\frac{n^2}{N_p^2}\right\} + 1\right]^2 = \left[\sum_n \exp\left\{-\frac{n^2}{N_p^2}\right\}\right]^2 \propto I^2 \tag{64}$$

Therefore, the expectation value of the energy of each oscillator increases as the square of the pulse area of the train. In other words, a sequence of 10 pulses prepares each oscillator in a coherent state characterized by an energy expectation value that is a factor of 100 larger than that of the state reached with a single pulse of the same peak intensity. This result is illustrated in Figure 7 through comparison of the energy for a multiple pulse case ($N_p = 7$) and for a single pulse case ($N_p = 0.25$) when the peak intensities have the same value (which may be limited in practice by the sample damage threshold). In addition, since the displacement and momentum amplitudes are proportional to λ, the qualitative conclusions reached for the energy given in this and the last section are also valid for the displacement and momentum. In other words, from experimentally measured increases in displacement amplitude, one can infer a corresponding increase in the energy.

While these conclusions are valid for the undamped oscillator, it is straightforward to include damping. Qualitatively, when there is finite damping, the oscillator energy after excitation with a reasonantly timed multiple pulse train is no longer simply proportional to the impulse of the force. Instead, after a given number

of excitation pulses pass through the sample, a maximum energy level is reached, and more excitation pulses merely act to maintain this quasi-steady-state energy level. This maximum occurs because energy is lost from the system at an exponential rate (note the prefactor in the sum in eq 59). In other words, damping causes the oscillators to lose memory of the early pulses in a long train. This can be seen analytically. For simplicity, when there is a finite number of pulses in the train (n_{max}) and the pulses are all of equal intensity (i.e. N_p large), then the energy shortly after the last pulse has passed through the sample is dominated (for sufficiently large γT) by the following term

$$\langle E(t=n_{max}T\rangle \propto |\lambda(t=n_{max}T)|^2 \approx |\frac{\partial\alpha}{\partial Q}\frac{C}{(2\hbar\omega)^{1/2}}\pi^{1/2}\frac{t_p}{2}\times \exp\left\{\frac{(\omega+i\gamma)^2 t_p^{\,2}}{4}\right\}\mathrm{erfc}\left(\frac{i\omega t_p}{2}+\frac{\gamma t_p}{2}\right)|^2 \quad (65)$$

which, in contrast to the undamped case, is independent of n_{max}. For smaller values of γT, more terms in the summation given in eq 59 must be considered. However, only a relatively small number of these terms will be nonnegligible, and the final result will still be independent of n_{max}.

B. Resonant Excitation

In the case of resonant excitation the density matrix approach leads to an appealing picture of ISRS. Because of the resonance condition, only the ground and resonant excited electronic states play significant roles in the time evolution of the density matrix. The vibrational coherences are then easily interpreted within the framework of propagating wavepackets. The excitation pulse transfers a ground-state bra (or ket) wavepacket to the excited state where it propagates for the duration of the pulse. Ground-state vibrational coherences are found to result from the overlap between the original ground-state ket (or bra) and the propagating bra (or ket) wavepacket transferred back down to the ground state by the second interaction with the electric field. Excited state coherences result from the overlap between the propagating bra (or ket) wavepacket and the original ground-state ket (or bra) wavepacket transferred to the excited state by the second interaction.

1. The Time-Dependent Density Matrix

Following the same formalism developed in section III.A.2, we rewrite the expression for $\rho(t)$ from eq 4 as:

$$\rho(t) = \frac{1}{i\hbar}\int_{t_i}^{t} dt_1\, U(t-t_1)[V(t_1),\rho(t_1)]U^{+}(t-t_1) + U(t-t_0)\,\rho(t_0)\,U^{+}(t-t_0) \quad (66)$$

We explicitly consider H_0 as the sum over the Hamiltonia of the individual potential surfaces, i.e. $H_0 = h_0 + h_1$, where h_0 (h_1) is the Hamiltonian for the ground (excited) electronic surface.[47] Assuming that the system is initially in its ground state and its density matrix is diagonal, ρ to second order is calculated to be

$$\rho^{(2)}_{0;0}(t) = \frac{1}{i\hbar}\int_{-\infty}^{t} dt_1\, e^{-ih_0(t-t_1)/\hbar}(V_{01}(t_1)\,\rho^{(1)}_{1;0}(t_1) - \rho^{(1)}_{0;1}(t_1)\,V_{10}(t_1))e^{ih_0(t-t_1)/\hbar} \quad (67)$$

$$\rho^{(2)}_{1;1} = \frac{1}{i\hbar}\int_{-\infty}^{t} dt_1\, e^{-ih_1(t-t_1)/\hbar}(V_{1;0}(t_1)\,\rho^{(1)}_{0;1}(t_1) - \rho^{(1)}_{1;0}(t_1)\,V_{0;1}(t))e^{ih_1(t-t_1)/\hbar} \quad (68)$$

$$\rho^{(2)}_{0;0}(t) = \left(\frac{1}{i\hbar}\right)^2\int_{-\infty}^{t} dt_1\int_{-\infty}^{t_1} dt_2\,\{e^{-ih_0(t-t_1)/\hbar}\times V_{01}(t_1)e^{-ih_1(t_1-t_2)/\hbar}V_{10}(t_2)\,\rho_{00}e^{ih_0(t_1-t_2)/\hbar}e^{ih_0(t-t_1)/\hbar} - e^{ih_0(t-t_1)/\hbar}e^{-ih_0(t_1-t_2)/\hbar}\rho_{00}V_{01}(t_2)e^{-ih_1(t_1-t_2)/\hbar}\times V_{10}(t_1)e^{ih_0(t-t_1)/\hbar}\} \quad (69)$$

$$\rho^{(2)}_{1;1} = \left(\frac{1}{i\hbar}\right)^2\int_{-\infty}^{t} dt_1\int_{-\infty}^{t_1} dt_2\,\{e^{-ih_1(t-t_1)/\hbar}\times V_{01}0(t_1)e^{-ih_0(t_1-t_2)/\hbar}\rho_{0;0}V_{0;1}(t_2)e^{ih_1(t_1-t_2)/\hbar}e^{ih_1(t-t_1)/\hbar} - e^{-ih_1(t-t_1)/\hbar}e^{-h_1(t_1-t_2)}V_{10}(t)\rho_{0;0}e^{ih_0(t-t_1)/\hbar}V_{01}(t_1)e^{ih_1(t-t_1)/\hbar}\} \quad (70)$$

2. A Wavepacket Interpretation of Resonant ISRS

The expressions for the ground- and excited-state vibrational coherences given in eqs 69 and 70 are easily interpreted in terms of propagating wavepackets. Rewriting $\rho^{(2)}_{0;0}(t)$ as

$$\rho^{(2)}_{0;0}(t) = \left(\frac{1}{i\hbar}\right)^2\int_{-\infty}^{t} dt_1\int_{-\infty}^{t_1} dt_2\,\{e^{-ih_0(t-t_1)/\hbar}\times V_{01}(t_1)e^{-ih_1(t_1-t_2)/\hbar}V_{10}(t_2)|0\rangle\langle 0|e^{ih_0(t_1-t_2)/\hbar}e^{ih_0(t-t_1)/\hbar} - e^{-ih_0(t-t_1)/\hbar}e^{-ih_0(t_1-t_2)/\hbar}|0\rangle\langle 0|V_{01}(t_2)e^{-ih_1(t_1-t_2)/\hbar}\times V_{10}(t_1)e^{ih_0(t-t_1)/\hbar}\} = \left(\frac{1}{i\hbar}\right)^2\int_{-\infty}^{t} dt_1\int_{-\infty}^{t_1} dt_2\,\langle 0|e^{ih_0(t-t_2)/\hbar}\times E(t_1)\mu_{01}e^{-ih_1(t_1-t_2)/\hbar}E(t_2)\mu_{10}|0\rangle - \langle 0|\mu_{01}E(t_2)e^{-ih_1(t_1-t_2)/\hbar}\times \mu_{10}E(t_1)e^{ih_0(t-t_1)/\hbar}e^{-ih_0(t-t_2)/\hbar}|0\rangle\} \quad (71)$$

we see that the coherence in the ground state is the result of the overlap between a ground state bra wavepacket and a ground state ket wavepacket that has been transferred to the excited state, propagated, and then transferred back down to the initial state. As seen in the first term of eq 71, the ket wavepacket $|0\rangle$ is first transferred to the excited state through an interaction with $E(t)\mu_{10}$ at time t_2. It then propagates under the Hamiltonian of the excited state h_1 for a time $t_1 - t_2$ until the second interaction with the light field at time t_1. $E(t_1)\mu_{01}$ then transfers the displaced and moving wavepacket to the ground-state surface. The second term of eq 71 is just the complex conjugate of the first term.

Similarly, the creation of coherences in the excited state is apparent in eq 70. Rewriting $\rho_{1;1}{}^{(2)}$ yields

$$\rho^{(2)}_{1;1} = \left(\frac{1}{i\hbar}\right)^2 \int_{-\infty}^{t} dt_1 \int_{-\infty}^{t_1} dt_2 \{e^{-ih_1(t-t_1)/\hbar} \times V_{10}(t_1) e^{-ih_0(t_1-t_2)/\hbar} |0\rangle\langle 0| V_{0;1}(t_2) e^{ih_1(t_1-t_2)/\hbar} e^{ih_1(t-t_1)/\hbar} - e^{-ih_1(t-t_1)/\hbar} e^{-h_1(t_1-t_2)/\hbar} V_{10}(t_2)|0\rangle\langle 0| e^{ih_0(t-t_1)/\hbar} \times V_{01}(t_1) e^{ih_1(t-t_1)/\hbar}\} = \left(\frac{1}{i\hbar}\right)^2 \int_{-\infty}^{t} dt_1 \int_{-\infty}^{t} dt_2 \times \{\langle 0|\mu_{01} E(t_2) e^{ih_1(t-t_2)/\hbar} e^{-ih_1(t-t_1)/\hbar} E(t_1)\mu_{10} e^{-ih_0(t_1-t_2)/\hbar}|0\rangle - \langle 0| e^{ih_0(t-t_1)/\hbar} \mu_{01} E(t_1) e^{ih_1(t-t_1)/\hbar} e^{-ih_1(t-t_2)/\hbar} E(t_2)\mu_{10}|0\rangle \quad (72)$$

Here we have the overlap between two moving wavepackets in the excited state. In the first term of eq 72, $\langle 0|$ is transferred to the excited state surface by $\mu_{01}E(t_2)$ where it propagates under h_1 until time t. Meanwhile, $|0\rangle$ remains in the ground state until time t_1 when it is also transferred to the excited state by $E(t_1)\mu_{10}$ where it propagates under h_1 until time t. Figure 8 summarizes the initiation of vibrational coherences.

In addition to the static distortion of the initial wavepacket by the coordinate-dependent transition moment that dominates the coherence in off-resonant ISRS, the coherence in resonant ISRS is enhanced by propagation of the wavepacket on the excited-state surface during the system's interaction with the ultrashort pulse.

3. Coherent Displacement in the Excited State

As seen in section III.A, off-resonant ISRS leads to oscillations in the average displacement in the ground state of a sinusoidal form. Resonant ISRS, on the other hand, induces cosinusoidal motion in both the ground and excited states. This behavior is easily seen by returning to the treatment of Fain and Lin.[46]

From eq 38, $\Delta\rho^{(2)}(t)$ in the ground and excited states on resonance are

$$\Delta\rho^{res}_{0v;0v'} = \frac{2\pi}{\hbar^2} \sum_w V(-\Omega)_{0v;n\infty} w V(\Omega)_{nw;0v'} \times \hat{f}(\Omega - \omega_{nw;0v}) \hat{f}(\omega_{nw;0v'} - \Omega)(\rho_{0v;0v} + \rho_{0v';0v'}) \quad (73)$$

$$\Delta\rho^{res}_{nv;nv'} = \frac{2\pi}{\hbar^2} \sum_w \rho_{0w;0w} V(-\Omega)_{nv;0w} V(\Omega)_{0w;nv'} \times \hat{f}(\omega_{nw;0v} - \Omega) \hat{f}(\Omega - \omega_{nv';0w}) \quad (74)$$

where $\hat{f}$ is the Fourier transform of the pulse shape function f and only the resonant terms have been reatained.

For the simplest case, we assume that $V_{n0;00}$ and $V_{n1;00}$ are the only nonzero matrix elements of the interaction and that $\omega_{nv;00} = \omega_e$ for all v. The expectation values of the displacement operator, calculated as in section III.A, are found to be[4]

$$Q_{ground}(t) \propto \left(\frac{2\hbar}{\omega_{grnd,vib}}\right)^{1/2} \cos \omega_{grnd,vib} t \quad (75)$$

$$Q_{excited}(t) \propto \left(\frac{2\hbar}{\omega_{exc,vib}}\right)^{1/2} \cos \omega_{exc,vib} t \quad (76)$$

The result for the excited state is easily understood. Essentially, impulsive absorption leaves the excited species on the side of its excited-state potential energy surface. Following excitation, motion toward and oscillation about the excited-state potential energy minimum ensues. The result eq 75 for the ground state is correct to the extent that wavepacket propagation during the excitation event, and not the coordinate dependence of the transition moment, provides the dominant contribution to $Q_{ground}(t)$.

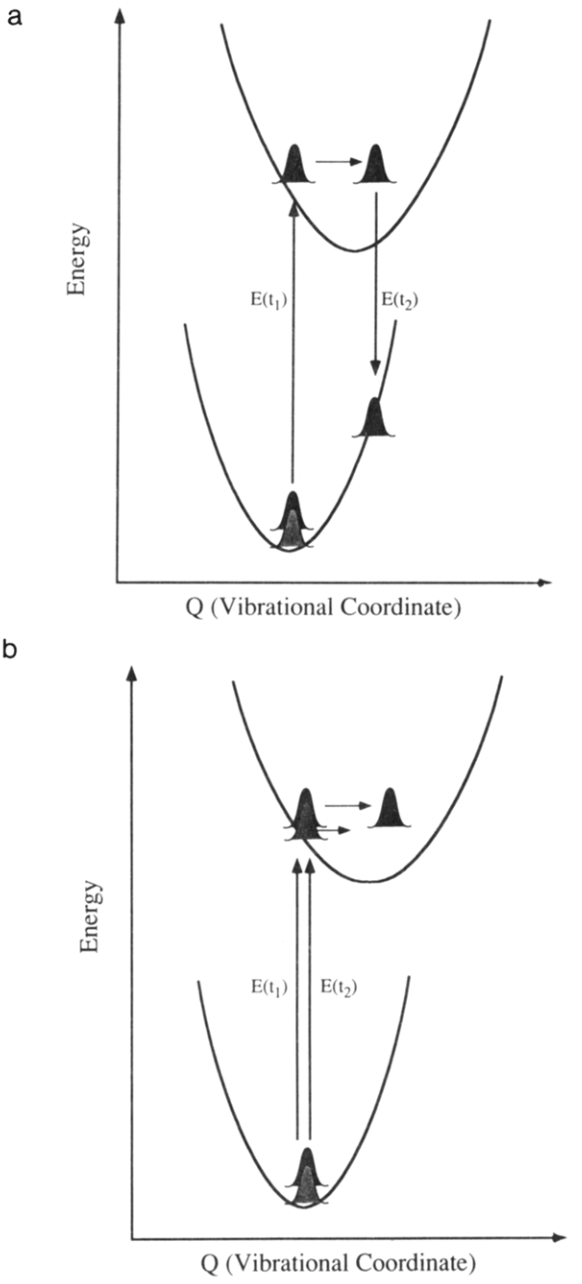

Figure 8. The coherences created through excited-state wavepacket propagation are shown. Part a shows the ground-state vibrational coherence results from the overlap between a ground-state ket wavepacket (black) that is transferred to the excited state surface at time t_2, propagated on the excited state, and then transferred back to the ground state at t_1, and a stationary ground-state bra wavepacket (gray). Part b shows the excited-state vibrational coherence results from the overlap between a ground-state ket wavepacket that is transferred to the excited state at time t_2 and then propagated on the excited-state surface and a ground-state bra wavepacket that is transferred to the excited state at time t_1.

C. Electronic Dephasing

In the above density matrix treatment, the effects of electronic dephasing were ignored since the majority of experiments have concentrated on vibrational co-

herences. Dephasing processes are included by adding a relaxation term to the time evolution of $\rho(t)$ as follows:

$$i\hbar\dot{\rho}(t) = [H,\rho] + \frac{\mathrm{d}}{\mathrm{d}t}\rho_{\mathrm{relax}} \tag{77}$$

The resonant solution for $\rho(t)$ to second order now becomes[4,46]

$$\rho^{\mathrm{res}}_{0v;0v'}(t) = -\frac{1}{\hbar^2}\int_{-\infty}^{\infty} \mathrm{d}t'\, f^2(t-t')\sum_w V_{0v;nw}(\Omega)\, V_{nw;0v'}(-\Omega)\times$$
$$\left\{\frac{\rho_{0v;0v}\exp\left[-\left(i\omega_{\mathrm{grnd}}+\frac{1}{T_2^{\mathrm{grnd}}}\right)\left(t'-\frac{T_e}{2}\right)\right]}{i(\omega_0-\omega_{n0})+\frac{1}{T_e}} + \right.$$
$$\left.\frac{\rho_{0v';0v'}\exp\left[-\left(i\omega_{\mathrm{grnd}}+\frac{1}{T_2^{\mathrm{grnd}}}\right)\left(t'-\frac{T_e}{2}\right)\right]}{-i(\omega_0-\omega_{n0})+\frac{1}{T_e}}\right\} \tag{78}$$

$$\rho^{\mathrm{res}}_{nv;nv'}(t) =$$
$$-\frac{1}{\hbar^2}\int_{-\infty}^{\infty} \mathrm{d}t'\, f^2(t-t')\sum_w V_{nv;0w}(\Omega)\, V_{0w;nv'}(-\Omega)\times$$
$$\rho_{0w;0w}\left\{\frac{\exp\left[-\left(i\omega_{\mathrm{exc}}+\frac{1}{T_2^{\mathrm{exc}}}\right)\left(t'-\frac{T_e}{2}\right)\right]}{i(\omega_0-\omega_{n0})+\frac{1}{T_e}} + \right.$$
$$\left.\frac{\exp\left[-\left(i\omega_{\mathrm{exc}}+\frac{1}{T_2^{\mathrm{exc}}}\right)\left(t'-\frac{T_e}{2}\right)\right]}{-i(\omega_0-\omega_{n0})+\frac{1}{T_e}}\right\} \tag{79}$$

where the T_2's are the vibrational dephasing times and T_e is the electronic dephasing time. Electronic dephasing does not affect the vibrational dynamics in nonresonant ISRS but adds a small time delay for the vibrational excitation in resonant ISRS.[4]

Later sections describe recent experiments that have monitored and manipulated electronic coherences.

D. Comparison to Frequency-Domain Spectroscopy

We mention very briefly some issues concerning comparison between the information content of data obtained through impulsive time-resolved vibrational spectroscopy and various frequency-domain experiments, and their relative practical advantages. First, it has been shown that impulsive stimulated scattering yields information equivalent to that provided from frequency-domain light scattering experiments.[1,2] In general, the time-domain approach offers important advantages in characterization of low-frequency modes which are difficult to resolve through conventional methods, and in examination of very heavily damped modes which appear in the spontaneous light-scattering spectrum as broad, structureless features centered at zero frequency shift. Other frequency-domain methods, in particular stimulated Raman and Brillouin gain spectroscopies, offer better prospects for elucidation of low-frequency and heavily damped modes. These methods are just beginning to be exploited for this purpose.

In the resonant case, there is no equivalence in principle to a simple frequency-domain experiment. To a certain extent, absorption and resonance Raman scattering spectroscopies provide information about wavepacket dynamics in electronic excited states which is similar to that extracted from impulsive absorption measurements. For example, one might observe vibrational progressions in absorption spectra whose frequencies give the excited-state molecular vibrational frequencies which are observed in time-domain impulsive absorption experiments. Similarly, resonance Raman measurements can indicate the nature of the excited-state PES, at least in the region of the ground-state equilibrium geometry. However, absorption and resonance Raman spectra only provide information about excited-state wavepacket propagation which occurs while electronic phase coherence is maintained. In contrast, impulsive absorption measurements continue to provide information for as long as vibration phase-coherence is maintained—generally a much longer period of time, especially in condensed phases—and so the impulsive absorption measurements often yield information about a much larger region of the excited-state PES.

IV. Examples of Impulsive Time-Resolved Vibrational Spectroscopy

In this section we present a review of experiments which illustrate the mechanisms of impulsive vibrational excitation and spectroscopy and which show some of the kinds of information which can be obtained using the methods. Although many of the initial experiments were aimed primarily at demonstrating spectroscopic capabilities, the potential for extracting important dynamical information was quickly realized. Experiments in which motions associated with chemical reactions, structural phase transitions, and other rearrangements soon began to yield new fundamental insights into those phenomena, and complex materials including biological systems were found to exhibit intriguing oscillatory responses, suggesting possible functional roles of vibrational coherence. The most recent developments in the field have been directed toward achieving optical control over chemical reactions and collective material behavior. The advances here hold the exciting promise of allowing active control over electronic and nuclear coherences analogous in some respects to the routine manipulation of spin coherences in multiple-pulse nuclear magnetic resonance.

A. Nonresonant Impulsive Stimulated Scattering

1. Early Origins

a. Impulsive Stimulated Brillouin Scattering. The very first "impulsive" stimulated scattering ex-

periments to our knowledge were conducted in the late 1960s[60] involving acoustic phonons. It was discovered that tightly focused, intense Q-switched laser pulses (of nanoseconds duration) could damage many materials, even if the light was not absorbed significantly. The damage was correctly attributed to shock waves which radiate cylindrically from the excitation region. These acoustic waves are generated through stimulated Brillouin scattering involving mixing among the frequency and wavevector components contained within the focused excitation spot.

The first examples of time-resolved vibrational spectroscopy in the impulsive limit involved acoustic phonons with picosecond and nanosecond oscillation periods. In impulsive stimulated Brillouin scattering (ISBS),[1,2] crossed picosecond laser pulses are used to generate counterpropagating acoustic waves which are detected through time-resolved diffraction. The acoustic frequency ω is determined by the scattering wavevector q and the speed of sound v, i.e. $\omega/q = v$. The frequency can be tuned by simply adjusting the wavevector.

The great strength of ISBS has been in characterization of the acoustic properties of crystalline solids near structural phase transitions and of glass-forming liquids as the temperature or pressure is varied and the liquid–glass transition is approached.[52-59] A typical example is the study of the structural phase transition of the ferroelectric material rubidium diphosphate.[55] Data at a series of temperatures approaching phase-transition temperature are shown in Figure 9. In this case VH-polarized excitation pulses have been used to generate a shear acoustic wave, and V-polarized probe light is diffracted to yield H-polarized signal. The transverse acoustic phonon frequency declines precipitously as the phase transition is approached because the incipient phase is distorted along the shear acoustic coordinate. The shear acoustic mode acts as a kind of collective "reaction coordinate" along which ions in the crystal move from their positions in one phase into the positions they occupy in the new phase. The restoring force against this motion (and therefore the acoustic frequency) decreases as the transition temperature is approached.

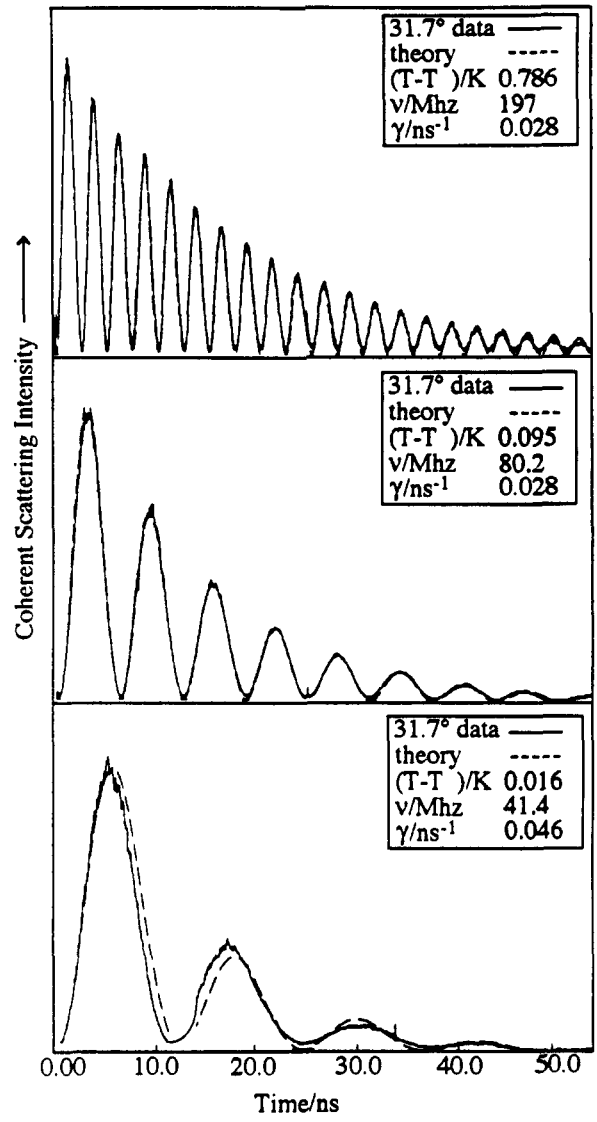

Figure 9. ISBS data from the "soft" transverse acoustic mode in the ferroelectric crystal rubidium dihydrogen phosphate as the phase-transition temperature is approached from above. The data were obtained using a VHVH excitation and probing geometry. The dashed lines are damped-oscillator simulations used to fit the data. The acoustic frequency decreases as the transition temperature is approached, indicating the reduced resistance to shear (i.e. the "softening") of the crystal.

b. Impulsive Stimulated Rotational Raman Scattering. Another important early experiment involved no vibrations at all, but instead demonstrated the capability for impulsive initiation of molecular rotational motion which could then be probed in the time domain. It was predicted and then demonstrated[61] that the sudden torque exerted by a picosecond pulse on molecules in the gas phase would initiate coherent rotational motion and that recurrences in alignment (and in the time-dependent birefringence) could be observed which would reflect the initial population of rotational levels. The excitation mechanism through which torque is applied is impulsive stimulated rotational Raman scattering, essentially the optical Kerr effect taken to the impulsive limit.

Analogous optical Kerr effect experiments in liquids also involved a torque on molecules applied optically through mixing among the frequency components of an excitation pulse. This is sometimes described explicitly as "stimulated Rayleigh-wing" scattering. Usually this is not thought of as "impulsive", since there is no well-defined rotational period in the liquid state with respect to which the pulse might be short. Instead rotational motion is described as relaxational (i.e. noninertial, or diffusional) in character. In fact the pulse might be quite long in duration, and the degree of molecular alignment generally increases gradually (without any phase coherence in the molecular motion) toward some limiting value as long as irradiation continues. However, on sufficiently short time scales molecular rotation can be seen to have vibrational (i.e. librational) character in many liquids.[62-69] In this case it is meaningful to think of an impulse force whose duration is short compared to the librational period. Impulsive stimulated scattering experiments on liquids conducted with femtosecond time resolution will be discussed below.

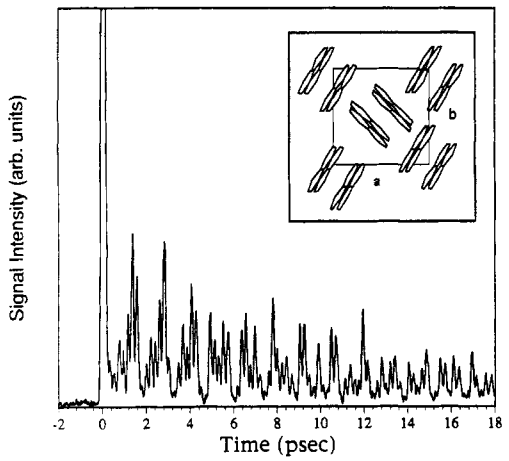

Figure 10. ISRS data from α-perylene at 5 K with a transient grating experimental geometry. The complex beating pattern results from simultaneous excitation of the 33-, 56-, 80-, and 104-cm^{-1} optic phonon modes.

2. Excitation of Lattice Vibrations: Initial Demonstrations

a. Impulsive Stimulated Raman Scattering. The "modern era" of impulsive vibrational spectroscopy began with the first impulsive stimulated Raman scattering experiments on vibrational modes. These showed that the femtosecond laser apparatus which at the time (1984–1985) was just becoming widely available could be used for impulsive excitation of many lattice vibrational mode and for time-resolved observations of vibrationally distorted materials. The experiments were conducted on organic crystals of α-perylene,[70] a crystal of some special interest in connection with an excited-state excimer formation reaction. Data from the crystal (recorded more recently) are shown in Figure 10. The time-dependent oscillations and decay are due to several low-frequency Raman-active optic phonon modes which are excited impulsively. The lower-frequency modes occurring at 33, 56, and 80 cm^{-1} involve librations of the molecular pairs shown in the inset of Figure 10. The higher-frequency mode at 104 cm^{-1} involves vibrations of molecules within a pair against each other and is believed to represent motion along an excited-state reaction coordinate leading toward excimer formation. These experiments, which were essentially demonstrative in nature, suggested the possibilities for impulsive vibrational spectroscopy of modes involves in chemical or structural rearrangements.

b. Optical Rectification. At about the same time that ISRS was first demonstrated on α-perylene, femtosecond time-resolved experiments on the inorganic crystal lithium tantalate also showed oscillations due to lattice vibrations.[71] Typical data are shown in Figure 11. In this case a different excitation mechanism was discussed; based on the fact that $LiTaO_3$ is noncentrosymmetric and therefore $\chi^{(2)}$ processes such as sum or difference-frequency mixing can occur. Usually these processes involve mixing of discrete incident frequencies. However, for a short incident pulse difference-frequency generation, like ISS, may occur through mixing among the continuous range of incident frequency components.[7] This generates far-IR radiation which may extend from nearly zero frequency to the bandwidth of the pulse. The result

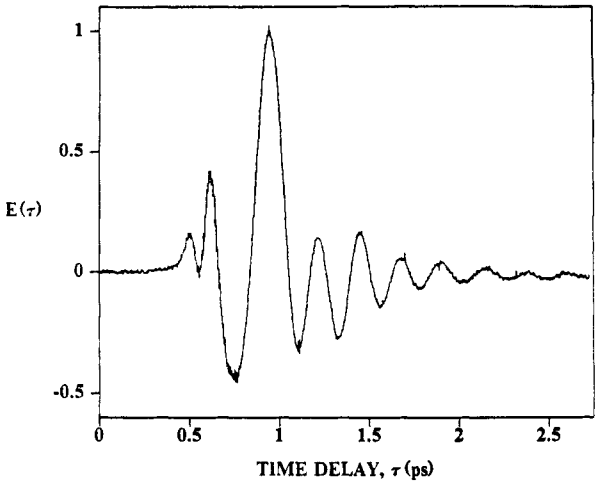

Figure 11. The femtosecond infrared waveform generated through the focusing of a single pump pulse to a 7-μm spot and detection of time-dependent birefringence by a probe pulse which travels parallel to the excitation pulse but is spatially separated from it. The damped oscillations are due to impulsive excitation of a phonon–polariton mode at 200 cm^{-1}. This mode propagates perpendicular in space to the probing region. (Reprinted from ref 71. Copyright 1984 American Physical Society.)

is an ultrashort "burst" of far-IR radiation whose duration is about a half-cycle of an average frequency which may be several terahertz. In a noncentrosymmetric crystal, the lattice vibrations are polar and are both Raman and IR active. Thus a mode which is within the bandwidth of the excitation pulse is driven resonantly by the far-IR radiation. The driving force is more or less "impulsive" since the duration of this radiation is less than one vibrational cycle.

Since the phonon modes are also Raman active, ISRS also contributes to the excitation. Subsequent calculations[74] indicate that in fact ISRS may play a larger role than resonant far-IR excitation in the case of $LiTaO_3$. The main point though is that an alternative "impulsive" excitation mechanism exists which is applicable to IR-active vibrational modes in noncentrosymmetric media. In general, a burst of terahertz radiation could also be generated outside the crystal of interest and directed into it for excitation of polar phonons even in centrosymmetric media.

3. ISRS Studies of Lattice Dynamics

ISRS experiments have now been reported on a substantial number of organic and inorganic crystals, and several of the experiments have gone far beyond the "demonstration" phase to provide important new information. An illustrative example is presented in this section. We review briefly the results of two ISRS studies of a ferroelectric material in the perovskite crystal family.[72,73a,74] In the first study, the ISRS technique was used to elucidate the dynamics of a class of structural phase transitions which occur in potassium niobate and barium titanate as well as other perovskites. In the second, ISRS measurements yielded strong evidence for significant phonon–phonon interactions in lithium tantalate, a material used for a variety of nonlinear optical applications.

a. Soft Lattice Modes in $KNbO_3$ and $BaTiO_3$. ISRS experiments conducted on the ferroelectric materials potassium niobate and barium titanate centered

upon the "soft" optic phonon modes involved in a series of structural phase transitions.[72,73a] The low frequencies and strong damping rates typical of soft modes in crystals near structural phase transitions make them extremely difficult to characterize through conventional Raman scattering. The Stokes and anti-Stokes features become very broad and merge at zero frequency shift, giving rise to a central scattering feature which typically overlaps other contributions due to hopping or other purely relaxational motions. It is often impossible to determine uniquely how many modes are present and whether they are relaxational or vibrational in character. In both $KNbO_3$ and $BaTiO_3$, it was widely believed that the soft mode features in the Raman spectra masked additional, low-frequency relaxational modes of the same scattering symmetry. This belief was motivated primarily by discrepancies between the values of the low-frequency dielectric constants calculated (through the Lyddane–Sachs–Teller relation) from the measured polar phonon frequencies and those determined independently through capacitance measurements. The belief was that additional relaxational modes, if observable, would yield agreement with the dielectric constants.

The crystal structures of potassium niobate and barium titanate are shown in Figure 12. In each case, the central ion (Nb or Ti) is surrounded by six oxygen ions at the face centers of the unit cell and by eight counterions (K or Ba) at the unit cell corners. The crystals undergo a series of structural phase transitions between a high-temperature cubic phase which is paraelectric and three low-temperature ferroelectric phases. Many features of the cubic–tetragonal–orthorhombic–rhombahedral series of transitions have been described according to an order–disorder model which proposes that the potential energy of the central ion reaches a local maximum at the center of the unit cell and that there are eight local potential energy minima for the central ion located at positions between the unit cell center and the corners. According to the model, all eight sites have equal energies in the cubic (paraelectric) phase, four sites on one side of the unit cell are lower in energy ("allowed") than the other four in the tetragonal phase, two adjacent sites are allowed in the orthorhombic phase, and only one site is allowed in the rhombohedral phase. The direction of the polarization in each of the three ferroelectric phases is consistent with this model.

The order–disorder model implies that motion of the central ion among the different local potential energy minima occurs through thermally assisted hopping rather than vibration. However, Raman spectra of $KNbO_3$ and $BaTiO_3$ each clearly show a low-frequency, heavily damped "soft" optic phonon mode which presumably represents the motion involved in transition between phases. In general, soft modes play the role of collective "reaction coordinates" in displacive structural phase transitions, which are characterized not by several distinct potential energy minima (as in order–disorder transitions) but by one minimum whose position is displaced at temperatures below the transition temperature. It is along the soft mode coordinate that ions move from their positions in one phase into the positions they occupy in an incipient phase. Motion about the single potential energy minimum is vibrational in character. The frequency is typically low, especially near the phase-transition temperature T_c at which the crystal may exhibit only a weak restoring force (i.e. become "soft") with respect to motion toward the new structure. The damping rates of soft modes are almost always very high, again especially near T_c since anharmonic coupling to other lattice degrees of freedom becomes very strong.

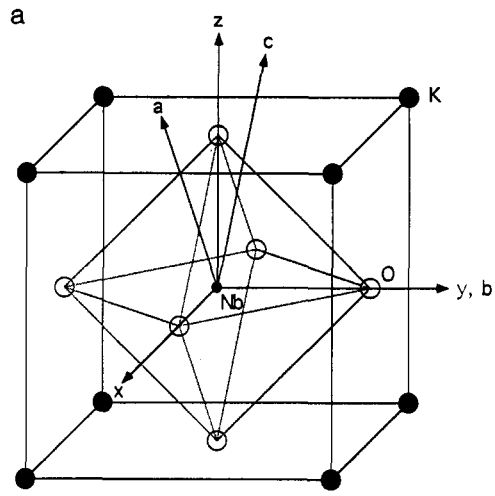

Unit Cell of $KNbO_3$ in the cubic phase
(x, y, z) crystal axes in C and T phases
(a, b, c) crystal axes in O phase

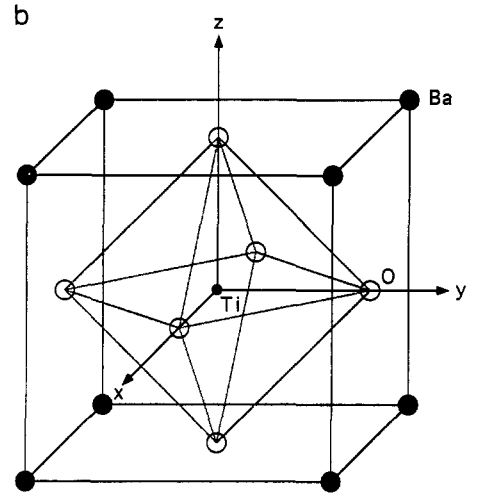

Unit Cell of $BaTiO_3$ in the cubic phase
(x, y, z) crystal axes in C and T phases

Figure 12. Part a shows the unit cell of $KNbO_3$ in the high temperature cubic phase. The crystal axes in the cubic and tetragonal phases correspond to the (x,y,z) coordinate system. The crystal axes in the orthorhombic phase correspond to the (a,b,c) coordinate system. Part b shows the unit cell of $BaTiO_3$ in the high-temperature cubic phase. The crystal axes in the cubic and tetragonal phases correspond to the (x,y,z) coordinate system. In the tetragonal phase, the z axis is the ferroelectric axis (from ref 73).

A soft lattice vibrational mode in $KNbO_3$ and $BaTiO_3$ would appear to rule out the eight-site model or any other order–disorder model in which the motion leading to structural change is hopping among distinct potential energy minima rather than vibration about a single minimum. To accomodate the soft mode observations, a modified eight-site model was proposed in which there

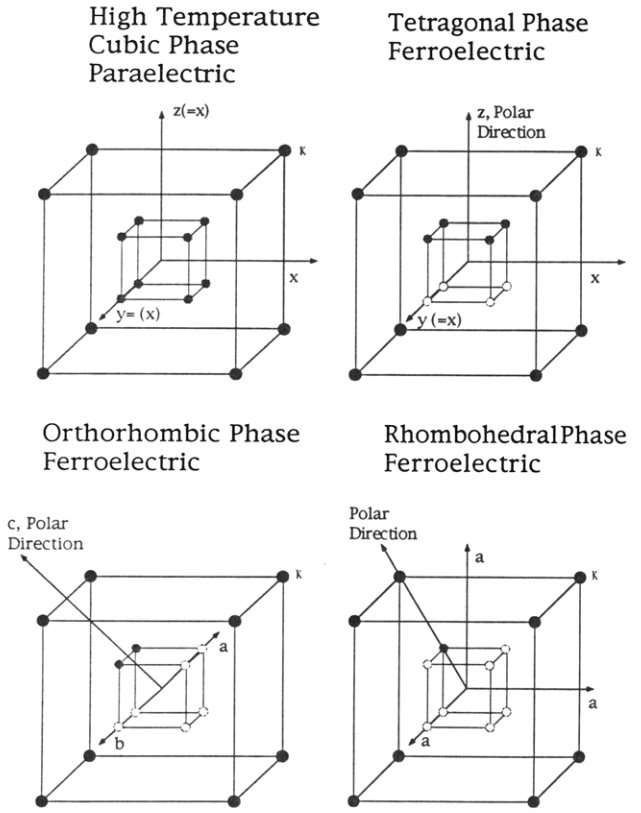

Figure 13. The central ion occupation sites within the framework of the eight-site model for the structural phase transitions in $KNbO_3$ and $BaTiO_3$. The cross-hatched circles represent the most favored sites for the central ion and the empty circles represent the higher energy sites. The eight sites are displaced along the ⟨111⟩ axes, toward the corners of the unit cell (from ref 73).

are still eight potential energy minima, but the barriers between the degenerate "allowed" sites of lowest energy are assumed to be so low (even compared to the zero-point vibrational energy) that motion among those sites would be vibrational in character. Motion of the central ion between allowed and higher-energy sites should still occur through thermally assisted hopping.

Representative ISRS data from $KNbO_3$ and $BaTiO_3$[72,73] are shown in Figures 14 and 15. The low frequencies and extremely high dephasing rates of the soft modes should be noted. Despite these features, the ISRS data permit accurate quantitative determination of the phonon frequencies. They also make it clear that there is only one mode present in each case. In particular, there are no relaxational modes in addition to the heavily damped vibrations. This supports the modified eight-site model. In $KNbO_3$, the values of soft phonon frequencies determined through ISRS measurements yielded quantitative agreement with the low-frequency dielectric constant at temperatures throughout the orthorhombic phase. In $BaTiO_3$, this quantitative agreement was not achieved with the dielectric constant values reported prior to the time of the ISRS work. However, more recent capacitive measurements of the low-frequency dielectric constant of $BaTiO_3$[73b] yield excellent quantitative agreement with the values calculated from phonon frequencies determined through ISRS. It seems that a consistent qualitative and quantitative picture of this important class of phase transitions can now be offered.

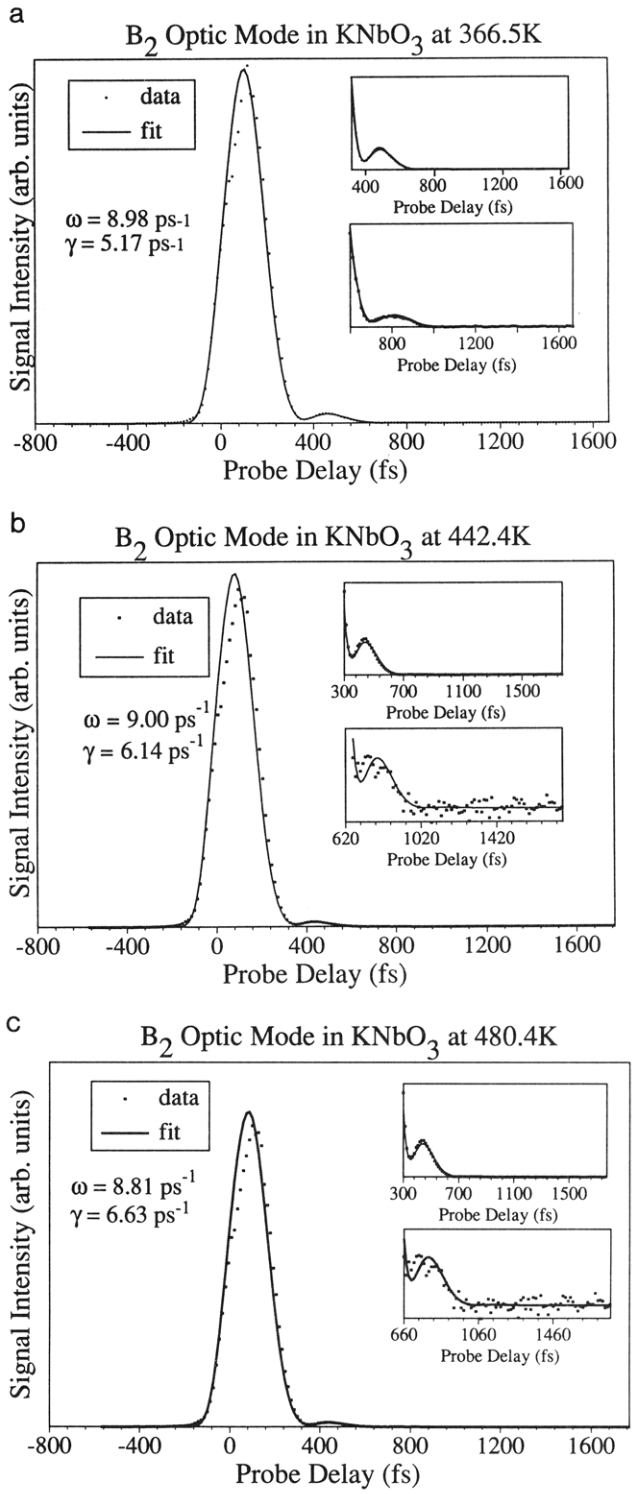

Figure 14. B_2-symmetry ISRS data from $KNbO_3$ showing the dynamics of the soft mode. The nuclear responses in parts **a–c** are fit with single damped harmonic oscillator responses. The wavevector is 2.7×10^{-4} cm^{-1} and the temperatures are indicated in the figures. The data show that there is only one mode present (from ref 73).

b. Lattice Dynamics and Mode Coupling in $LiTaO_3$. Lithium tantalate and many other members of its crystal family have useful electrooptic and other nonlinear responses based on lattice displacements induced by an applied field. A clear understanding of the lattice dynamics is essential for rationalization of these properties. However, study of $LiTaO_3$ had led to conflicting results and assignments for the spectrum of

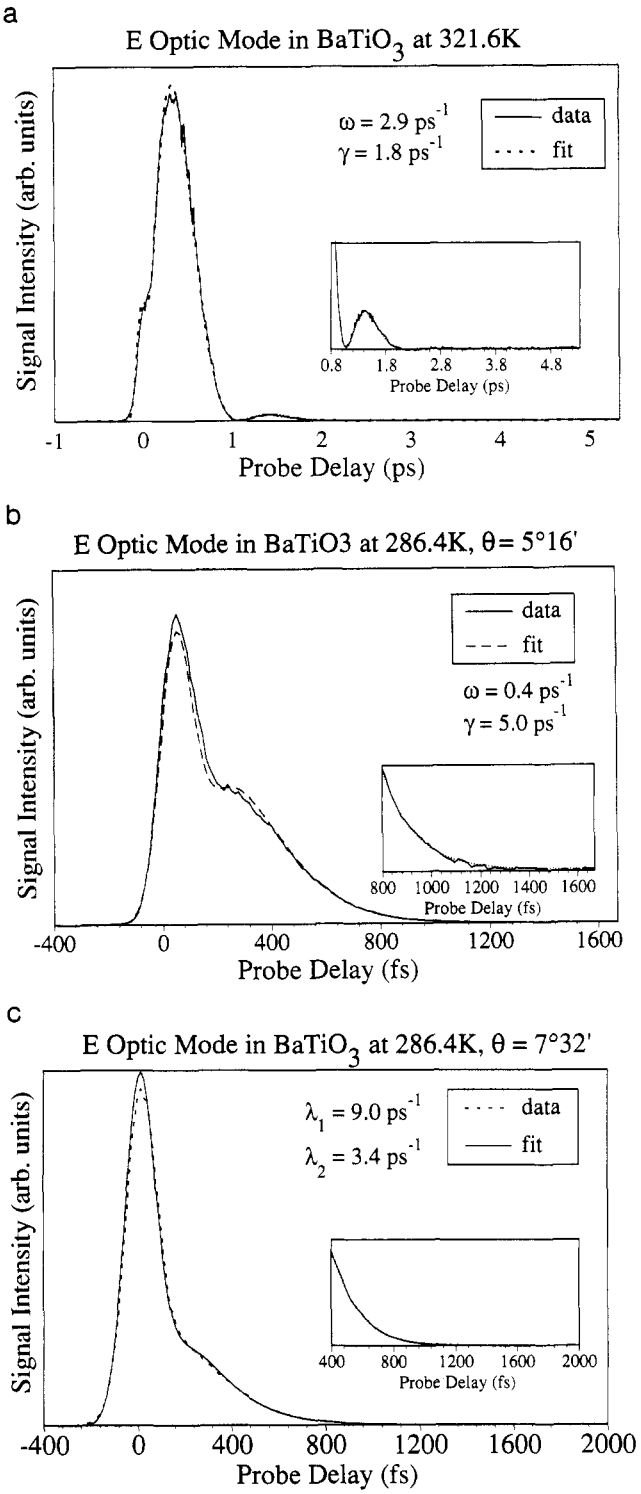

Figure 15. E symmetry ISRS data from $BaTiO_3$ showing the dispersive properties of the soft mode. In **a** and **b**, the data are fit with a single underdamped harmonic oscillator response while in **c** the data are fit with a single overdamped harmonic oscillator response (from ref 73).

low-frequency polar phonons which play the dominant roles in mediating behavior of practical interest.[74] Part of the complexity is due to the fact that the polar modes act as radiating dipoles which couple strongly to far-IR electromagnetic modes in the same wavevector and frequency range.[75] This results in coupled phonon–polariton modes whose frequencies and damping rates are highly dispersive (wavevector-dependent). The lattice is also highly anharmonic, with phonon–phonon

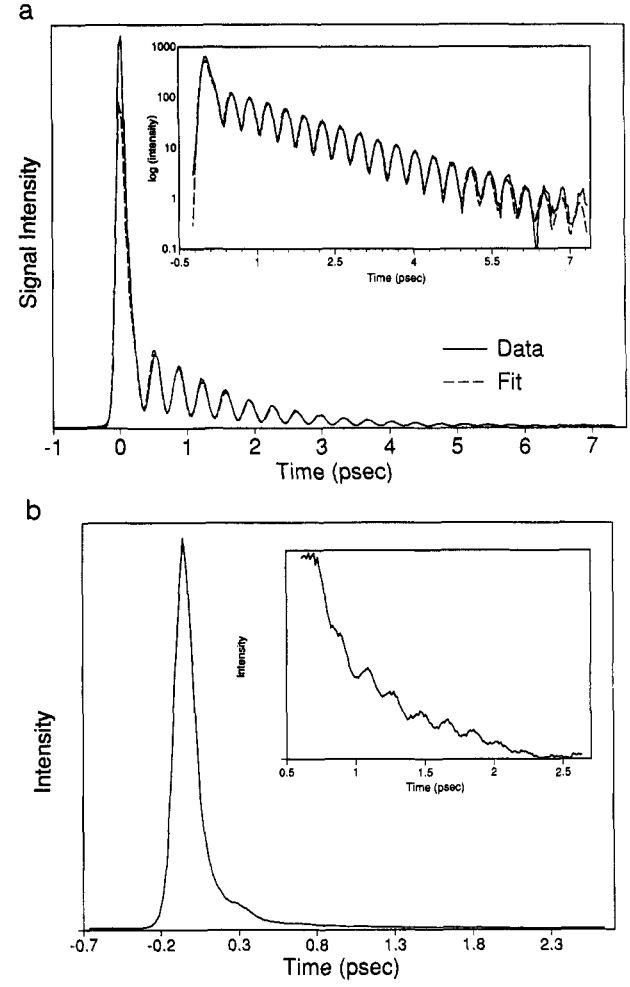

Figure 16. Part a shows the ISRS data from $LiTaO_3$ at 300 K, recorded in a transient grating geometry with a scattering wavevector of 1800 cm^{-1}. The signal arises from impulsive excitation of the lowest frequency A_1 phonon–polariton mode. The frequency and damping rate of the polariton are found to be 47.5 and 2 cm^{-1} respectively. Part b shows ISRS data at a wavevector of 12 800 cm^{-1}. The oscillations are far higher in frequency but are still resolvable due to heterodyning of the oscillatory signal with the decaying signal of a weakly Raman-active relaxational mode. The damping rate is found to be significantly higher than in the low-wavevector regime (from ref 74).

interactions exerting a strong influence over the lattice dynamics.

ISRS measurements were made over a wide range of wavevector values q to characterize the dispersive phonon–polariton behavior. Figure 16 shows data recorded at two different scattering angles, and the measured q-dependent frequencies and damping rates are shown in Figure 17. There are large discrepencies from the damping rate predicted on the basis of a simple phonon–polariton model, i.e. dispersion due to coupling of the phonon mode to only the electromagnetic field. Large differences in the damping rate are observed in three regions: there are two peaks at intermediate values of q, and there is anomalously strong damping at all of the lowest wavevectors examined. These features are due to coupling between the phonon–polariton mode and other lattice degrees of freedom, in particular to phonon modes of other symmetries at 92 and 140 cm^{-1} and to a relaxational mode with a decay time of approximately 0.3 ps. It is believed that coupling to modes of other symmetries is induced by strain in

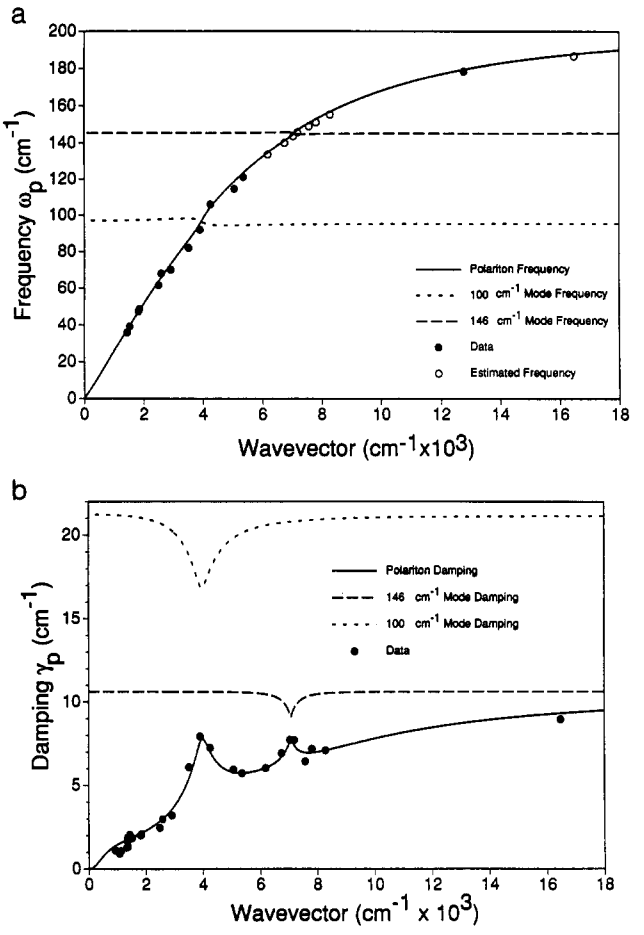

Figure 17. The experimental dispersion curves for the frequency (a) and damping (b) rate of the A_1 polariton in $LiTaO_3$. The experimental results are well reproduced by a model (solid curve) that includes coupling of the polariton to a weakly Raman-active relaxational mode (accounting for the strong damping seen at low wavevectors) and two oscillatory modes at 92 and 142 cm^{-1} (accounting for the two peaks seen in the damping dispersion at the wavevectors 3900 and 7000 cm^{-1}) (from ref 74).

the crystal and that the relaxational mode corresponds to a hopping motion of the central ion similar to those discussed in the previous section. Additional ISRS experiments on this sample at reduced temperatures required multiple-pulse excitation, and are discussed below.

4. ISRS from Liquids

a. Intramolecular Vibrations. For most chemists, the most graphic illustration of impulsive stimulated Raman spectroscopy was provided by direct time-resolved observation of molecular vibrations. Figure 18a shows data from dibromomethane liquid, collected in a transient grating configuration, in which the 173 cm^{-1} halogen bending mode is observed. Figure 18b shows data collected from the same mode with a single excitation pulse and a nearly collinear probe pulse whose transmitted spectrum is analyzed as a function of delay time. As discussed earlier, the transmitted probe pulse spectrum alternately red- and blue-shifts as the probe pulse arrives at the sample alternately in phase and out of phase with the coherent vibrational motion induced by the excitation pulse. ISRS data from molecular vibrations in many liquids have now been recorded in a variety of ways including optical Kerr effect geometries.[66,76]

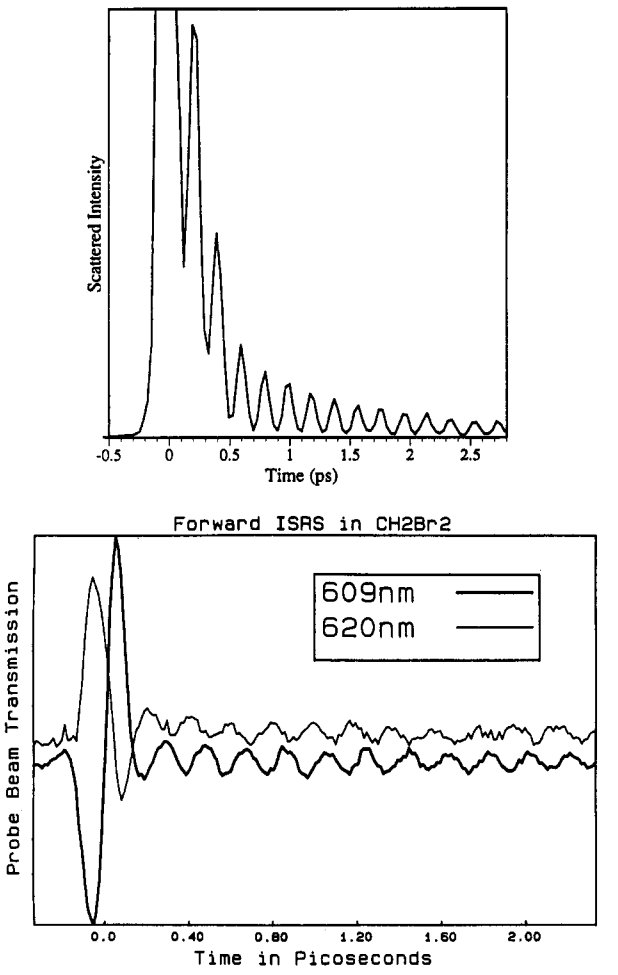

Figure 18. ISRS data from molecular vibrations in dibromomethane liquid at room temperature. Part a shows the transient grating configuration with the pump, probe, and signal beams polarized vertically. The oscillations in the data correspond to the 173-cm^{-1} halogen bending mode of CH_2Br_2. The decay of the oscillations is due to reorientational and vibrational dephasing. Part b shows the observations of molecular vibrations through measurement of the transmitted probe pulse spectral components as shown in Figure 2b, part 2. The probe pulse is centered at 615 nm. Antiphased oscillations of the red and blue components are observed due to the spectrum alternately shifting toward the red and the blue. (Reprinted from ref 66. Copyright 1987 Editions de Physique.)

In most cases, nonresonant ISRS data from molecular vibrations have not yielded new information about the modes since conventional Raman spectra can also provide their frequencies and dephasing rates. A recent exception is the ISRS data shown in Figure 19, collected from the glass-forming organic liquid triphenylphosphite (TPP).[59] The data show a low-frequency and very heavily damped vibrational feature which may be due to either the "umbrella" mode of vibrational about the central P atom or to torsional motions of the phenyl groups. The Raman spectrum of TPP is shown in the inset. There is no apparent spectral feature at 75 cm^{-1}, presumably because it is masked by the intense quasielastic peak. The strong damping indicates rapid energy exchange between the molecular vibrational mode and intermolecular motions. This exchange could provide one of the dissipative channels which lead to slow structural relaxation and viscoelastic behavior.

b. Intermolecular Vibrations. As mentioned earlier in connection with the optical Kerr effect, to the

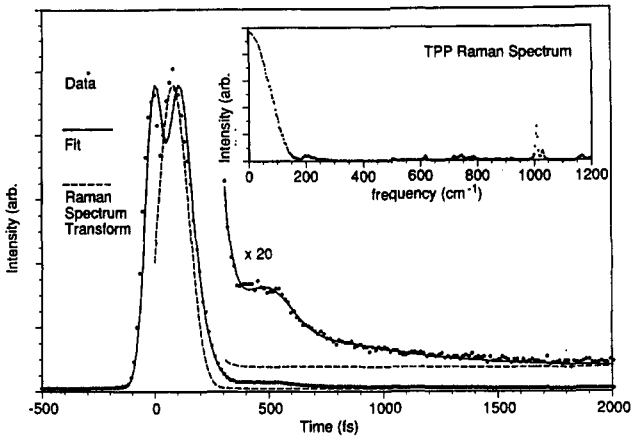

Figure 19. ISRS data from the glass-forming liquid triphenyl phosphite. The polarizations of the excitation, probe, and signal beams are chosen to minimize the electronic contribution to the signal at $t = 0$. Following this contribution, heavily damped oscillations are observed. The damped oscillatory mode is found to have a frequency and damping rate of respectively 76 and 33 cm^{-1}. The Raman spectrum of TPP is shown in the inset. The transform of the Raman data into the time domain, shown by the dotted line, gives no indication of the vibrational mode and demonstrates the difficulty of detecting low-frequency vibrations in the presence of a broad Rayleigh wing. (Reprinted from ref 59. Copyright 1992 American Institute Physics.)

extent that molecular motions in liquids are purely relaxational (i.e. diffusional) in character, there is no meaningful definition of an "impulsive" driving force. Time-resolved optical Kerr effect measurements of molecular rotational diffusion dynamics require pulse durations short compared to the rotational relaxation time, but not compared to any vibrational period. However for many liquids, motion which is clearly nondiffusional can be observed on short time scales. An example is presented in Figure 20, which shows ISS data recorded from carbon disulfide liquid at different pressures.[77] Even at 1 atm, the signal continues to increase after the excitation pulses have left the sample (at $t > 100$ fs), indicating an inertial (nondiffusional) response to the sudden driving force. Only after some additional time does the signal begin to decline, indicating a return toward equilibrium. At elevated pressures the data show inertial behavior more dramatically, as heavily damped time-dependent oscillations become apparent. The data were analyzed in terms of the impulsive torque exerted by the excitation pulses, which initiates molecular rotational motion. This motion is opposed by neighbors in the liquid, leading to oscillation about a local potential energy minimum. Measurement of the librational frequency yields information about the configuration-averaged intermolecular forces (torques) in the liquid. The rapid decay of oscillations was analyzed in terms of primarily inhomogeneous dephasing, and so the decay rate yielded information about the degree of inhomogeneity (i.e. the range of intermolecular torques) in the liquid.

In this simplest level of analysis, the excitation pulses act on the molecules through their (single-molecule) polarizability anisotropies, the motion induced is librational, and the signal measures the degree of orientational alignment which can be described through the single-molecule orientational correlation function. ISS data similar to that shown in Figure 20 were

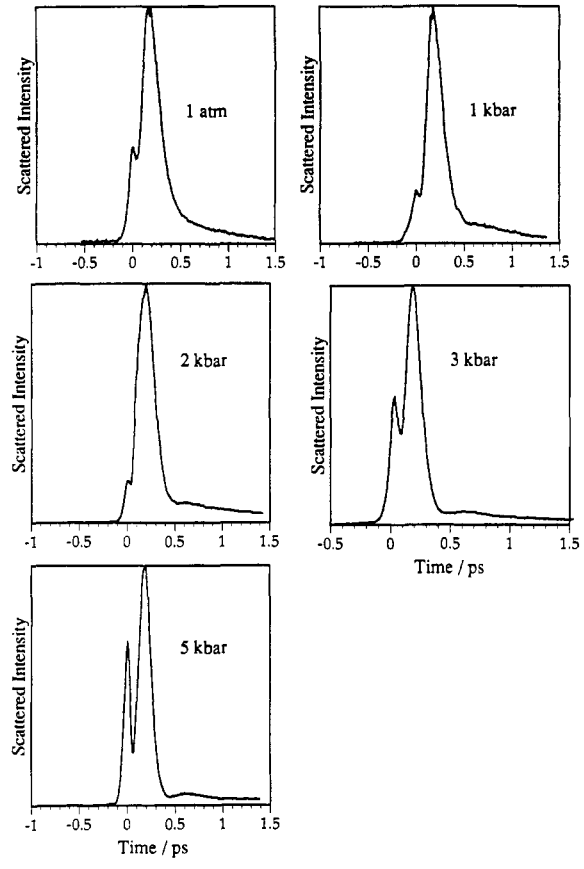

Figure 20. Pressure-dependent ISS data from liquid carbon disulfide. The signal is recorded using a polarization combination of excitation and probing beams that discriminates against electronic contributions and allows only the nuclear contributions to the signal to appear. As the pressure is increased, an oscillatory feature at 500 fs appears. The decay time of the part of the signal that persists after 500 fs increases with increasing pressure. Both features indicate more hindered reorientations of molecules as the liquid becomes more dense. (Reprinted from ref 77. Copyright 1992 American Chemical Society.)

recorded with various four-wave mixing polarization combinations and in optical Kerr effect configurations.[13,62-69] Unfortunately, molecular dynamics simulations of CS_2 and calculations of the single-molecule orientational correlation function do not yield good agreement with the data at elevated pressures or reduced temperatures.[77] The inertial "lag" at short times is described well, but the weakly oscillatory feature at longer times does not appear. There are several possible explanations of the discrepancies. First, the simulations could simply be wrong due to imperfect intermolecular potentials. Second, it is possible that pair orientational correlations in the liquid—which can still contribute to signal through single-molecule polarizability anisotropies—play an important role in the data. This could be plausible, for example, if one imagines that neighboring molecules with different orientations are subjected to a torque along the direction which bisects them, initiating rotational motions in opposite directions that lead to intermolecular "collisions" and subsequent librations. Such a picture clearly includes important pair orientational correlations, which can contribute to signal through the separate molecular polarizability anisotropies. Finally, a third possibility is that higher-order polarizabilities must be accounted for. For example, one might imagine the

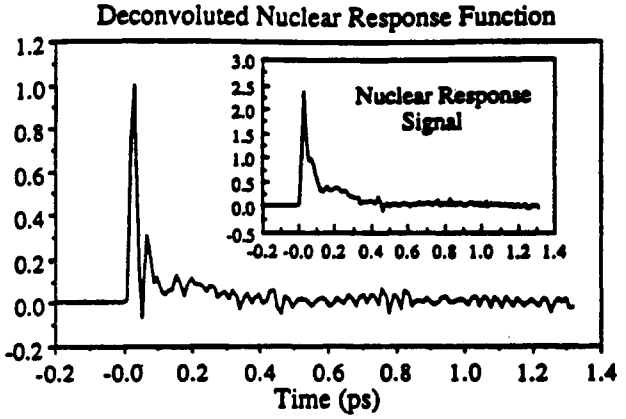

Figure 21. Optical Kerr effect measurements in water. The nuclear response obtained after deconvoluting the pump and probe pulse profiles shows a clear oscillation at 50 fs and a rapid decay. The oscillation is believed to arise from hindered rotations or librational motion of the water molecules. (Reprinted from ref 80. Copyright 1993 Springer-Verlag.)

impulse force driving two neighboring molecules toward each other along a "Raman-active" intermolecular coordinate. The light-scattering activity in this case arises from a pair polarizability and can initiate relative center-of-mass (i.e. translational) as well as orientational motions.

Unfortunately, reliable calculation of higher-order molecular orientational or translational correlation functions or higher-order polarizabilities is extremely difficult. It is therefore difficult to "assign" unambiguously the vibrational mode observed in Figure 20. A substantial amount of suggestive, but not conclusive, evidence in favor of a librational interpretation has been presented. Similar responses have been observed in benzene and other molecules. In addition, extensive studies of CS_2 solutions in various solvents have been done[78] and have yielded information about the degree of inhomogeneity in mixed as well as neat liquids.

A recent example of ISS data of this form recorded from pyrrole liquid[79] has been interpreted not in terms of molecular librations but rather in terms of intermolecular motions that may include a substantial translational component. The planar pyrrole molecules are believed to form "T"-shaped dimers in the liquid state, and the vibrational motion observed was interpreted in terms of distortions of the pair geometry. This interpretation involves pair molecular correlations which contribute to signal through pair polarizabilities.

A final recent example of optical Kerr effect data from intermolecular motions in liquids is shown in Figure 21.[80] In this experiment, measurements in water revealed a librational mode with a frequency of approximately 600 cm^{-1}. The Kerr signal was modeled by a spectral distribution of librations obtained through computer simulations. The oscillatory feature was reproduced as was the fast decay seen in the data. The decay is not due to an overdamped mode but simply to the wide frequency distribution (from 100–1100 cm^{-1}) of the oscillators about the mean frequency.

Impulsive stimulated scattering study of molecular liquids in this fashion continues to be an active research area. This subject was investigated extensively in earlier years through quasielastic light scattering spectroscopy. ISS has led to a resurgence of interest because the inertial and weakly oscillatory features apparent in ISS data could not be extracted uniquely from the light-scattering spectra. New and important components of molecular motion in the liquid state have been revealed, and they have provided more stringent tests of liquid-state theory and simulation. A convergence of experiment and simulation remains an important goal.

B. Resonant Absorption and Impulsive Stimulated Scattering

Time-resolved spectroscopy at the impulsive limit has been broadened in several ways through the use of resonant excitation pulses. First, resonance enhancement of coherent vibrational excitation in the electronic ground state has permitted ISRS observations in rather dilute systems such as proteins. Second, observation of coherent motion in electronic excited states has permitted their potential energy surfaces and photochemical processes to be studied in detail. "Femtochemistry" observations of unstable molecular species formed during transformation from reactant to product have permitted the reaction process and the interactions which influence it to be examined in exquisite detail in a variety of molecules and media. Finally, impulsive absorption into delocalized electronic excited states in some solids has provided a new mechanism for coherent vibrational excitation of modes which may not be accessible through ISRS.

1. Excited-State Molecular Vibrations in Liquids: Early Origins and Recent Results

The first resonant femtosecond experiments in which coherent vibrations were time-resolved were transient absorption measurements on dye molecules in liquid solution. Typical data from the dye malachite green are shown in Figure 22.[81] The oscillations and decay were described originally as "mysterious", but were explained soon afterward in terms of molecular vibrations of the electronically excited molecules.[83]

These vibrations are observed in impulsive absorption experiments even though conventional frequency-domain electronic absorption spectra of the molecules in solution show no vibrational progressions. Such progressions, observed often in the gas phase and less frequently in condensed phases, yield the vibrational frequencies of the excited state. In the liquid state, homogeneous and inhomogeneous broadening (i.e. dephasing) of the electronic transition wash out discrete vibrational structure in the electronic absorption spectra of many molecules, including the dye molecules studies here. However, information about excited-state vibrations can be extracted in the time domain. Excited-state vibrational motion is initiated in all the excited molecules at essentially the same time, regardless of variation in the excited-state electronic energy due to the inhomogeneity of the environment. The vibrations continue for as long as the excited-state vibrational dephasing rate or electronic lifetime, regardless of fast electronic dephasing. Thus there is no washing out of the coherent vibrational oscillations even though the corresponding progressions do not appear in the frequency domain. In many cases, resonance Raman spectra can provide more information than absorption spectra about the electronic potential energy

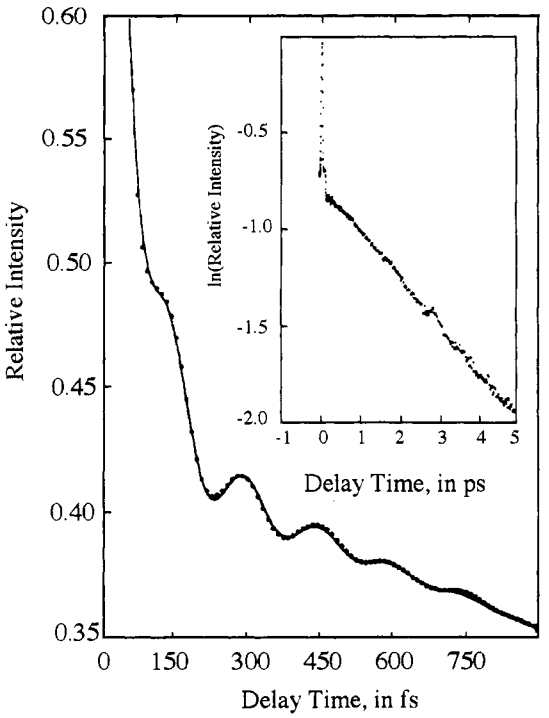

Figure 22. Impulsive absorption measurements of malachite green dye in methanol solution. Well-defined oscillations with a period of 150 fs are observed. These oscillations were later explained to result from coherent molecular vibrations in the excited state of malachite green. (Reprinted from ref 81. Copyright 1986 the American Physical Society.)

surface. However, as mentioned earlier these too are limited by rapid electronic dephasing rather than by (generally slower) vibrational dephasing.

Shortly after the initial set of observations, a systematic study of molecular vibrations in ground and excited electronic states was reported.[4] Following impulsive excitation of malachite green in solution with a resonant pulse, either transient birefringence or transient absorption was monitored to yield the results shown in Figure 23, parts a and b.[4] In the case of birefringence, the dominant contribution to signal was from those molecules which remained in the ground electronic state and which underwent coherent oscillations driven through ISRS. In the case of transient absorption, molecules in the excited state played the predominant role. In fact the probe wavelength was the same as the excitation wavelength, so oscillations in signal were due to time-dependent stimulated emission from the coherently vibrating excited state back to the ground state. Note also that the excited-state vibrational decay is faster, presumably because of stronger intermolecular interactions in the excited state. The ground and excited-state potentials of malachite green apparently have very similar curvatures, since the vibrational frequencies are observed to be equal.

Figure 24 shows more recent results from the dye nile blue in soluton.[82,83] The main feature of this data with respect to molecular vibrations is the high frequency of the modes observed. By using 10-fs excitation and probe pulses, molecular vibrations of energies up to 600 cm^{-1} were excited impulsively and monitored in the time domain. In this case, the electronic and vibrational evolution of the excited dye molecules was probed on 10–1000-fs time scales.

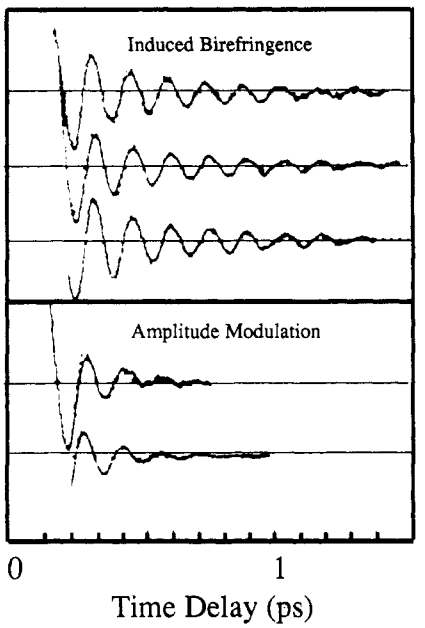

Figure 23. Pump–probe data from malachite green dye in different solvents. (a) Measurement of transient birefringence yields information on ground-state vibrational dynamics in water (top curve), ethylene glycol (middle curve), and dimethyl sulfoxide (lower curve). (b) Measurement of transient dichroism (i.e. transient absorption through crossed polarizers) in water (top curve) and ethylene glycol (lower curve) yields information on excited-state vibrational dynamics. Note the increased rate of vibrational dephasing in the electronic excited state. (Reprinted from ref 4. Copyright 1988 the American Physical Society.)

2. "Femtochemistry" and Molecular Vibrations in the Gas Phase

One of the great strengths of impulsive absorption spectroscopy lies in what has been labeled "femtochemistry". Following the observation and explanation of coherent vibrations in bound potential energy surfaces of molecular excited states, impulsive absorption into unstable potential energy surfaces and direct observation of synchronized molecular photodissociation was carried out. The initial "femtochemistry" experiments of this type were conducted in ICN in the gas phase.[84] Some of the first data reported are reproduced in Figure 25. By probing absorption at several wavelengths, the motion of the molecules along the dissociative potential surface was monitored. What is actually measured is the laser-induced fluorescence induced by the variably delayed probe pulses at different wavelengths.

Figure 26 shows transient laser-induced fluorescence measurements made on NaI in the gas phase following impulsive absorption.[85] In this case the excited state is not simply dissociative, but weakly bound due to crossing of levels corresponding to states of largely covalent or ionic character. The data show time-dependent oscillations whose decay is due to some fraction of the molecules crossing through the barrier and undergoing dissociation. Figure 26b shows data in which the probe pulse is tuned to observe the reaction products, rather than the bound excited state. A series of "steps" is observed, each of which corresponds to some of the bound molecules reaching the turning point and dissociating. The timing of the steps matches the timing of the excited-state oscillations.

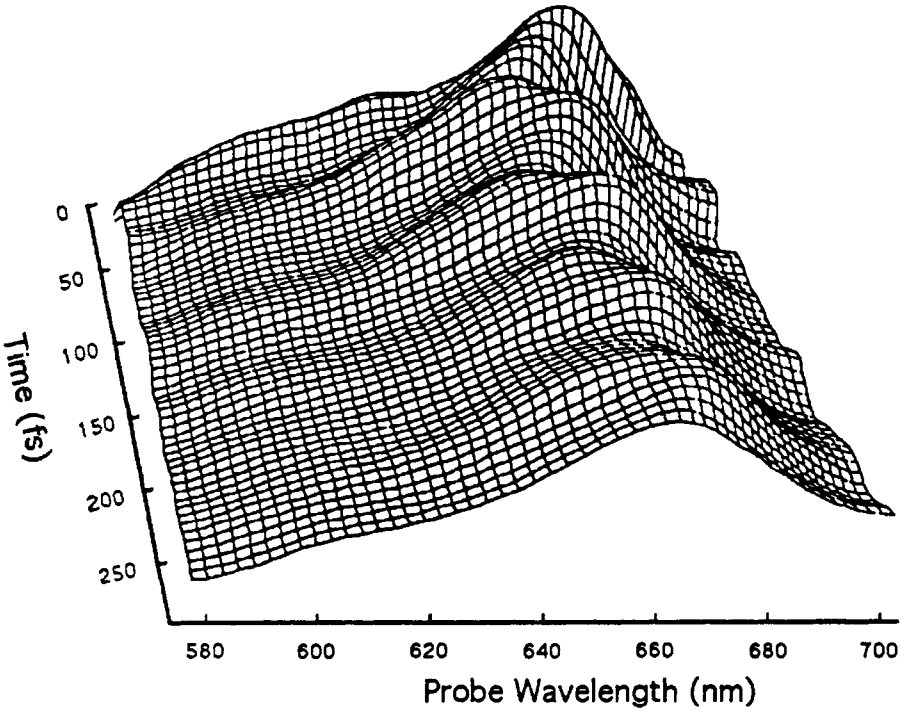

Figure 24. Three-dimensional plot of the absorption spectrum of nile blue as a function of time and wavelength. The pump and probe beams are 10 fs in duration. After passing through the sample, the probe beam is dispersed to yield the absorption spectrum from 530 to 700 nm. The oscillations in the spectrum result from impulsive excitation of the 590-cm^{-1} ring distortion mode of the dye. (Reprinted from ref 83. Copyright 1989 Elsevier Science Publishers.)

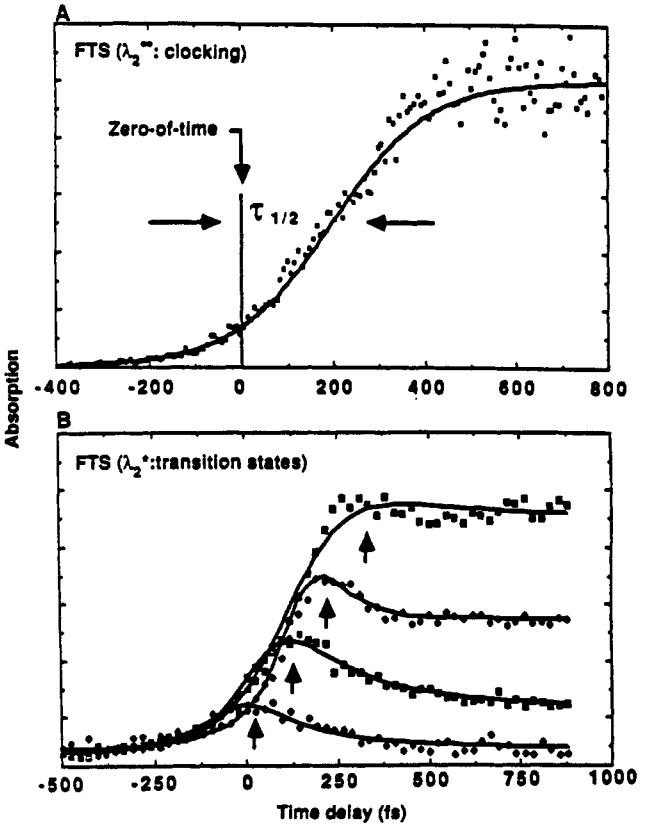

Figure 25. Time-resolved observation the reaction ICN* → [I···CN]* → I + CN through laser-induced fluorescence (LIF). (a) The probe wavelength corresponds to the absorption of the free CN fragments. The free CN appears in approximately 200 fs. (b) As the probe wavelength is tuned to the red (from bottom to top, λ = 391.4 nm, 390.4 nm, 389.8 nm, and 389.7 nm), the absorption maximum shifts to earlier times.

Figure 26c shows data from the bound excited state, with a series of excitation wavelengths. In this case it can be seen that higher excitation energies yield slower oscillation periods since the molecules are higher on the anharmonic potential energy surface. In addition, the decay of oscillations in the signal is faster with higher excitation energies since the more energetic molecules have a greater probability of barrier crossing. Note that this is very different from ordinary vibrational damping which occurs at all positions in the vibrational cycle.

These experiments can provide detailed information about dissociative potential energy surfaces as well as the dynamics of reaction along them. Strategies for inversion of time-resolved data of this sort to extract potential energy surfaces have been presented.[86-88]

Of course, molecular vibrations in the gas phase can also be observed without dissociation or other chemical reactions occurring. An example from molecular iodine is shown in Figure 27.[89] The data show oscillations at the fundamental vibrational frequency, modulated by molecular rotation. In addition, since molecular vibrations in the excited state are of fairly large amplitudes and the mode is anharmonic, the oscillations have a component at the first excited vibrational frequency which is somewhat less than twice the fundamental frequency. The fundamental and excited vibrational frequencies go in and out of phase in the data, resulting in the appearance and disappearance of the oscillations.

Measurements of transient absorption, rather than laser-induced fluorescence, from dissociating molecules in the gas phase have also been reported.[90-92] These measurements are difficult since the density of molecules is low and the net changes in absorption are small.

3. Femtochemistry in Condensed Phases

a. Liquids. After the successes of "femtochemistry" in the gas phase, time-resolved measurements of

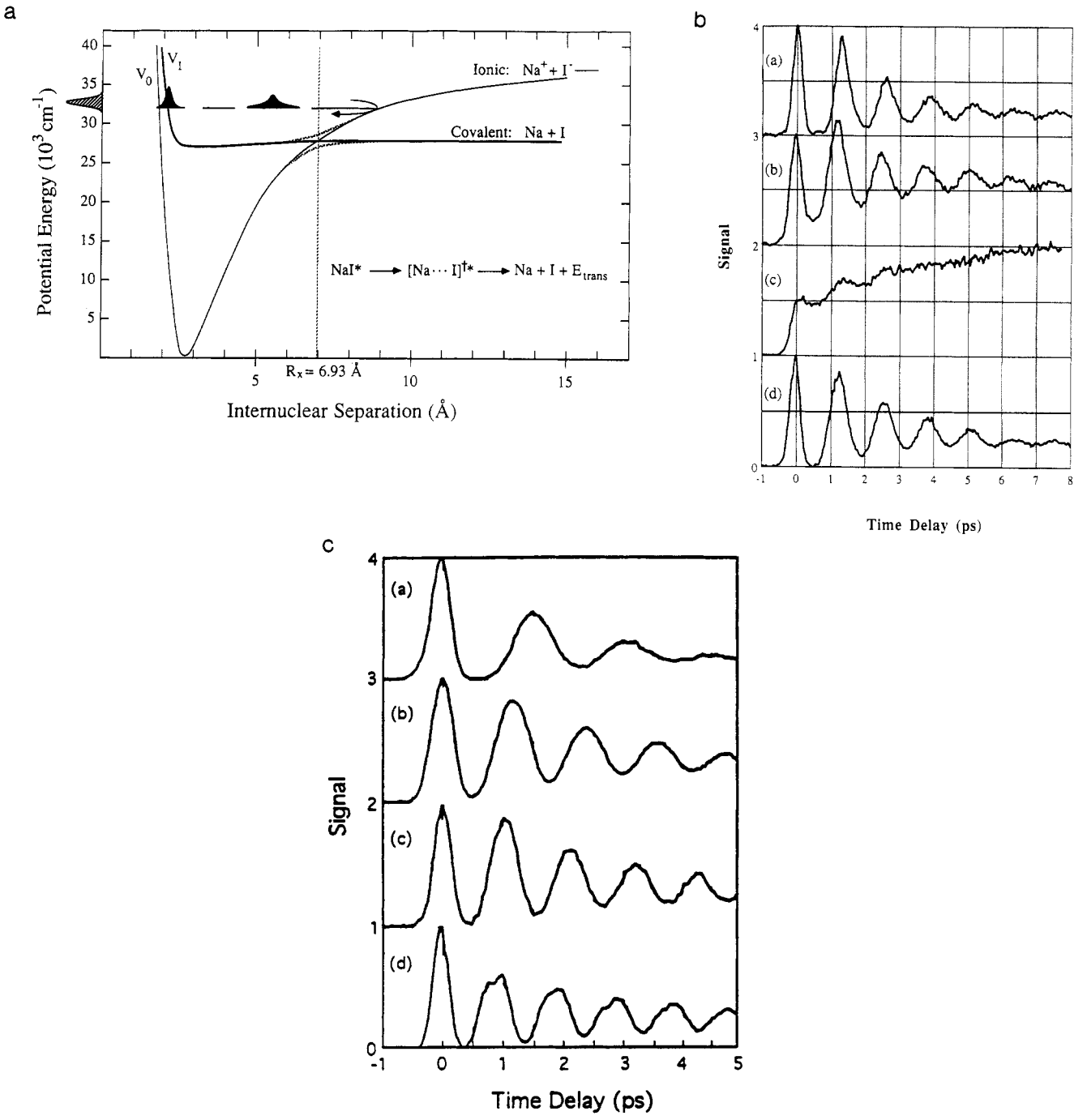

Figure 26. Part a shows potential energy curves describing the photodissociation reaction NaI* → [Na···I]* → Na + I. Part b shows LIF measurements from the reaction NaI* → [Na···I]* → Na + I. The bottom curve shows the oscillatory behavior of the wavepacket within ionic and covalent potential curves shown in a. The probability of escape of the wavepacket near the crossing point of the two curves is seen in the damping of the oscillations. The top curve is the result of detection of the free sodium atom. Part c shows LIF data demonstrating the effect of pump energy on excited-state wavepacket dynamics when exciting into an anharmonic potential surface. The pump wavelengths are (a) 300, (b) 311, (c) 321, and (d) 339 nm. As the pump wavelength is tuned to the red, the wavepacket explores progressively lower energy regions inside potential well and so the oscillation period and damping rate decrease. (Reprinted from ref 86. Copyright 1985 American Institute of Physics).

molecular photodissociation in liquids were initiated in order to understand the effect of the solvent upon chemical reactions. Two typical examples in the liquid state are presented in Figures 28 and 29. The first shows data from $Cr(CO)_6$ in which impulsive absorption of near-ultraviolet light leads to CO ligand loss which is observed in transient absorption measurements.[93,94] Subsequent complexation of the exposed Cr by solvent molecules can also be observed, and its dynamics were found in a number of studies to depend on the solvent size, viscosities, and other parameters. Figure 29 shows transient absorption data from radicals generated through photodissociation of an aryl disulfide.[95] The evolution of the time-dependent absorption spectrum reflects the dynamics of the initial dissociation process and the subsequent solvent response.

In recent experiments, impulsive absorption and resonant ISRS were combined in two separate excitation steps to first initiate and then probe liquid-state chemical reaction dynamics. Triiodide ions first absorb an ultrashort pulse, leading to dissociation into iodine and a diiodide ion. The I_2^- undergoes coherent vibra-

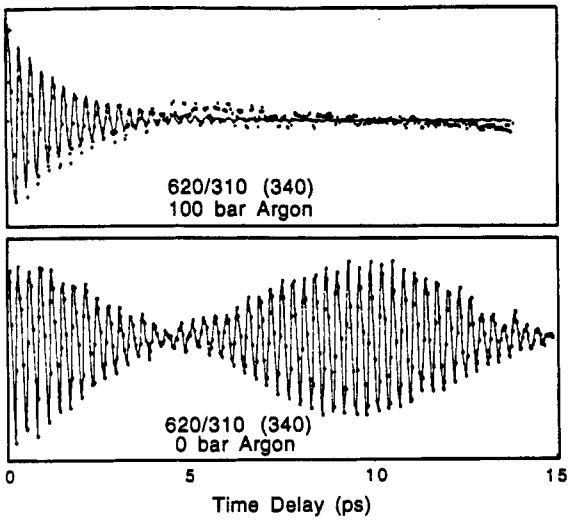

Figure 27. Laser-induced fluorescence measurements of iodine gas in the presence (upper curve) and absence (lower curve) of argon. 620-nm light is used to excite iodine to the B electronic state, and 310-nm light is used to probe the excited-state wavepacket dynamics. Fluorescence is collected at 340 nm. In the absence of argon, the anharmonicity of the excited-state potential well leads to the dephasing and rephasing of the oscillations of the wavepacket envelope. When argon is present, collisions between the iodine and argon gases yield a dissipative channel for the wavepacket and lead to an overall decay of the signal. (Reprinted from ref 90. Copyright 1992 Elsevier Science Publishers.)

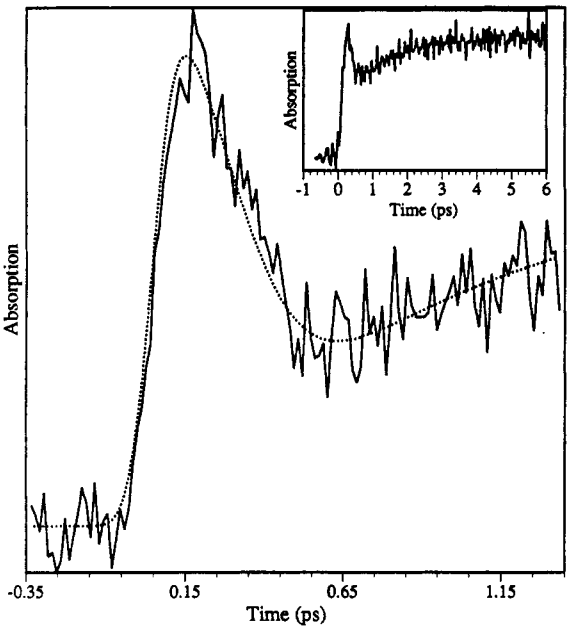

Figure 28. Transient absorption of $Cr(CO)_6$ in methanol. A 310-nm pump pulse leads to CO ligand loss while the 480-nm probe pulse used corresponds to the absorption maximum of the solvent-complexed species, $Cr(CO)_5(MeOH)$. The rapid nonexponential decay occurring in less than 500 fs is believed to correspond to coherent wavepacket propagation and dissociation on the excited-state potential energy surface. The subsequent slow (~1.6 ps) rise in the absorption is due to solvent complexation.

tional oscillations which were observed through the time-dependent changes in absorption of a resonant probe pulse.[96a] In the most recent experiments,[96b] a second excitation pulse was used for ISRS excitation of the diiodide ions after their initial coherent oscillations had ceased but while they still had high levels

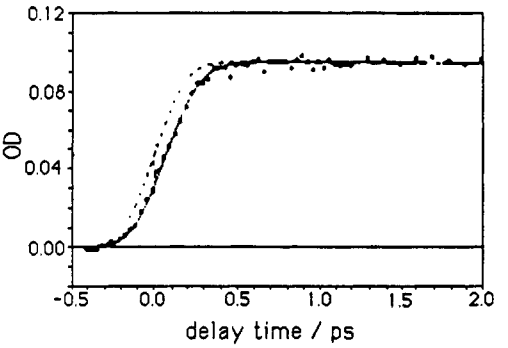

Figure 29. Ultrafast pump–probe data of bis(*p*-aminophenyl) disulfide in acetonitrile. Ultraviolet excitation generates two (*p*-aminophenyl)thiyl radicals which are probed through the use of a white light continuum. The temporal evolution of the absorption spectrum yields information on the vibrational relaxation of the thiyl radicals and the dielectric relaxation of the solvent (from ref 96).

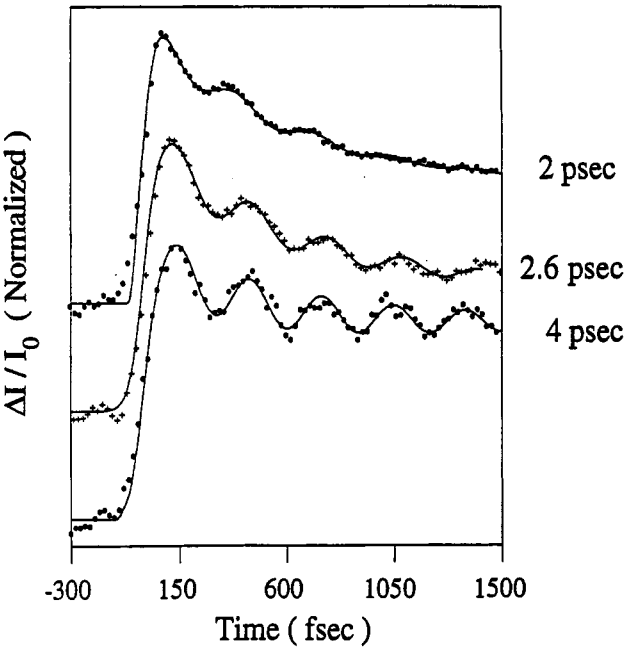

Figure 30. Resonance-enhanced ISRS data of nascent I_2^- ions formed through I_3^- photodissociation. The data were recorded with three different delays between the photodissociation pulse (at $t = 0$) and the ISRS excitation pulse. Transient absorption of a probe pulse is measured at times following the ISRS excitation pulse. The vibrational frequency increases at later ISRS excitation pulse delays as the I_2^- fragment ions vibrationally relax down to the bottom of the anharmonic potential energy well where their energy level spacings are larger. (Reprinted from ref 97. Copyright 1987 American Institute of Physics.)

of (incoherent) vibrational energy. The delay of this second excitation pulse relative to the first was varied, and the vibrational oscillations induced by the second pulse were observed (again through measurement of transient absorption of a time-delayed probe pulse) as shown in Figure 30. As the delay time of the ISRS excitation pulse was increased, the ions relaxed to the bottom of the anharmonic potential well where the vibrational energy level spacings are larger. Therefore the frequency of the oscillations increased at longer delay times. This new technique holds great promise for obtaining the vibrational relaxation dynamics of rapidly evolving systems.

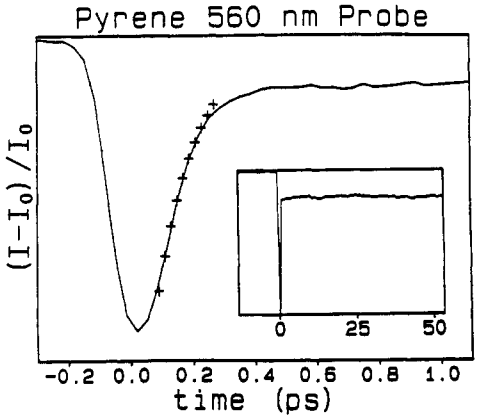

Figure 31. Femtosecond pump–probe data from pyrene single crystals at 300 K using a 615-nm pump pulse and 560-nm probe pulse. The fast increase in transmission after t = 0 is reasonably well described by a single exponential time constant of 140 fs and was interpreted to result from relaxation of the initially formed excited states into the excimer. The long-lived signal is due to the excimer whose lifetime is known to be 100 ns.

b. Solids. Time-resolved photochemistry experiments in solids represent an intriguing area of research since the relative positions and orientations of the reacting species are well defined, and the lattice ("bath") modes which may influence reaction dynamics are discrete phonon modes rather than ill-defined intermolecular motions as in the liquid state. However these experiments are more difficult than in gases and liquids because the sample cannot be flowed to remove reaction products and supply fresh material. In one class of photochemical reactions, excimer formation, this problem is alleviated since the excimer (excited-state dimer) separates following relaxation to the electronic ground state to regenerate the original monomers. In two crystalline solids the formation of excimers has been studied. These cases are also of interest in that they represent bimolecular reactions whose initiation does not require diffusion and therefore whose motions can be synchronized following impulsive absorption.

Figure 31 shows transient absorption data[97] from the organic molecular crystal pyrene which has the same crystal structure as α-perylene. The data show a rapid decay following excitation, after which the absorption level remains essentially constant for many picoseconds. These results were interpreted as indicative of ultrafast excimer formation. Time-dependent fluorescence measurements have indicated far slower (picosecond) excimer formation times.[98] The final story in this material remains uncertain, but it appears that at least substantial motion along the excited-state reaction coordinate occurs on a very fast time scale.

Figure 32 shows recent data recorded from NaCl crystals.[99] In these experiments a self-trapped exciton (STE) made up of a hole localized as a chloride molecular ion and a trapped electron is generated through two-photon absorption. A second pulse excites the molecular ion, whose relaxation dynamics are then probed. The evolution of time-dependent absorption spectra after excitation of the chloride molecular ion is due to both relaxation back to the original configuration and the formation of a new center where the molecular ion is significantly displaced (denoted as X). The oscillations are believed to represent the vibration

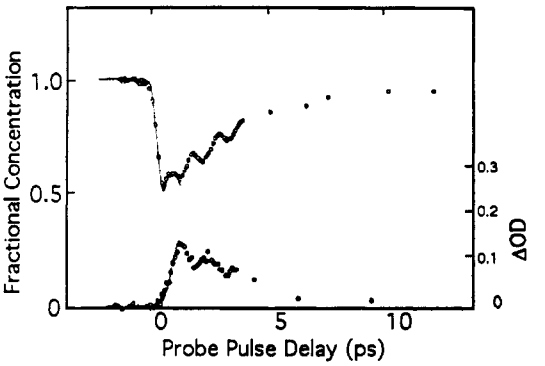

Figure 32. Time-resolved absorption of self-trapped excitons (STE) and X centers in NaCl crystals (the upper and lower curves, respectively). The STE and X centers are believed to correspond to different configurations of the halogen molecular ion. The oscillations in both spectra occur at a frequency of 1.1 ps and can be explained by a wavepacket coherently propagating in a double-minimum potential well where one minimum corresponds to the configuration of the STE center and the other minimum corresponds to the configuration of the X center. Note that the oscillations in the two spectra are of opposite phase, supporting the explanation that the wavepacket oscillates between the configurations of the STE center and the X center. (Reprinted from ref 100. Copyright 1991 American Physical Society.)

of the molecular ion about these two equilibrium configurations.

c. Biological Materials. Femtosecond time-resolved transient absorption spectroscopy of various biological molecules has been conducted, and in several cases the nuclear motion following photoexcitation is believed to have been phase coherent.[102] Figure 33 shows transient absorption spectra recorded from bacteriorhodopsin.[103] In this case absorption leads to very rapid isomerization coupled to relaxation into the (isomerized) ground electronic state. On the basis of the time scale for the spectral changes observed, it was deduced that the motion must be phase coherent. A biological role for phase coherence was proposed. The suggestion was that absorption into the side of the isomerization potential energy surface leads to a "spring"-like release of energy which drives the isomerization process at a rapid rate. This mechanism could optimize the quantum yield by minimizing the time available for relaxation or level crossing back to the ground state in the initial configuration.

A second biological example comes from photosynthetic reaction center of the D_{LL} mutant of *Rhodobacter capsulatus*.[103,104] The reaction reaction center in the wild type of this species displays the same kinetic and spectral behaviors to those of *Rhodobacter sphaeroids* R-26. The initially excited chlorophyll dimer known as the "special pair", labeled P, transfers an electron through the bacteriochlorophyll denoted as B_L (whose exact role in the process in under intense investigation) to the bacteriopheophytin, H_L, in a range from 0.7 to 3.5 ps, depending on the particular species and the sample temperature. In the D_{LL} mutant, the HL bacteriopheophytin is missing. Impulsive absorption into the excited state of the special pair, P*, in the mutant gave rise to coherent vibrational oscillations, indicating a dramatic effect due to the absence of electron transfer beyond the bacteriochlorophyll. Transient absorption data are shown in Figure 34. Two oscillating features are detected, one with a period of

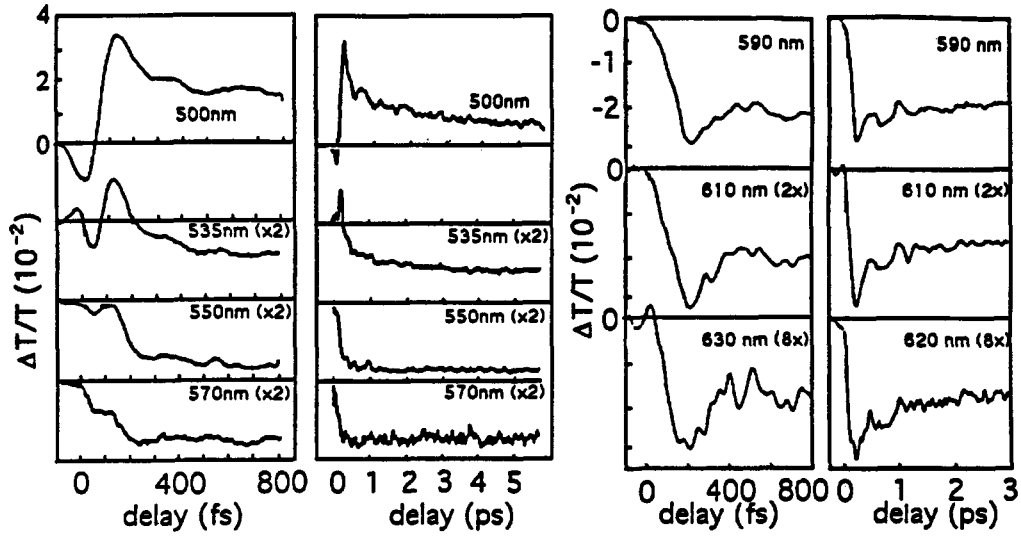

Figure 33. Transient absorption data from 11-*cis*-rhodopsin after excitation with a 35-fs pump pulse centered at 500 nm. Oscillatory behavior at all probe wavelengths is due to resonance-enhanced ISRS excitation. The absorptions at 570 and 550 nm is due to the photoproduct, the trans configuration. Absorption at 535 nm is at the red edge of the cis absorption band and the blue edge of the trans absorption band. The initial dynamics are ascribed to wavepacket spreading and motion on the excited-state potential energy surface while the long-time dynamics are due to vibrational cooling of the photoproduct. (Reprinted from ref 102. Copyright 1992 National Academy of Sciences.)

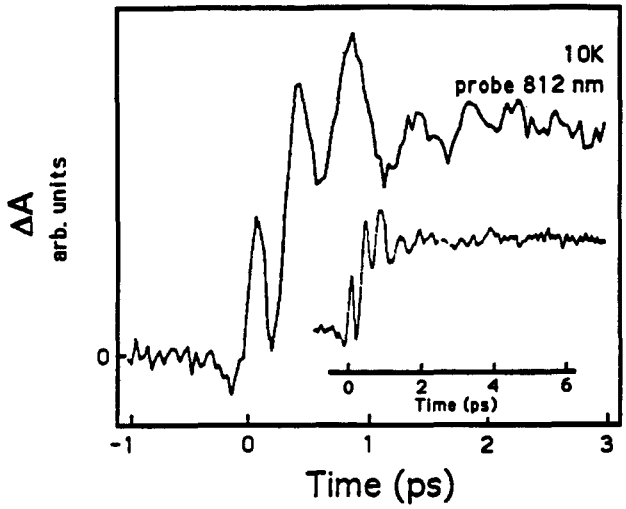

Figure 34. Time-resolved absorption data from chromatophores of *R. capsulatus* D_{LL} at 10 K in the Q_Y region. A 45-fs excitation pulse centered at 870 nm and a probe pulse centered at 812 nm were used. The period of the oscillations is initially 500 fs but increases somewhat at later times. A slower oscillation period of 2 ps is also observed and is seen more clearly in the inset. (Reprinted from ref 103. Copyright 1992 National Academy of Sciences.)

approximately 460 fs and the other with a period of 2 ps. The observed periods are characteristic of global protein motion. Although there is no direct evidence for coupling of the 2-ps mode to the electron-transfer reaction, it is postulated that the charge-transfer process is marked by an oscillating charge distribution, perhaps the intermediate $P^+B_L^-$ state. Another important suggestion of the coherent vibrational motion is that electron transfer does not occur from a vibrationally relaxed state as was previously believed.

4. Resonance Excitation of Collective Vibrational Modes

The examples of resonant excitation discussed above all involve localized molecular excited states and molecular vibrations, at least according to the interpretations given here. (Possible exceptions would include the crystalline and photosystem cases.) In several materials including semiconductors, metals, and superconductors, resonant initiation of collective vibrational modes has been reported. This provides a mechanism complementary to ISRS for observation of coherent vibrations that may be relevant to phase transitions and other important collective phenomena.

Figure 35, parts a and b, show transient absorption data from mercuric iodide, HgI_2, a wide-bandgap semiconductor,[104,105] and GaAs, a narrow-bandgap material.[106,107] The oscillations are due to optic phonons excited through impulsive absorption. Promotion of electrons into the conduction band is believed to reduce screening between positively charged nuclei and, thereby, changes the local equilibrium positions of the nuclei in the unit cell. This initiates coherent vibrational motion along optic phonon coordinates with significant vibronic coupling to the electronic excited state.

Figure 36 shows transient reflection data of similar appearance recorded from the high-T_c superconductor $Y_1Ba_2Cu_3O_{7-\delta}$.[107] The feature of particular interest is the change in oscillation amplitude as a function of temperature near the superconducting transition temperature T_c. The reduced amplitude below T_c indicates reduced electron–phonon coupling in the superconducting phase.

Figure 37 shows transient reflectivity results from antimony samples.[108-110] There are two features of special interest in these results. First, the amount of change in reflectivity due to coherent lattice vibrations is several percent, which indicates vibrational motion of unusually large amplitude. Second, the vibrational amplitude was found to increase linearly with excitation intensity. This is in contrast to the case of molecular vibrations. In molecular samples, if more excitation light is used then there are more molecules which are excited but there are a negligible number of molecules which are excited into higher-lying excited states. Thus for each molecule the vibrational amplitude is essen-

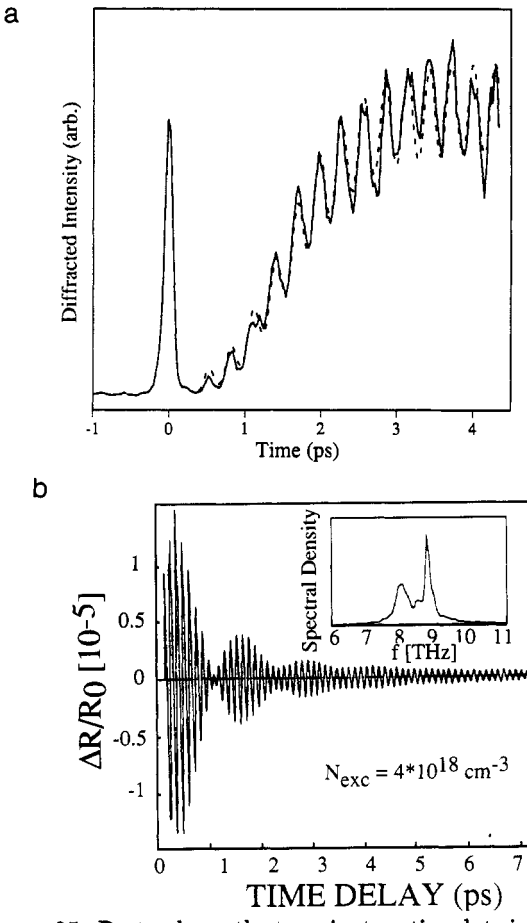

Figure 35. Part a shows the transient grating data in single-crystal mercuric iodide at 78 K. The oscillations in the data correspond to coherent vibrations of the 114 cm^{-1} A_{1g} mode in HgI_2. The rising signal level is due to the relaxation of hot carriers, excited through two-photon absorption, to the free exciton state. Part b shows the interference between a longitudinal and a transverse optic mode in GaAs generated through ultrafast excitation. The longitudinal mode is excited under carrier density conditions ($\sim 4 \times 10^{17}$ cm^{-3}) where the plasma frequency is in resonance with the longitudinal mode. (Part a, from ref 105. Part b, reprinted from ref 108. Copyright 1991 American Institute of Physics.)

tially fixed by the amount of shift between the ground- and excited-state potential energy minima independent

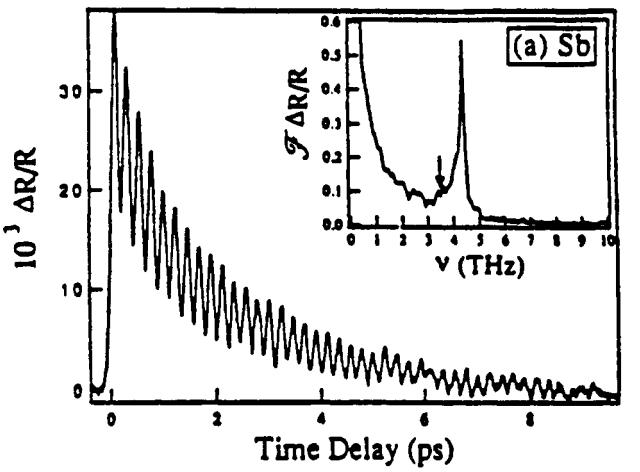

Figure 37. Time-resolved reflectivity data from single-crystal antimony. Oscillations in the signal intensity occur with a period of 0.22 ps and correspond to the lowest frequency A_1 mode in antimony. A Fourier transform of the data (inset) shows no evidence of the low-frequency E_g mode, yielding support for an impulsive absorption mechanism of excitation rather than an ISRS mechanism.

of excitation intensity. On the other hand, for collective electronic excitations such as those in conductors, increased excitation pulse intensity leads to a higher density of "hot" carrier electrons and reduced screening among ions in the unit cells. Thus the collective vibrational amplitude increases (approximately linearly) with excitation intensity. In the material shown in Figure 38, an estimated coherent vibrational amplitude of up to 0.05 Å was induced. Still higher excitation intensities could not be used without melting the sample. At low intensities, the phonon frequency characteristic of the semimetal is seen.

V. Multiple-Pulse Femtosecond Spectroscopy: From Observation of to Control over Sample Behavior

Experimental control over the dynamical behavior of a sample remains a major goal for the field of ultrafast spectroscopy. Progress in this direction has been achieved in several experiments in which successive

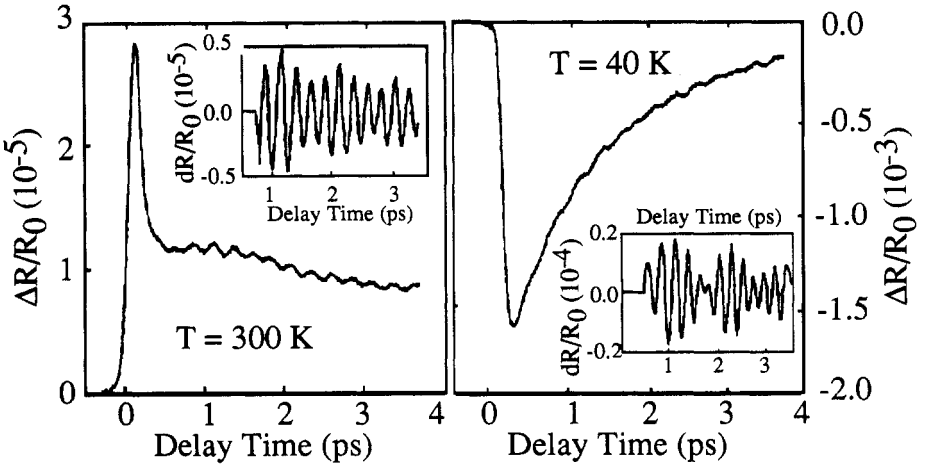

Figure 36. Time-resolved reflectivity data from a 300-nm-thick film of $Y_1Ba_2Cu_3O_{7-\delta}$ on a $SrTiO_3$ substrate. The oscillations are more clearly seen in the insets where the slowly decaying background has been subtracted. The oscillations are ascribed to the 120-cm^{-1} vibration of the Ba and the 150-cm^{-1} vibration of the Cu(2). (Reprinted from ref 108. Copyright 1991 American Institute of Physics.)

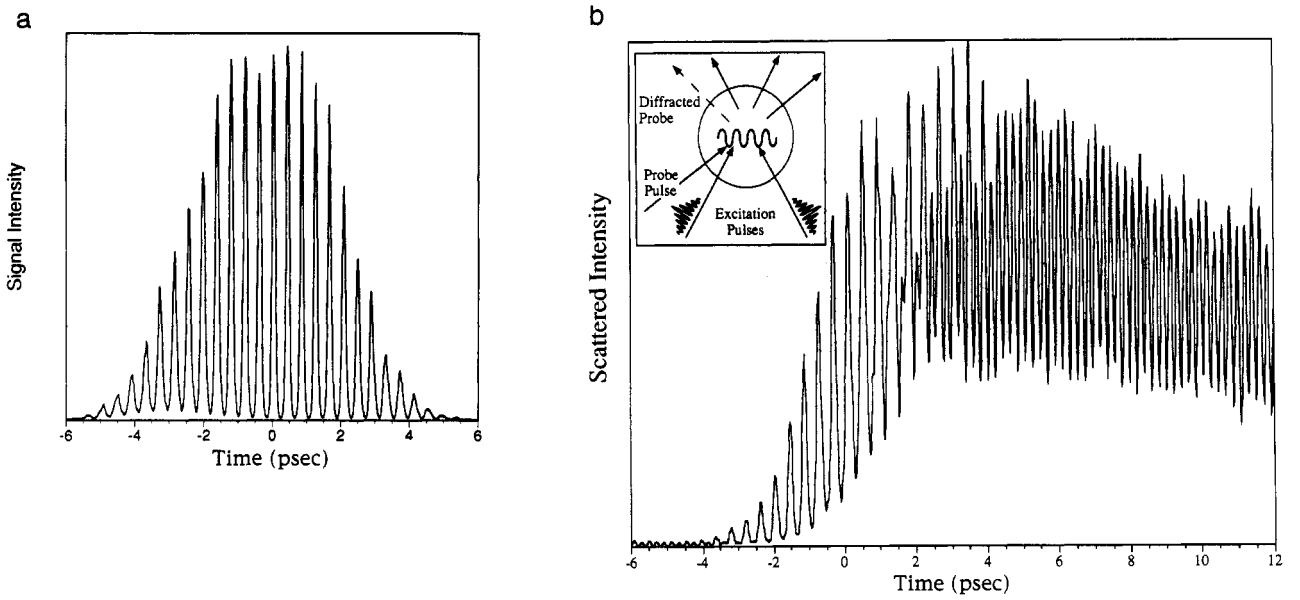

Figure 38. Part a shows the cross-correlation of a sequence of pulses created through femtosecond pulse-shaping techniques. The repetition rate of the pulse sequence is 2.39 THz, matching the oscillation period of the 80-cm^{-1} optic phonon mode which corresponds to in-phase librations of molecular pairs in α-perylene. Part b shows ISRS data recorded from α-perylene at 5 K, using the multiple excitation pulse sequence of a. After about 10 pulses, lattice vibrational oscillations (at twice the driving frequency) become apparent. The signal due to vibrations continues to increase for the duration of the excitation pulse train, demonstrating multiple-pulse ISRS vibrational amplification.

impulsive stimulated scattering or impulsive absorption events were used. Vibrational phase coherence has been manipulated with femtosecond pulse sequences of more than 10 pulses. Electronic and vibrational phase coherences have been manipulated with pairs of pulses, in some cases with related optical phases. In each of these cases, sample responses which could not be elicited through single pulses were induced.

A. Multiple-Pulse Impulsive Stimulated Raman Scattering

The first multiple-pulse ISRS experiment was conducted using a femtosecond pulse-shaping technique developed for optical communications applications.[111] Through this method it is possible to transform a single femtosecond pulse into an almost arbitrarily complex waveform whose amplitude and phase profiles are controlled. A simple pulse sequence consisting of evenly spaced femtosecond pulses is shown in Figure 38a. In multiple-pulse ISRS experiments on α-perylene crystals,[112,113] such a sequence of nonresonant pulses was used to exert a series of impulsive driving forces on one of the Raman-active lattice vibrational modes. By timing the pulse sequence to match the vibrational frequency, the coherent vibrational amplitude was increased substantially over that driven by a single pulse. ISRS data recorded from α-perylene with a single excitation event were shown in Figure 10. Several optic phonons are excited whose oscillations go in and out of phase, leading to a "beating" pattern in the data. Note also that the intensity of the signal due to lattice vibrations is only about 4% of that at $t = 0$ due to the nonresonant electronic response of the sample. ISRS data recorded with multiple excitation pulses are shown in Figure 38b. The signal due to lattice vibrations increases with each successive pulse, becoming apparent after about 10 pulses have passed through the sample

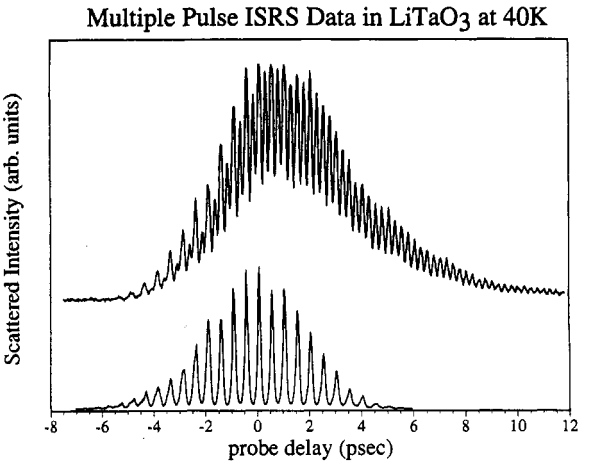

Figure 39. ISRS data from $LiTaO_3$ at 40 K (top curve), recorded utilizing multiple excitation pulses (cross-correlation shown in bottom curve). The multiple-pulse technique allows the vibrational dynamics to be observed with significantly lower peak pulse intensities than those needed with a single excitation pulse. This circumvents photorefractive damage which occurs at low temperatures.

and continuing for many picoseconds after the excitation pulsetrain is over. The signal due to the vibrations becomes larger than that due to nonresonant electronic effects at $t = 0$, in contrast to the 4% relative signal level observed after one excitation event. Substantial (about 10-fold) vibrational amplification of the selected mode and suppression of the other modes was achieved in this manner.

A more recent example from $LiTaO_3$ is shown in Figure 39.[74] In this case, photorefractive damage of the crystal at reduced temperatures frustrated ISRS experiments with single excitation pulses. When the single excitation pulses were sufficiently intense to yield detectable signals, two-photon absorption occurred and led to damage. Multiple excitation pulses produced vibrational amplitudes sufficient for reliable data

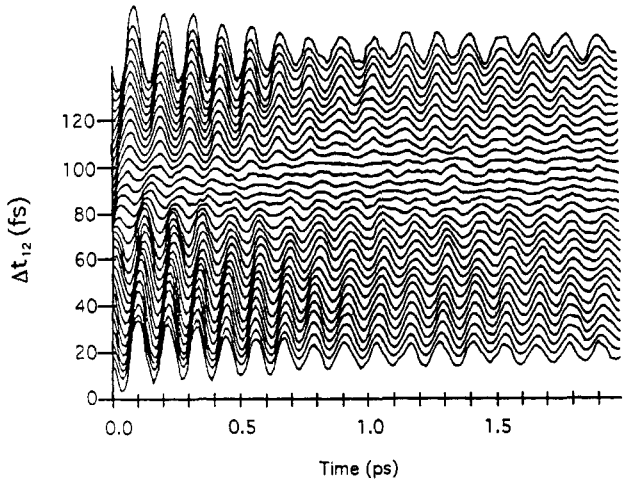

Figure 40. Constructive and destructive interferences between longitudinal optic phonons in GaAs. Two pump pulses are separated by a time Δt_{12}. When $\Delta t_{12} = n\nu_{LO}^{-1}$ where n is an integer, constructive interference between the vibrational responses to the two pulses is observed. When $\Delta T_{12} = (n + {}^1/_2)\nu_{LO}^{-1}$, destructive interference is observed. Δt_{12} denotes the time interval between the second pump pulse and the probe pulse. (Reprinted from ref 108. Copyright 1991 American Institute of Physics.)

collection with substantially reduced peak pulse intensities, permitting experiments like those discussed earlier on $LiTaO_3$ to continue at reduced temperatures.

ISRS experiments on GaAs have also been conducted with pairs of nonresonant excitation pulses whose timing was varied such that the two vibrational responses were either in or out of phase.[114] Figure 40 shows data demonstrating that the net vibrational amplitude is either increased or decreased and, in general, the vibrational phase is shifted, depending on the timing of the two excitation events relative to the optic phonon oscillation period.

A similar experimental concept was executed on acoustic phonons much earlier, using pairs of picosecond excitation pulses.[115] Figure 41 shows data in which two pairs of crossed excitation pulses are used to excite acoustic responses which are either in or out of phase with each other. The results, similar to those reported for ISRS experiments, are that the first acoustic response can be amplified or cancelled by the second, and in general the net acoustic amplitude and phase are shifted, depending on the timing of the two excitation events relative to the acoustic oscillation period.

B. Resonant Multiple-Pulse Experiments

1. Manipulation of Vibrational Coherence and Chemical Control

Several experiments have been reported in which multiple impulsive absorption events have been used to manipulate molecular motion along excited-state potential energy surfaces. In an early example of experiments of this kind, vibrational coherences in the excited "B" state of molecular iodine were manipulated.[116] The results are shown in Figure 42. The first pulse excited some molecules which underwent wavepacket propagation (coherent vibrational motion) along

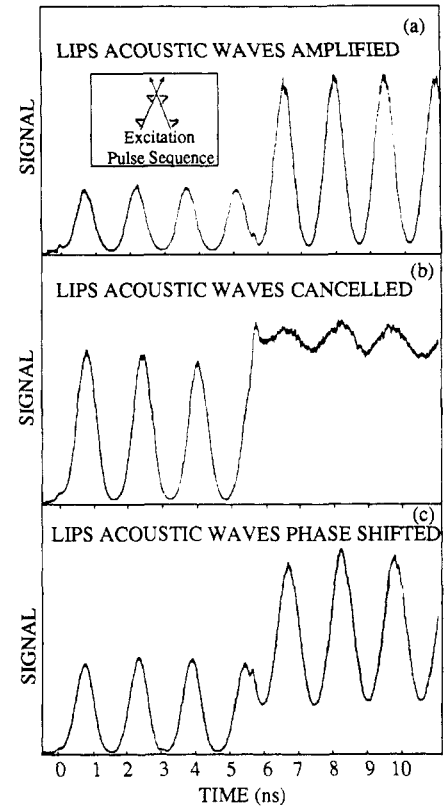

Figure 41. Transient grating data showing multiple-pulse excitation of acoustic waves in a solution of cresyl violet in ethanol. (a) A second pair of excitation pulses arrives at time $8\pi/\omega$ after the first pair of pulses, amplifying the coherent acoustic waves. (b) The second pair of excitation pulses arrives at time $7\pi/\omega$ after the first pair, opposing the acoustic response that was generated initially. (c) The second pair arrives at time $7.34\pi/\omega$, phase shifting the acoustic waves. (Reprinted from ref 116. Copyright 1990 American Physical Society.)

the excited-state potential energy surface, and the second pulse excited more molecules whose coherent vibrations were either in or out of phase with those of the molecules excited first. The net vibrational coherence, observed through laser-induced fluorescence as in other gas-phase experiments, was amplified, reduced, and/or phase shifted depending on the timing of the two excitation events relative to the molecular vibrational oscillation period. Note that although the data in Figure 42 appear similar to those shown earlier, they are fundamentally different in that the observed amplification or reduction of coherent oscillations is due to superposition of coherent signals from different vibrational coherences, one of which (excited by the first pulse) oscillates with a phase that is different than that of the another (excited by the second pulse). The vibrational amplitudes are not different in the two groups, and the second pulse does not increase or decrease the vibrational amplitudes of the molecules which were excited by the first pulse. In contrast, in multiple-pulse ISRS experiments the same impulse driving force is exerted by each pulse on all the (collective or molecular) oscillators and their individual vibrational amplitudes are increased or decreased depending upon the arrival time of each pulse.

An elegant extension of this experimental approach to the area of chemical control was demonstrated recently. In this case, weakly-bound linear complexes of molecular iodine with xenon atoms were examined.[117]

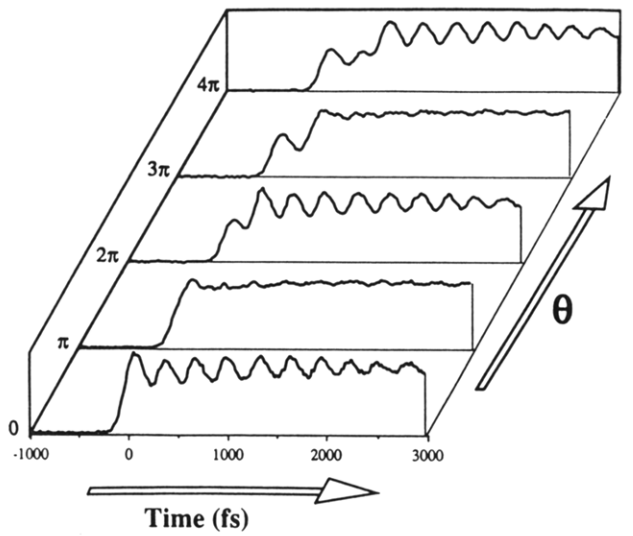

Figure 42. The results of a three-pulse experiment demonstrating control of excited-state wavepacket motion in iodine. The first pulse initiates wavepacket propagation and the second pulse produces a second wavepacket which may interfere either constructively or destructively with the first. The timing of the second pulse is indicated by the phase angle T which is defined to be $\omega_1\tau_1$ where ω_1 is the frequency of the wavepacket and τ_1 is the delay between the first and second pulses. Alternate constructive and destructive interference results in amplification or cancellation of the oscillations appearing in the signal. The signal is the fluorescence intensity induced by a third pulse. The wavelengths of the pump pulses are 620 nm while the wavelength of the probe pulse is 310 nm. (Reprinted from ref 117. Copyright 1990 Elsevier Science Publishers.)

Excited-state vibrations of molecular iodine were initiated through impulsive absorption of a single femtosecond pulse, as illustrated in Figure 27. A second pulse was used to induce electron transfer from the weakly-bound xenon atom to the iodine atom nearest to it. The interesting result, illustrated in Figure 43, was that the electron-transfer probability could be controlled to a considerable degree depending on the phase of the iodine vibrations. At the outer vibrational turning point, which the I–I bond stretched and the I–Xe distance minimized, the electron-transfer probability was maximized. At the inner turning point, greatly reduced electron transfer was observed. These results provide a graphic illustration of some of the possibilities for control over chemical reactivity through manipulation with multiple femtosecond pulses.

2. Manipulation of Electronic and Vibrational Phase Coherences

Additional control over molecular behavior can be achieved through experimental manipulation over electronic as well as vibrational phase coherence. Experimentally, this may require control over the phases of optical pulses as well as over their relative intensities and timing. Pulse-shaping techniques for achieving this have been demonstrated, as discussed briefly above. Several methods are currently in use and are improving rapidly.

An early example of manipulation of electronic phase coherence only was demonstrated with sodium atoms.[118] In this case, two pulses whose relative optical phases were controlled were used. The first pulse initiates phase coherence involving the ground and excited

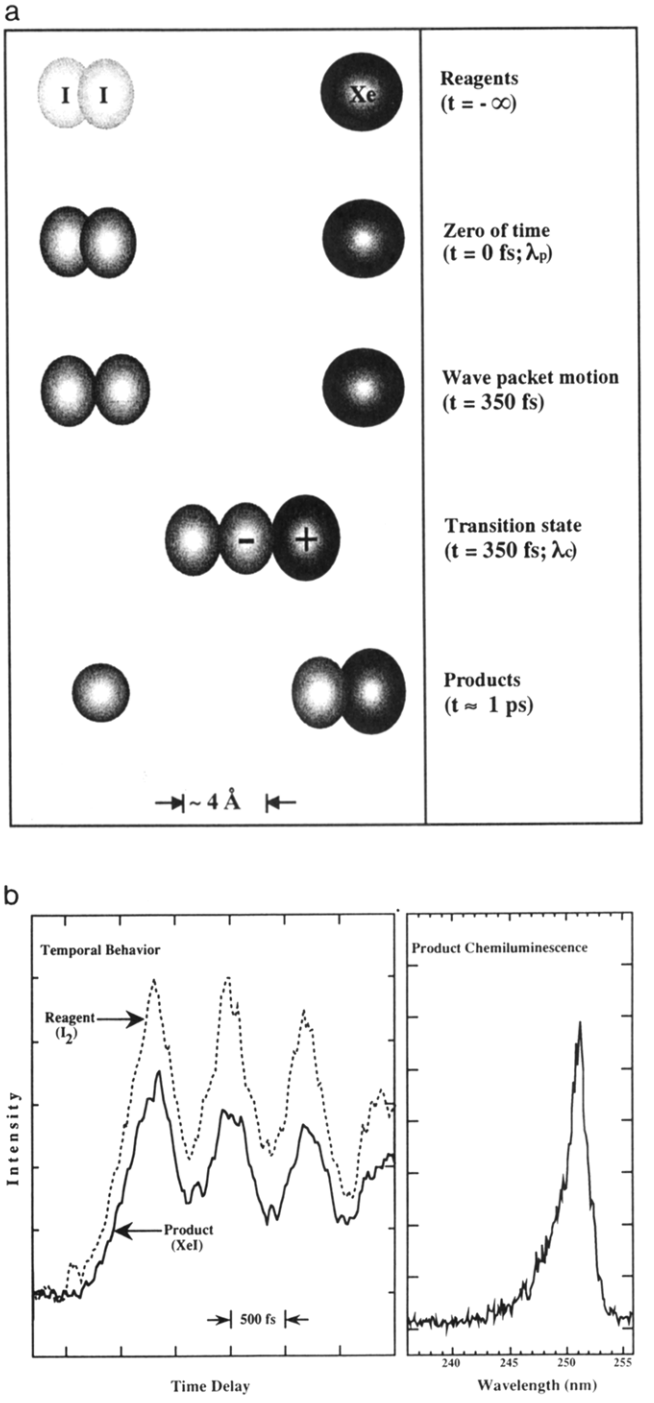

Figure 43. The sequence of events in an optically controlled electron transfer reaction between xenon and iodine is illustrated in part a. The pump pulse (λ_p = 515 nm) excites the iodine (I_2) from its ground electronic state to an excited electronic state, creating a well-defined excited-state wavepacket. The oscillations of the wavepacket correspond to variations from 2.5 to 5.0 Å of the iodine internuclear separation. The control pulse (λ_c = 260 nm) arrives at some time during the vibrational cycle and moves the wavepacket into a higher lying electronic level from which an electron transfer reaction with xenon occurs. Part b shows chemiluminescence of the product of the reaction, Xe + I_2 → XeI (lower curve), as a function of time delay between the pump pulse and the control pulse. If the control pulse arrives at the time when the iodine wavepacket is at its outer turning point, the reaction of the iodine and the xenon is enhanced as seen by the peaks in the XeI chemiluminescence signal. The I_2 signal is obtained by monitoring the laser-induced fluorescence of the bare iodine atom at 340 nm. (Reprinted from ref 117. Copyright 1992 Nature.)

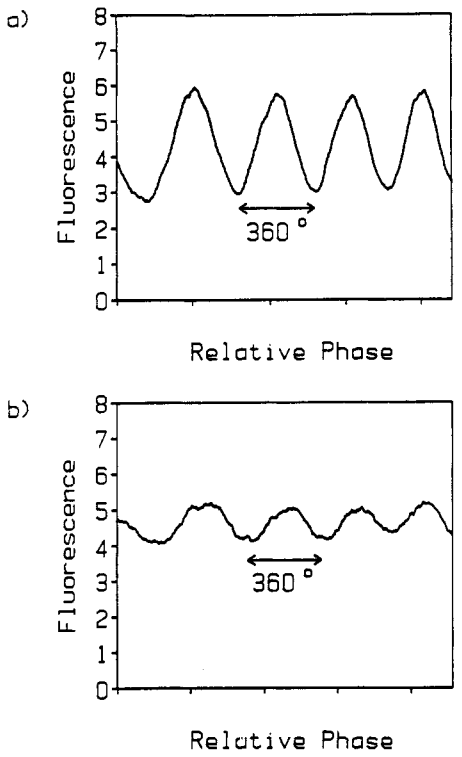

Figure 44. Part a shows the excitation of sodium vapor with two pulses whose relative optical phases are under experimental control. The two pulses are tuned to the Na D_1 line at 5896 Å. Incoherent fluorescence is measured as a function of the relative phase between the pulses. The delay between the two pulses is maintained at 107 ps so they do not overlap in time. The electronic coherences generated by the two pulses add constructively or destructively depending on the optical phase, giving rise to the phase-dependent oscillations in the data. In part b, the delay between the pulses is 200 ps. The same dependence on the relative phase as seen in a is observed but the lower amplitude of the fluorescence intensity is due to the free induction decay of the system. (Reprinted from ref 119. Copyright 1990 American Institute of Physics.)

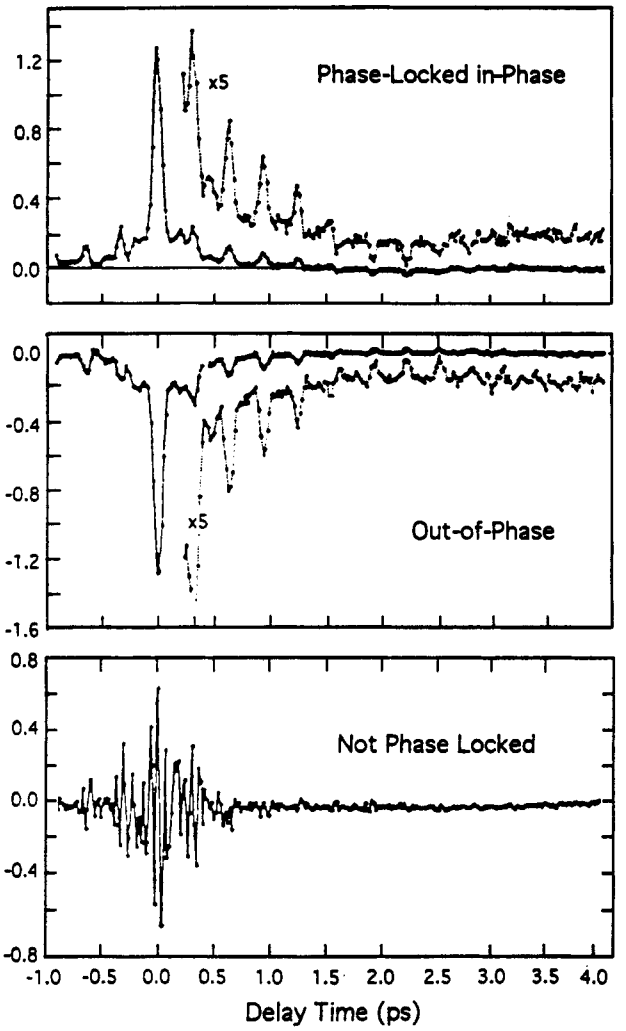

Figure 45. Phase-locked excitation of iodine vapor at 300 K, with incoherent fluorescence measured. The beams are modulated so that only the fluorescence due to both pulses is detected. The first scan shows the constructive interference of the wavepackets created by the pump and probe pulses when the two are phase locked. The second scan demonstrates the destructive interference of the wavepackets when the pulses are phase shifted by 180°. The third scan shows the result when there is no active phase locking between the two pulses. (Reprinted from ref 120. Copyright 1990 American Institute of Physics.)

electronic levels. This can be thought of physically in terms of oscillations of the electron cloud around each irradiated atom. The second pulse either amplifies or reduces the coherence depending on the optical phase relative to the electronic phase, i.e. depending on the relative phases of the two pulses. The results are determined through measurement of the total fluorescence intensity. Data are shown in Figure 44 illustrating the dependence on the relative optical phases.

The first example of manipulation of both electronic and vibrational phase coherence on a time scale short compared to the vibrational period is illustrated in Figure 45.[119-121] Impulsive absorption of the first pulse initiates molecular vibrations in the iodine B state, as shown earlier. It also initiates electronic phase coherence involving the ground and excited electronic levels, just as in atomic sodium. In the multiple-pulse experiments discussed above on molecular iodine, electronic phase coherence was also initiated by the first pulse but was not observed since relative phases of the subsequent pulses were not controlled. Figure 46 shows that a second phase-controlled pulse either increases or decreases the net electronic phase coherence and the ultimate net fluorescence intensity, just as in the case of sodium. However, an important difference between the molecular and atomic cases arises through the combined electronic and vibrational phase coherences. The vibrational motion in the excited state changes the electronic transition frequency, so that the second pulse is not on resonance with the transition in excited molecules which are vibrationally distorted away from the ground-state bond length. The situation is illustrated in Figure 46. The result is that manipulation of the electronic phase coherence with a second pulse is only possible after integral numbers of vibrational cycles, when the excited molecules return to their initial bond lengths and the transition frequency returns to its original value.

The results on molecular iodine depend on molecular rotation as well, since as the excited molecules rotate their transition dipoles change in magnitude. It is worth pointing out that experiments have been conducted to demonstrate that with properly "shaped" pulses the electronic phase coherence can be extended to include molecules in a wide range of initial rotational levels and orientations.[121] The experiments were conducted

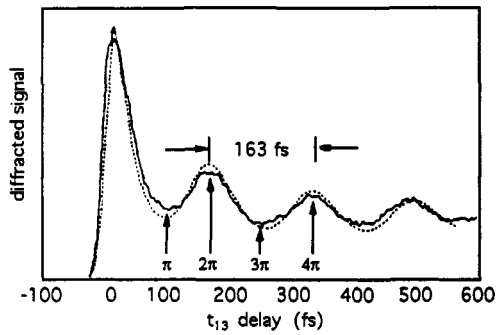

Figure 46. Three-pulse photon echo of 22 Å CdSe nanocrystals. The time delay between the first and second pulses is held constant at 33 fs while the time delay between the first and third pulses is varied to demonstrate the modulation of the echo signal by the coherent vibrational excitation induced by the first excitation pulse. The time delay labeled by π marks the third pulse arriving out of phase with the coherent vibration of the nuclei while the delay labelled by 2π marks the third pulse arriving when the nuclei have returned to their original positions. The dashed line shows the predicted stimulated echo signal of an inhomogeneously broadened system with a single harmonic phonon mode. (Reprinted from ref 123. Copyright 1993 American Physical Society.)

on picosecond time scales and therefore vibrational phase coherence was not monitored, but the results indicate that molecular rotation can be incorporated into the excitation design to minimize its reduction of control over vibrational and electronic phase coherences.

Electronic and vibrational phase coherences have been manipulated in condensed phases as well. In recent work investigating electronic dephasing in CdSe nanocrystals, a three-pulse photon-echo technique was used to separate the contributions of coherently excited LO-phonons and electron–hole dephasing to electronic dephasing.[122] Figure 46 shows the echo signal detected at the phase-matched direction $(-k_1 + k_2 + k_3)$ as a function of delay between the first and third pulses-(t_{13}) where the delay between the first two (t_{12}) is fixed. The oscillations result from the coherent excitation of the 205-cm^{-1} LO phonon mode of the CdSe nanocrystal. By delaying the third pulse from the first by exactly one LO phonon period so that the nuclei have returned to their original positions after excitation by the pulse at t_1, the quantum beat modulation of the echo signal was eliminated. Figure 46 shows the echo signal for various fixed t_{13} and variable t_{12} delays. Using this manipulation of the contribution of the vibrational coherence, the authors were able to carefully explore the dynamics of the polarization dephasing.

In a broader sense, the experiments reviewed in this section represent the very early stages of molecular and material manipulation through the use of complex femtosecond waveforms. The technology for generating and manipulating such waveforms is still evolving rapidly, as is the theoretical and experimental apparatus for optimizing waveforms to achieve desired objectives. Continued progress in this area may lead to dramatic advances in optical control over molecular and material behavior.

VI. Summary

It is now routinely possible to produce optical pulses whose duration is short compared to the time required for nearly any motion of atoms or molecules, i.e. collective vibrations in condensed materials, molecular rotations, and many molecular vibrations. This makes time-resolved observation of these motions possible in principle. The other requirement is a mechanism through which ultrashort pulses can initiate and monitor collective or molecular motion. We have reviewed the mechanisms discovered and exploited to date, primarily impulsive stimulated scattering and impulsive absorption, for initiation of phase-coherent motion in electronic ground and excited states, respectively. The conceptual and theoretical underpinnings for the excitation mechanisms and the different ways in which phase-coherent motion can be monitored were presented.

Spectroscopic applications of impulsive stimulated scattering and impulsive absorption were reviewed. The initial efforts in each case were aimed at demonstration and understanding of the excitation mechanisms. More recently, a substantial body of results which were not obtainable through other spectroscopic means has been amassed. Through impulsive stimulated scattering, information about the dynamics of structural phase transitions, molecular liquids, and vibrational relaxation of chemical reaction products has been extracted. Impulsive absorption has provided information about electron–phonon interactions in a variety of crystalline solids and has made possible the entire area of "femtochemistry" which now extends throughout gas, liquid, and solid phases and includes photobiological materials.

Finally, multiple-pulse femtosecond spectroscopy at the impulsive limit was reviewed. This is a relatively new area but one whose accessibility to broad use and whose prospects are growing rapidly. Just as the availability of ultrashort pulses led to dramatic advances in our capabilities for observation of elementary collective and molecular motions, the availability of tailored ultrafast waveforms may be expected to herald similar advances in our level of control over these motions and over the chemical and structural changes resulting from them.

VII. Acknowledgments

Partial support from NSF grants no. CHE-8901722 and DMR-9002279 is acknowledged. Lisa Dhar acknowledges support from a DOD Graduate Fellowship and a grant from the AT&T Graduate Research Program for Women. John Rogers acknowledges support from an NSF Predoctoral Fellowship.

VIII. References

(1) Yan, Y.-X.; Cheng, L.-T.; Nelson, K. A. In *Advances in Nonlinear Spectroscopy*; Clark, R. J. H., Hester, R. E., Eds.; Adv. in Spectrosc. Series; Wiley: Chichester, 1988; Vol. 16, p 299.
(2) (a) Yan, Y.-X.; Nelson, K. A. *J. Chem. Phys.* **1989**, *87*, 6240. (b) Yan, Y.-X.; Nelson, K. A. *J. Chem. Phys.* **1989**, *87*, 6257.
(3) Nelson, K. A.; Ippen, E. P. *Adv. Chem. Phys.* **1989**, *75*, 1.
(4) Chesnoy, J.; Mokhtari, A. *Phys. Rev. A* **1988**, *38*, 3566.
(5) Walmsley, I. A.; Wise, F. W.; Tang, C. L. *Chem. Phys. Lett.* **1989**, *154*, 315.
(6) Walsh, A. M.; Loring, R. F. *Chem. Phys. Lett.* **1989**, *160*, 299.
(7) Shen, Y. R. *The Principles of Nonlinear Optics*; Wiley-Interscience: New York, 1984.
(8) Nelson, K. A.; Williams, L. R. *Phys. Rev. Lett.* **1987**, *58*, 145.
(9) Wise, F. W.; Rosker, M. J.; Tang, C. L. *J. Chem. Phys.* **1987**, *86*, 2827.
(10) Dougherty, T. P.; Wiederrecht, G. P.; Nelson, K. A. *J. Opt. Soc. Am. B* **1992**, *9*, 2179.

(11) Berne, B. J.; Pecora, R. *Dynamic Light Scattering*; John Wiley & Sons, Inc.: New York, 1976.
(12) Etchepare, J.; Grillon, G. Chambaret, J. P., Hamoniaux, G.; Orszag, A. *Opt. Commun.* **1987**, *63*, 329.
(13) Etchepare, J.; Grillon, G. Arabat, J. *Appl. Phys. B.* **1989**, *49*, 425.
(14) Fain, B.; Lin, S. H. *Chem. Phys.* **1992**, *161*, 515.
(15) Siegman, A. *Lasers*; University Science Books: Mill Valley, CA, 1986.
(16) Stone, J. *Appl. Opt.* **1973**, *12*, 1828.
(17) (a) Gordon, J. P.; Leite, G. C. C.; Moore, R. S.; Porto, S. P. S.; Whinnery, J. R. *J. Appl. Phys.* **1965**, *36*, 3. (b) Davis, C. C. *Appl. Phys. Lett.* **1980**, *36*, 515.
(18) Fragnito, H. L.; Bigot, J. Y.; Becker, P. C.; Shank, C. V. *Chem. Phys. Lett.* **1989**, *160*, 101.
(19) Knox, W. H.; Fork, R. L.; Downer, M. C.; Miller, D. A. B.; Chemla, D. S.; Shank, C. V.; Gossard, A. C.; Wiegmann, W. *Phys. Rev. Lett.* **1985**, *54*, 130.
(20) Knox, W. H.; Hirlimann, C.; Miller, D. A. B.; Shah, J.; Chemla, D. S.; Shank, C. V. *Phys. Rev. Lett.* **1986**, *56*, 1191.
(21) Knox, W. H.; Chemla, D. S.; Livescu, G.; Cunningham, J. E.; Henry, J. E. *Phys. Rev. Lett.* **1988**, *61*, 1290.
(22) Oudar, J. L.; Hulin, D.; Migus, A.; Antonetti, A.; Alexandre, F. *Phys. Rev. Lett.* **1985**, *55*, 2074.
(23) Joffre, M.; Hulin, D.; Migus, A.; Mysyrowicz, A.; Antonetti, A. *Rev. Phys. Appl.* **1987**, *22*, 1705.
(24) (a) Kowalczyk, P.; Radzewicz, C.; Mostowski, J.; Walmsley, I. A. *Phys. Rev. A.* **1990**, *42*, 5622. (b) Walmsley, I. A.; Dunne, T. J.; Sweetser, J.; Radzewicz, C. *Ultrafast Phenomena VIII*; Springer-Verlag: Berlin, 1993; p 78.
(25) Dantus, M.; Rosker, M. J.; Zewail, A. H.; *J. Chem. Phys.* **1987**, *87*, 2395.
(26) Placzek, G. *Handbuch der Radiologie*; Marx, E., Ed.; Akademischer Verlag: 1934; Vol. VI, Part 2, p 205.
(27) Ting, C. H. *Spectrochim. Acta* **1968**, *24A*, 1177.
(28) Page, J. B.; Tonks, D. L. *J. Chem. Phys.* **1981**, *75*, 5694.
(29) Wang, C. S. *Phys. Rev.* **1969**, *182*, 482.
(30) Yan, Y. J.; Mukamel, S. *J. Chem. Phys.* **1991**, *94*, 997.
(31) Giordmaine, J. A.; Kaiser, W. *Phys. Rev.* **1966**, *144*, 676.
(32) Hellwarth, R. W. *Prog. Quantum Electron.* **1977**, *5*, 1.
(33) Feynman, R. P. *Rev. Mod. Phys.* **1948**, *20*, 267.
(34) Schwinger, J. *J. Math. Phys.* **1961**, *2*, 407.
(35) Fuller, R. W.; Harris, S. M.; Slaggie, E. L. *Am. J. Phys.* **1963**, *31*, 431.
(36) Carruthers, P.; Dy, K. S. *Phys. Rev.* **1966**, *147*, 214.
(37) Carruthers, P.; Nieto, M. M. *J. Am. Phys.* **1965**, *33*, 537.
(38) Scarfone, L. M. *Am. J. Phys.* **1964**, *32*, 158.
(39) Perelomov, A. *Generalized Coherent States and Their Applications*; Springer-Verlag: New York, 1986).
(40) Senitzky, I. R. *Phys. Rev.* **1960**, *119*, 670.
(41) Mukamel, S.; Yan, Y. J. *J. Phys. Chem.* **1991**, *95*, 1015.
(42) Mukamel, S. *Phys. Rep.* **1982**, *93*, 1.
(43) Mukamel, S.; Loring, R. F. *J. Opt. Soc. B.* **1986**, *3*, 595.
(44) Mukamel, S. *Adv. Chem. Phys.* **1988**, *70*, 165.
(45) Walmsley, I. A.; Wise, F. W.; Tang, C. L. *Chem. Phys. Lett.* **1989**, *154*, 315.
(46) Fain, B.; Lin, S. H. *J. Chem. Phys.* **1990**, *93*, 6387.
(47) Pollard, W. T.; Lee, S.-Y.; Mathies, R. A. *J. Chem. Phys.* **1992**, *92*, 4012.
(48) Lee, S.-Y.; Heller, E. J. *J. Chem. Phys.* **1979**, *71*, 4777.
(49) Heller, E. J.; Sundberg, R. L.; Tannor, D. *J. Phys. Chem.* **1982**, *86*, 1822.
(50) Struve, W. S. *Fundamentals of Molecular Spectroscopy*, John Wiley & Sons: New York, 1989.
(51) Weiner, A. M.; Leaird, D. E.; Wiederrecht, G. P.; Nelson, K. A. *J. Opt. Soc. Am. B* **1991**, *5*, 1264.
(52) Cheng, L.-T.; Nelson, K. A. *Phys. Rev. B* **1988**, *37*, 3603.
(53) Cheng, L.-T.; Nelson, K. A. *Phys. Rev. B* **1989**, *39*, 9437.
(54) Silence, S. M.; Nelson, K. A.; Berger, J. *Phys. Rev. B* **1992**, *46*, 2714.
(55) Farrar, M. R.; Cheng, L.-T.; Yan, Y.-X.; Nelson, K. A. *IEEE J. Quantum. Electron.* **1986**, *QE-22*, 1453.
(56) Yan, Y.-X.; Cheng, L.-T.; Nelson, K. A. *J. Chem. Phys.* **1988**, *88*, 6477.
(57) Cheng, L.-T.; Yan, Y.-X.; Nelson, K. A. *J. Chem. Phys.* **1989**, *91*, 6052.
(58) Duggal, A. R.; Nelson, K. A. *J. Chem. Phys.* **1991**, *94*, 7677.
(59) Silence, S. M.; Duggal, A. R.; Dhar, L.; Nelson, K. A. *J. Chem. Phys.* **1992**, *96*, 5448.
(60) Chiao, R. Y.; Townes, C. H.; Stoicheff, B. P. *Phys. Rev. Lett.* **1964**, *12*, 592.
(61) (a) Lin, C. H.; Heritage, J. P.; Gustafson, T. K. *Appl. Phys. Lett.* **1971**, *19*, 397. (b) Lin, C. H.; Heritage, J. P.; Gustafson, T. K.; Chiao, R. Y.; McTague, J. P. *Phys. Rev. A.* **1976**, *13*, 813. (c) Heritage, J. P.; Gustafson, T. K.; Lin, C. H. *Phys. Rev. Lett.* **1975**, *34*, 1299. (d) Heritage, J. P.; Lin, C. H.; Gustafson, T. K. *IEEE J. Quantum. Electron.* **1972**, *QE-8*, 544.
(62) Kalpouzos, C.; Lotshaw, W. T.; McMorrow, D.; Kenney-Wallace, G. A. *J. Phys. Chem.* **1987**, *91*, 2028.
(63) Lotshaw, W. T.; McMorrow, D.; Kalpouzos, C.; Kenney-Wallace, G. A. *Chem. Phys. Lett.* **1987**, *136*, 323.
(64) Williams, L. R.; Ruhman, S.; Joly, A. G.; Kohler, B.; Nelson, K. A. In *Advances in Laser Science - II*; Lapp, M., Stwalley, W. C., Kenney-Wallace, G. A., Eds.;
(65) Ruhman, S.; Williams, L. R.; Joly, A. G.; Kohler, B.; Nelson, K. A. *J. Phys. Chem.* **1987**, *91*, 2237.
(66) Ruhman, S.; Joly, A. G.; Williams, L. R.; Nelson, K. A. *Rev. Phys. Appl.* **1987**, *22*, 1717.
(67) Ruhman, S.; Kohler, B.; Joly, A. G.; Nelson, K. A. *IEEE J. Quantum Electron.* **1988**, *24*, 470.
(68) Ruhman, S.; Kohler, B.; Joly, A. G.; Nelson, K. A. *Chem. Phys. Lett.* **1987**, *141*, 16.
(69) Greene, B. I.; Farrow, R. C. *Chem. Phys. Lett.* **1983**, *98*, 273.
(70) DeSilvestri, S.; Fujimoto, J. G.; Ippen, E. P.; Gamble, E. B.; Williams, L. R.; Nelson, K. A. *Chem. Phys. Lett.* **1985**, *116*, 146.
(71) (a) Auston, D. H.; Nuss, M. C. *IEEE J. Quantum. Electron.* **1988**, *QE-24*, 184.
(72) Dougherty, T. P.; Wiedderecht, G. P.; Nelson, K. A. *Ferroelectrics* **1991**, *120*, 79.
(73) (a) Dougherty, T. P.; Wiedderecht, G. P.; Nelson, K. A. *Science* **1992**, *258*, 770. (b) Li, Z.; Grimsditch, M.; Chan, S.-K. Accepted for publication in *Ferroelectrics*.
(74) Wiedderecht, G. P.; Dougherty, T. P.; Dhar, L.; Nelson, K. A. Submitted to *Phys. Rev. B*.
(75) Louden, R. *Light Scattering Spectra of Solids*; Springer-Verlag: New York, 1969; p 25.
(76) McMorrow, D.; Lotshaw, W. T.; Kenney-Wallace, G. A. *Chem. Phys. Lett.* **1988**, *145*, 309.
(77) Kohler, B.; Nelson, K. A. *J. Phys. Chem.* **1992**, *96*, 6532.
(78) Kalpouzos, C.; McMorrow, D.; Lotshaw, W. T.; Kenney-Wallace, G. A. *Chem. Phys. Lett.* **1988**, *150*, 138.
(79) Wynne, K.; Galli, C.; Hochstrasser, R. M. *Chem. Phys. Lett.* **1992**, *193*, 17.
(80) Scherer, N. F.; Cho, M.; Ziegler, L. D.; Du, M.; Matro, A.; Cina, J.; Fleming, G. R. *Ultrafast Phenomena VIII*; Springer-Verlag: Berlin, 1993; p 99.
(81) Rosker, M. J.; Wise, F. W.; Tang, C. L. *Phys. Rev. Lett.* **1986**, *57*, 321.
(82) Fragnito, H. L.; Bigot, J.-Y.; Becker, P. C.; Shank, C. V. *Chem. Phys. Lett.* **1989**, *160*, 101.
(83) Pollard, W. T.; Fragnito, H. L.; Bigot, J.-Y.; Shank, C. V.; Mathies, R. A. *Chem. Phys. Lett.* **1990**, *168*, 239.
(84) Dantus, M.; Rosker, M. J.; Zewail, A. H. *J. Chem. Phys.* **1987**, *87*, 2395.
(85) Rose, T. S.; Rosker, M. J.; Zewail, A. H. *J. Chem. Phys.* **1989**, *91*, 7416.
(86) Bersohn, R.; Zewail, A. H. *Ber. Bunsen-Ges. Phys. Chem.* **1988**, *92*, 373.
(87) Bernstein, R. B.; Zewail, A. H. *J. Chem. Phys.* **1989**, *90*, 829.
(88) Williams, S. O.; Imre, D. G. *J. Phys. Chem.* **1988**, *92*, 6636.
(89) Zewail, A. H.; Dantus, M.; Bowman, R. M.; Mokhtari, A. *J. Photochem. Photobiol. A: Chem.* **1992**, *62*, 301.
(90) Misewich, J.; Glownia, J. H.; Rothenberg, J. E.; Sorokin, P. P. *Chem. Phys. Lett.* **1988**, *150*, 374.
(91) Glownia, J. H.; Misewich, J. A.; Sorokin, P. P. J. *Chem. Phys.* **1990**, *92*, 3335.
(92) Walkup, R. E.; Misewich, J. A.; Glownia, J. H.; Sorokin, P. P. *Phys. Rev. Lett.* **1990**, *65*, 2366.
(93) Joly, A. G.; Nelson, K. A. *J. Phys. Chem.* **1989**, *93*, 2876.
(94) Joly, A. G.; Nelson, K. A. *Advances in Laser Science IV*; AIP: New York, 1989; p 333.
(95) Ernsting, N. P. *Ultrafast Phenomena VIII*; Springer-Verlag: Berlin, 1993; p 638.
(96) (a) Banin, U.; Ruhman, S. *J. Chem. Phys.* **1993**, *98*, 4391. (b) Banin, U.; Ruhman, S. Submitted to *Phys. Rev. Lett.*
(97) Williams, L. R.; Nelson, K. A. *J. Chem. Phys.* **1987**, *87*, 7346.
(98) Seyfang, R.; Betz, E.; Port, H.; Schrof, W.; Wolf, H. C. *J. Lumin.* **1985**, *34*, 57.
(99) Tokizaki, T.; Makinura, T.; Akiyama, H.; Nakumara, A.; Tanimura, K.; Itoh, N. *Phys. Rev. Lett.* **1991**, *67*, 2701.
(100) Nuss, M. C.; Zinth, W.; Kaiser, W.; Kaiser, W.; Kolling, E.; Oesterhelt, D. *Chem. Phys. Lett.* **1985**, *117*, 1.
(101) (a) Mathies, R. A.; Brito-Cruz, C. H.; Pollard, W. T.; Shank, C. V. *Science* **1989**, *240*, 777. (b) Schoenlein, R. W.; Peteanu, L. A.; Wang, Q. W.; Mathies, R. A.; Shank, C. V. *Ultrafast Phenomena VIII*; Springer-Verlag: Berlin, 1993; p 53. (c) Pollard, W. T., et al. *J. Phys. Chem.* **1992**, *96*, 6147.
(102) Vos, M. H.; Lambry, J.-C.; Robles, S. J.; Youvan, D. C.; Breton, J.; Martin, J.-L. *Proc. Natl. Acad. Sci. U.S.A.* **1992**, *88*, 8885.
(103) Vos, M. H.; Lambry, J.-C.; Robles, S. J.; Youvan, D. C.; Breton, J.; Martin, J.-L. *Proc. Natl. Acad. Sci. U.S.A.* **1992**, *89*, 613.
(104) Williams, L. R.; Anderson, R. J. M.; Banet, M. J. *Chem. Phys. Lett.* **1991**, *182*, 422.
(105) Williams, L. R.; Anderson, R. J. M.; Banet, M. J. Submitted to *Phys. Rev. B.*
(106) Cho, G. C.; Kutt, W.; Kurz, H. *Phys. Rev. Lett.* **1990**, *65*, 764.
(107) Kutt, W. A.; Albrecht, W.; Kurz, H. *IEEE J. Quantum Electron.* **1992**, *28*, 2434.
(108) Cheng, T. K.; Vidal, J.; Zeiger, H. J.; Dresselhaus, G.; Dresselhaus, J. S.; Ippen, E. P. *Appl. Phys. Lett.* **1992**, *59*, 1923.

(109) Zeiger, H. J.; Vidal, J.; Cheng, T. K.; Ippen, E. P.; Dresselhaus, G.; Dresselhaus, M. *Phys. Rev. B.* **1991**, *45*, 768.
(110) Vidal, J.; Cheng, T. K.; Fung, A. W.; Zeiger, H. J.; Ippen, E. P.; Dresselhaus, G.; Dresselhaus, M. S. In *Pump-Probe Study of $Bi_{1-x}Sb_x$ Alloys*; Bristowe, P. D., Broughton, J., Newsam, J. M., Eds.; *Mater. Res. Soc. Proc.* (Pittsburgh, PA, 1992); to be published.
(111) Weiner, A. M.; Heritage, J. P.; Kirschner, E. M. *J. Opt. Soc. B.* **1988**, *5*, 1563.
(112) Weiner, A. M.; Leaird, D. E.; Wiedderecht, G. P.; Nelson, K. A. *Science* **1990**, *247*, 1317.
(113) Weiner, A. M.; Leaird, D. E.; Wiedderecht, G. P.; Nelson, K. A. *J. Opt. Soc. B.* **1991**, *5*, 1264.
(114) Kutt, W.; Pfeifer, T.; Dekorsky, T.; Kurz, H. *Ultrafast Phenomena VIII.*
(115) Nelson, K. A.; Miller, R. J. D.; Lutz, D. R.; Fayer, M. D. *J. Appl. Phys.* **1982**, *53*, 1144.
(116) Gerdy, J. J.; Dantus, M.; Bowman, R. M.; Zewail, A. H. *Chem. Phys. Lett.* **1990**, *171*, 1.
(117) Potter, E. D.; Herek, J. L.; Perersen, S.; Liu, Q.; Zewail, A. H. *Nature* **1992**, *355*, 66.
(118) Fourkas, J.; Wilson, W.; Wackerle, G.; Frost, A. E.; Fayer, M. D. *JOSA B* **1989**, *6*, 1905.
(119) Scherer, N. F.; Ruggiero, A. J.; Du, M.; Fleming, G. R. *J. Chem. Phys.* **1990**, *93*, 856.
(120) Scherer, N. F.; Carlson, R. J.; Matro, A.; Du, M.; Ruggiero, A. J.; Romero-Rochin, V.; Cina, J. A.; Fleming, G. R.; Rice, S. A. *J. Chem. Phys.* **1991**, *95*, 1487.
(121) Scherer, N. F.; Matro, A.; Ziegler, L. D.; Du, M.; Carlson, R. J.; Cina, J. A.; Fleming, G. R. *J. Chem. Phys.* **1992**, *96*, 4180.
(122) Schoenlein, R. W.; Mittleman, D. M.; Shiang, J. J.; Alivisatos, A. P.; Shank, C. V. *Phys. Rev. Lett.* **1993**, *70*, 1014.